VO_2 Thin Films and Nanoparticles, from Chemical Vapour Deposition and Hydrothermal Synthesis, for Energy Efficient Applications

This thesis is submitted in partial fulfilment of the requirements for the Degree of Doctor of Philosophy (Chemistry)

Michael J. Powell

2015

Supervised by: Professor Ivan P. Parkin and

Professor Claire J. Carmalt

Declaration

I, Michael Powell confirm that the work presented in this thesis is my own. Where information has been derived from other sources, I confirm that this has been indicated in the thesis.

Abstract

Thin films of VO_2 were synthesised by atmospheric pressure chemical vapour deposition (APCVD). The effect of deposition time on the thickness of the films was studied. The samples synthesised were the first time monoclinic VO_2 has been demonstrated by the reaction between vanadium (IV) chloride and ethyl acetate under APCVD conditions.

Multi-layer films of $VO_2/SiO_2/TiO_2$ were also synthesised by APCVD and the effect on the thermochromism and visible light transmission were investigated. The multi-layered $VO_2/SiO_2/TiO_2$ is the first such multi-layer to be demonstrated by APCVD.

A specialised Fluidised Bed Chemical Vapour Deposition (FBCVD) reactor was designed and built specifically for the project, with this design being utilised to coat powder substrates with thin films of TiO_2. A multi-shelled system of anatase on rutile on mica was deposited to demonstrate that the FBCVD system is capable of depositing core-shell and multi-shelled systems with fast and uniform growth rates. The different TiO_2 samples were tested for their photocatalytic properties by measuring stearic acid destruction rates.

VO_2 nanoparticles were synthesised by Continuous Hydrothermal Flow Synthesis (CHFS), with the effect of temperature and residence time within the CHFS reactor on the phase produced and particle size distribution was evaluated. This is the first time that CHFS has been used to produce VO_2 nanoparticles.

Finally, CHFS was used to synthesise nanoparticles of Nb doped VO_2. The effect of varying the concentration of Nb was investigated by evaluating the phase of vanadium oxide synthesised, the range of particle size and the thermochromic properties observed in the material.

Acknowledgements

I would first like to thank my supervisors, Ivan Parkin and Claire Carmalt, who have supported me through the PhD process, keeping me on track when I needed the extra encouragement. The Parkin/Carmalt group have also been a fantastic group of people to get to know over the last few years, and I will have many treasured memories from my time at UCL. I would also like to thank Beckers Industrial Coatings for financial support towards the PhD project.

For help learning the various techniques I used to synthesise and analyse my samples I would like to thank Prof. Jawwad Darr, Dr Sanjay Sathasivam, Dr Pete Marchand, Mr Clement Denis, Dr Joe Bear, Mrs Penny Carmichael, Dr Alison Cross, Dr Will Travis, Dr Steven Firth and Mr Martin Vickers- all of your support has been invaluable! Special thanks goes to Dr Raul Quesada-Cabrera, who has really helped to energise my final year of PhD studies and actually managed to put up with me- a herculean feat if ever there was one.

Beyond the lab, I would like to thank Dr Emma Newton, Dr Michael Warwick, Dr Ana Jorge-Sobrido, Mr Nick Chadwick, Mr Will Peveler, Miss Emily Glover and Miss Monika Jurcic for always being willing to have a cup of tea or a pint depending on what was required! Your friendship throughout the process has meant so much to me.

I would like to thank my auntie Annie- who was always willing to come to the pub and discuss chemistry with me!

I would also like to thank my bandmates, Miss Catriona Harris, Mr Jamie Pegge and Mr Giacomo Zucconi- being able to play with you guys over the last year has been incredible and really helped me relax away from the lab.

Finally, I would like to thank my Mum, Dad, sister- Chrissie and Naomi, brothers-in-law Joel and Lukasz, and the two cheeky monkeys (nephews) Jack and Peter. You've had to put up with me for many years now, and I'm afraid it isn't the end yet!

List of contents

List of figures

List of tables

List of Abbreviations

AACVD	Aerosol assisted chemical vapour deposition
APCVD	Atmospheric pressure chemical vapour deposition
CHFS	Continuous hydrothermal flow synthesis
CVD	Chemical vapour deposition
FBCVD	Fluidised bed chemical vapour deposition
HR	High resolution
IR	Infra-red
MST	Metal-to-semiconductor transition
SEM	Scanning electron microscopy
TEM	Transmission electron microscopy
T_{lum}	Photopically averaged transmittance
T_{sol}	Solar modulation
UV/Vis	Ultra violet/ visible/ near infra-red spectroscopy
VO_2 (M)	Monoclinic vanadium (IV) oxide
VO_2 (R)	Tetragonal vanadium (IV) oxide
XPS	X-ray photoelectron spectroscopy
XRD	X-ray diffraction

Chapter 1

Introduction

Chapter 1: Introduction

1.1 Introductory remarks

This thesis is focused on the development of thin film and nanoparticle synthetic routes of monoclinic vanadium (IV) oxide. Vanadium (IV) oxide is a thermochromic material that displays a fully reversible, temperature induced phase transition.[1] The following literature review will concentrate on the fundamental principles underlying the thermochromic behaviour of VO_2, including proposed reasons for the behaviour observed in the monoclinic to tetragonal phase change. Comparison and evaluation of routes to the synthesis of monoclinic VO_2 will be discussed, with pros and cons of the different methodologies discussed, a brief overview of both hydrothermal and chemical vapour deposition will be given- these being the principle synthetic methods used for producing the samples discussed throughout this thesis. Methods for altering the phase transition temperature, through both doping of the material and inducing strain effects by lattice mismatch to the substrate will be discussed.

Finally, the visible light transmission of VO_2 will also be discussed, including proposed methods to alter the visible light transmission of the material.

1.2 Properties of vanadium (IV) oxide

Vanadium oxides display a wide range of phases, with both primary and mixed oxides present in the phase diagram.[2] This is due to the ability of vanadium to assume many oxidation states, from V(0) in the elemental state to V(V) when fully oxidised.[3]

Vanadium (IV) oxide is formed when the ratio of V:O is 1:2 (±0.1 % O).[4] Vanadium (IV) oxide has four known phases, these are known as VO_2(A),[5] (B),[6] (M) and (R).[7] VO_2(A) and (B) have shown promise for the intercalation of Li ions for battery applications.[6, 8] Undoped monoclinic VO_2 [VO_2(M)] shows a reversible phase transition to a tetragonal (rutile) structure at ~68 °C.[2] This phase change is accompanied by a large change in both the optical, in near IR wavelengths, and electronic properties.[7] Monoclinic VO_2 has semi-conductor properties, with a distinct band-gap (~0.7 eV), and is both transmissive to near IR wavelengths and poorly conducting of electricity. Tetragonal VO_2, on the other hand, has semi-metallic properties, with the valence and conduction bands overlapping and is reflective of near IR wavelengths and has good electrical conductivity. Due to the fully reversible nature of the MST in VO_2, there are many potential applications for VO_2 thin films

and powders. These include: solar control coatings,[9, 10] data storage[11] and optical computing.[12, 13] The vast majority of current research is based on the use of VO_2 in solar control coatings.

Goodenough was the first researcher to propose an explanation for this phase change and the associated change in properties.[2, 7] It was suggested that in the monoclinic phase, the vanadium ions would each have an unpaired electron in the d_{II} orbital. These d-orbitals can overlap, to form a V-V bond. In the tetragonal phase, the electrons are released from the V-V bond. This induces a change in the band-structure of the material, leading to the semi-metallic properties observed above the phase transition temperature (T_c). Figure 1.01 (a) and (b) show pictorial representations for this.

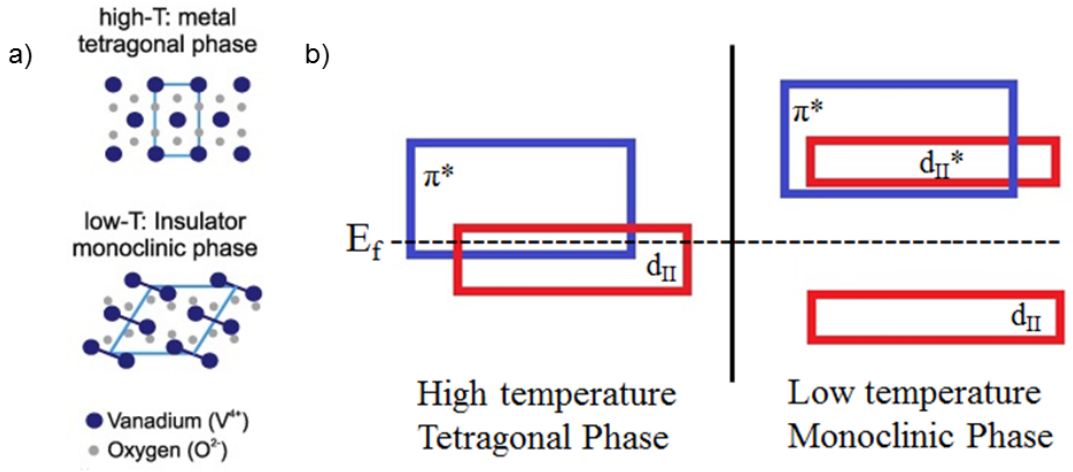

Figure 1.01: Pictorial representations for a) the lattice parameters for monoclinic and tetragonal VO_2 phases; in the monoclinic phase, vanadium ions share a pair of electrons forming V-V bonds and b) the band structure for the monoclinic (semi-conducting) and tetragonal (semi-metallic) phases.

The metal-to-semiconductor transition (MST) is closely associated with a change in band structure.[2] In the monoclinic phase the electrons in the d_{II} orbitals are paired together, this creates a structure where pairs of vanadium atoms are bonded together. As the electrons are held in bonds between the vanadium atoms, below the MST VO_2 has a distinct band-gap, of ~0.7 eV, and acts as a semi-conductor. Above the MST, the band structure changes, the d_{II} orbitals overlap with the π* orbitals. This change in the band structure releases the electrons held in the V-V bonds, these electrons are then able to move as there is no longer an effective band-gap, as the π* orbitals are thermally achievable, as shown in Figure 1.01 (b). This results in the material becoming semi-metallic.[7]

The exact nature of the phase change has been a subject of much debate. Whether the phase change is driven by a change in band structure (electronic effect) or by a change in lattice parameters (steric effect) has been unclear. A recent study by Wall *et al.* has focused on determining the timescale for the structural and electronic changes observed when VO_2 passes through the MST.[14] Until recently, it has been impossible to determine whether the atomic rearrangement leads to the band alteration or vice versa. Using broadband time-resolved reflection spectroscopy, Wall *et al.* were able to show that the electronic band structure change was established within the femtosecond range, whereas the structural change occurred over the picosecond range. This study also noted that during the phase change, the electronic and structural properties were in a state of flux and could neither be described as semi-conducting or semi-metallic in nature, but were a complex mix of the two.

This conclusion has been supported by work done by Peng *et al.*[15] In this study, the use of far infra-red (FIR) spectroscopy was used to model the electronic and structural changes associated with the MST. It was found that there were 2 distinct electronic structural changes, a slow change which had both semi-conducting and semi-metallic properties at 304-335 K and an abrupt change at 335 K. This study also showed that there was a delay between the electronic and structural changes, with the electronic changes happening before the structural ones.

1.3 VO_2 for solar control coatings

Due to the significant difference in transmission of near IR wavelengths between the monoclinic and tetragonal phases of VO_2, the ability to have thermochromic applications for solar control is possible.[16] The VO_2 can be coated on surfaces, such as windows or roofs, when the temperature is below the T_c near IR wavelengths will be transmitted into the building, alleviating the need for some of the central heating and thus preventing the release of excess greenhouse gases that contribute to climate change.[17] When the temperature is above the T_c the VO_2 undergoes a phase change and becomes highly reflective to near IR wavelengths. This would mean that there would be less of a need for air conditioning to be used.[18] As air conditioning units rely on electricity, and most electricity is currently produced by the burning of fossil fuels which release large amounts of greenhouse gases into the atmosphere contributing to climate change, the use of thermochromic solar control coatings could allow for a comfortable environment inside buildings whilst also allowing energy efficiency. A schematic for this process is shown in Figure 1.02.

Buildings are currently estimated to account for ~40% of annual CO_2 emissions,[19] so if heating and air-conditioning loads can be reduced this would lead to a significant reduction in anthropogenic CO_2 emissions.

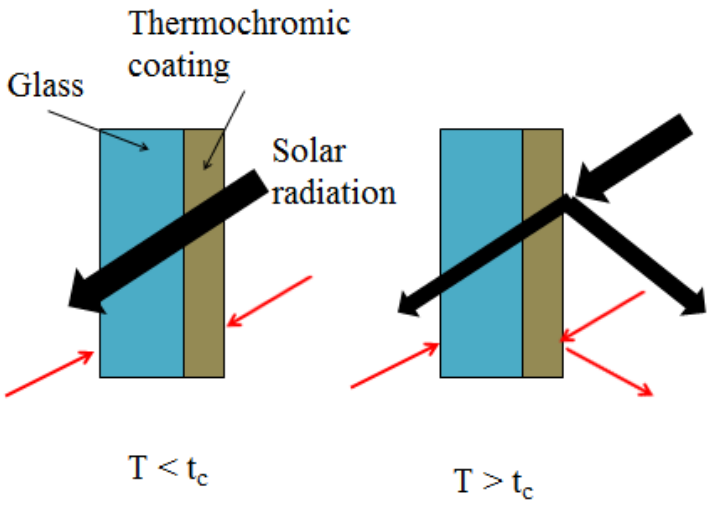

Figure 1.02: Schematic of a VO_2 solar control coating, below the MST, infra-red radiation is transmitted through. Above the MST, the infra-red wavelengths are reflected away by the VO_2 coating. This switch happens reversibly and is controlled by the temperature of the surrounding environment, there is no additional energy input required to achieve the switch in the material.

1.4 Synthesis methods for producing VO_2

Several methods for producing VO_2 have been researched, these include physical vapour deposition,[20] sputtering,[9, 21, 22] sol-gel methods,[23-25] hydrothermal synthesis[26-30] and chemical vapour deposition.[11, 31-33] The two most widely researched methods for producing VO_2 thin films and nanoparticles are CVD and hydrothermal synthesis, these are also the methods that will be used for the synthesis of materials discussed in this thesis.

1.5 Chemical Vapour Deposition

Chemical vapour deposition (CVD) is a method used to cover large substrates quickly and uniformly. It is commonly used in industry to coat glass,[11, 34, 35] produce sensors/electronics[36-38] and synthesise corrosion resistant coatings.[39-41] There are many forms of CVD including aerosol assisted CVD,[42-44] low-pressure CVD,[45-47] plasma enhanced CVD,[48-50] atmospheric pressure CVD[51-53] and fluidised bed CVD.[54-56]

VO_2 thin films have been previously reported from APCVD and AACVD techniques. Manning *at al.* have successfully formed thin films from a variety of precursors *via* APCVD.[31, 32, 57, 58] This has included the doping of VO_2 thin films with tungsten, this leads to the lowering of the thermochromic switching temperature.[32, 57]

Blackman *et al.* have also been able to synthesise VO_2 thin films *via* APCVD.[11] In this study it was shown that the concentrations of precursors used could be lowered, which both ensured that the system was less prone to blockages forming whilst also improving the conditions to allow the formation of high quality VO_2 films onto substrates.

Piccirillo *et al.* have been able to successfully produce VO_2 thin films *via* AACVD.[10, 33, 43] A solution of $[VO(acac)_2]$ in ethanol was made into an aerosol *via* a Vicks humidifier, with the resulting mist being pasted over a heated glass substrate, yielding VO_2. Further studies by Piccirillo *et al.* showed that doping of VO_2 was also possible in AACVD by Nb[43] and W.[33]

Warwick *et al.* have also used an AACVD process coupled with electric fields to control the size of the crystallites formed during the deposition of VO_2 thin films.[59-61]

AACVD is not currently used in industrial processes, unlike APCVD. The main reason for this is that APCVD is a more mature technology than AACVD. AACVD relies on the generation of an aerosol which is then carried by an inert gas to the reaction chamber. The reactant is then deposited onto a heated substrate. Oxygen is added to the reaction by either the use of an oxygen source being dissolved into the solution used for the aerosol, or oxygen gas can be 'bled' into the reaction chamber. The advantage of AACVD over APCVD is that there are no unwanted nucleation reactions, the reactants are carried by a cold gas and can only react over the heated substrate surface. The disadvantage of AACVD is that the reactant must be soluble in a suitable solvent, if the solvent is too viscous it is impossible to generate a good enough aerosol. The deposition times of AACVD also tends to occur over about 30 minutes as compared with 2-3 minutes for APCVD. For these reasons, APCVD methods were chosen as the method for producing thin films of VO_2 for the research discussed in this thesis.

1.5.1 Atmospheric Pressure Chemical Vapour Deposition

CVD is a technique to deposit a solid product onto a substrate by means of a gas-phase or surface reaction. There are many differing forms of CVD each tailored for a particular purpose. For an Atmospheric Pressure Chemical Vapour Deposition (APCVD) process the mechanistic steps are generally considered to be:[62]

- Transport of the reactive species to the substrate surface
- Gas phase reaction
- Adsorption onto the substrate surface
- Nucleation on the substrate surface
- Reaction and desorption of by-products
- Film Growth

This is shown pictorially in Figure 1.03.

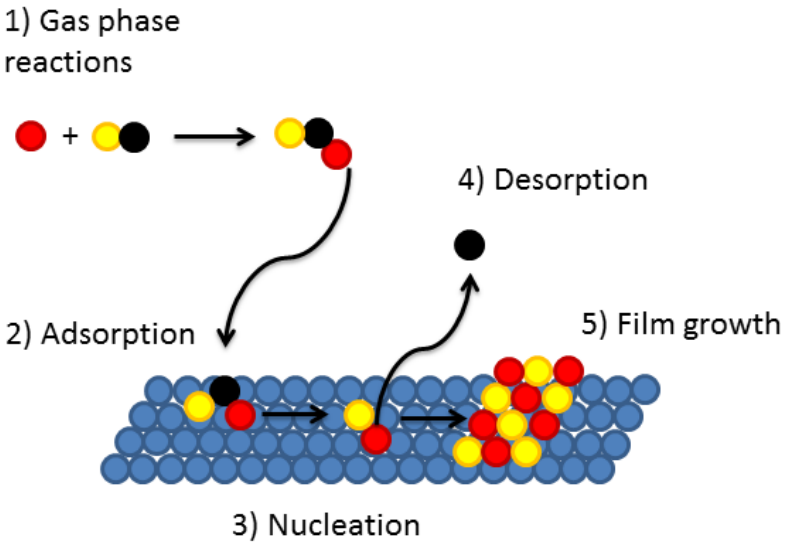

Figure 1.03: Diagram showing the necessary mechanistic steps during a Chemical Vapour Deposition process to deposit a thin film from the initial precursors.

APCVD requires the reactor to be at or close to atmospheric pressure, meaning that the precursors must be either low melting solids or highly volatile liquids. Precursors are carried to the reactor in an inert gas stream (usually N_2) which is heated to prevent condensation of the precursors. The precursors and carrier gas are then

passed over a heated substrate which causes the nucleation of the precursor on the surface of the substrate. The substrate is generally significantly hotter than the carrier gas, which helps to minimise the effect of gas phase reactions.

1.5.2 Reaction sites in CVD

For the thin films grown in this project, a cold-walled CVD reactor was used. In the reaction chamber itself two types of broad reaction can occur; homogeneous gas phase reactions and heterogeneous vapour-solid phase reactions. Due to the use of a cold-walled reactor, the homogenous gas phase reactions are significantly reduced meaning that only the vapour-solid phase reactions need be considered from a mechanistic point of view.[62]

1.5.3 Film growth mechanisms

The kinetics of any given CVD process is complex. There are, however, models which help describe the most likely explanations for some of the different morphologies observed in CVD processes.[63]

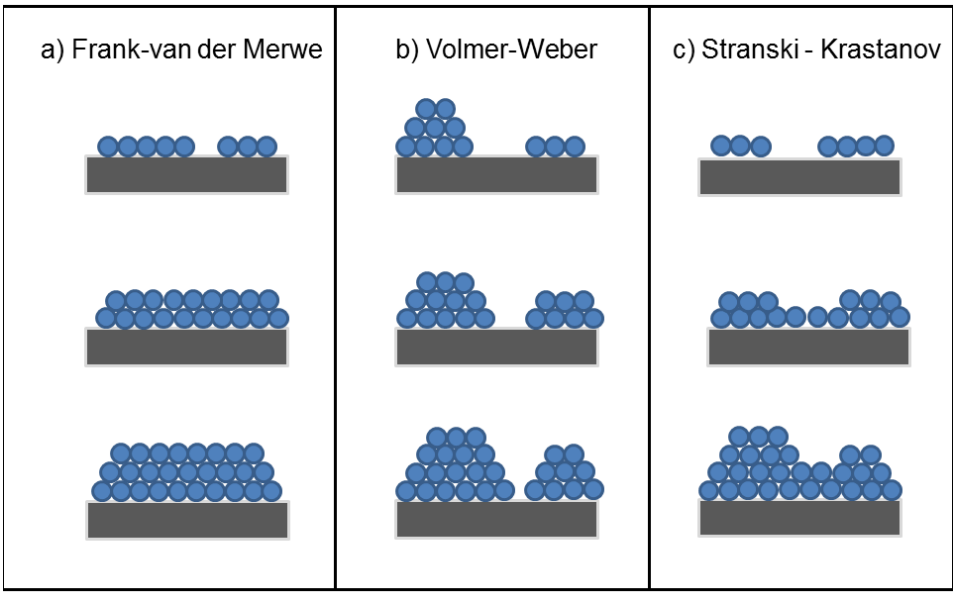

Figure 1.04: Pictorial representations for some of the different growth patterns in Chemical Vapour Deposition processes.

The Frank-van der Merwe mechanism, Figure 1.04 (a), proceeds layer by layer, with the atoms in the film being more strongly attracted to the substrate than to each other. The Volmer-Weber mechanism, Figure 1.04 (b), proceeds through an island growth mechanism, with the atoms in the deposited film being more strongly attracted to each other than the film. The Stranski-Krastanov mechanism, Figure

1.04 (c), is between the two extremes, proceeding initially by a layered growth followed by an island type growth thereafter.

1.5.4 Film growth rates

In APCVD processes the rate of film growth is governed by two factors, the mass transport of precursors into the reactor and the surface kinetics of the reaction. The mass transport can be controlled by the rate precursors arrive at the substrate surface, it also has a maximum theoretical rate. The surface kinetics are controlled by the temperature of the substrate, initially a higher substrate temperature will increase the reaction rate due to increased decomposition of precursors. The rate can slow, however, due to increased desorption of precursors or exhaustion of precursors at very high deposition temperatures.

1.5.5 Fluidised Bed Chemical Vapour Deposition

Fluidised Bed Chemical Vapour Deposition (FBCVD) is a commonly used process in industry to coat powders for corrosion resistance.[41, 54, 64-67] FBCVD has also been used to synthesise carbon nanotubes.[68-71] It is not a commonly used laboratory technique, however, and so there has been little published on the ability to deposit materials beyond corrosion resistant coatings and carbon nanotubes.

1.5.5.1 Processes involved in Fluidised Bed Chemical Vapour Deposition

The FBCVD syntheses presented here work on the same principles as those outlined for Atmospheric Pressure Chemical Vapour Deposition (APCVD).

For an FBCVD process, there are several factors that must be considered. Due to the reactor being at, or close to, atmospheric pressure the chemical precursors must be either low melting solids or volatile liquids. The precursors are carried to the reactor by a heated stream of an inert carrier gas, usually nitrogen. The substrate to be coated needs to be heated too. This is to ensure that there is sufficient energy for the nucleation of reactive species. As the APCVD and FBCVD reactions are very similar in terms of precursor types, reaction temperatures and transportation of the precursors to the reactor, it is likely that similar film growth mechanisms are observed for each system. The final consideration for a fluidised bed process is the fluidisation of the substrate to ensure uniform coverage by the precursors.

1.5.5.2 Geldart Fluidisation groups:

Fluidisation of the substrate relies on the ability of a stream of gas to apply sufficient pressure to cause a powdered solid to attain fluid like properties- in a fluidised bed reactor this means that the solid substrate becomes free-flowing under the force of gravity. One of the main considerations in the fluidisation process is the choice of substrate to be fluidised. Substrates can be sorted into Geldart Groupings.[72] This gives 4 groups of substrate type, based on the density difference and mean particle size.

The 4 groups can be summarised as:

A) Small particle sizes (20-100 μm) and low density (typically < 1.4 g/cm^3). This group tends to show an increase in the bed expansion prior to fluidisation, due to a decrease in bulk density. The particles are poorly cohesive.

B) Intermediate particle sizes (40-500 μm) and medium density (1.4-4 g/cm^3). This group does not show a large increase in the bed expansion before fluidisation occurs. The particles are poorly cohesive.

C) Very small particle sizes (10-30 μm) and very high cohesion between particles. Very difficult to fluidise, normally requires application of a mechanical force as well as gas pressure.

D) Large particles (> 600 μm) and very high densities. Fluidisation requires high fluid energies and results in high levels of abrasion. These types of particles are usually deposited in shallow or spouted bed designs.

Typically, Geldart groups A and B are favoured for fluidised bed processes as these are easily fluidised and do not require additional mechanical elements in the design of the reactor.

1.5.5.3 Fluidised Bed Reactor Designs:

There are 5 types of fluidisation bed reactor designs. Of these types, the reactors can be loosely divided into those that rely solely on the gas flow and those that require additional mechanics to initiate fluidisation.[56]

For the reactors that rely solely on gas flow, there are stationary/bubbling and circulating fluidised bed reactors. The bubbling reactors can use low or high gas flows, with the solids either remaining relatively stationary or suspended in the bed. The circulating fluidised bed has a higher gas flow, therefore the solid is suspended

within the bed. This means that the surface of the bed is much less smooth, and particles can become entrained from the bed. In the circulating design, the entrained particles can be recirculated back into the bed through the use of cyclones. Both of these reactor designs are only suitable for Geldart group A and B types.

The remaining fluidised bed designs all rely on a mechanical element to ensure fluidisation of solids within the bed. These are vibratory fluidised beds, flash reactors and annular fluidised beds. Vibratory fluidised beds are similar in principle to bubbling beds, with the addition of a vibrating bed to help achieve fluidisation of the particles. Flash reactors work at much higher gas velocities than other reactor types, this means that the solid particles can achieve similar velocities to the gas which allows denser/more cohesive particles to be coated uniformly- this come at the expense of the heat distribution. Annular fluidised beds have a large nozzle at the centre of the bed that allows for a high velocity gas to be injected directly into the fluidised bed- once again this enable dense/highly cohesive particles to be fluidised. Although the mechanical reactor bed types allow the fluidisation of Geldart groups C and D to be achieved, this comes at with additional cost and complexity meaning that these designs are only suitable if the substrate to be coated must have cohesive properties or a high mass/density.

1.6 Hydrothermal Synthesis

Hydrothermal synthesis is a commonly used technique for the production of nanoparticles,[73-75] zeolites[76-78] and metal organic frameworks.[79-81] As with CVD techniques, there are several different methods to produce materials, these include the use of templates,[82, 83] surfactants[84, 85] and continuous hydrothermal techniques.[86-88]

Hydrothermal treatments of VO_2 sol gels can lead to the formation of nanoparticles with interesting morphologies. Liu *et al.* have reported on the formation of VO_2 powders from a hydrothermal treatment of V_2O_5 powders followed by annealing under a N_2 atmosphere.[89] This led to the formation of clusters and nanosheets which were shown to have thermochromic properties.

Munoz-Rojas *et al.* have also reported on hydrothermal synthesis of VO_2. In this study, clusters of hydrated VO_2 ($VO_2 \cdot H_2O$) were formed from the hydrothermal reaction of V_2O_5 and hydrazine.[90] These clusters were then annealed under an N_2 atmosphere to produce VO_2 nanoparticles. Clusters that were initially formed with a

hydrothermal synthesis temperature of 50 °C showed interesting hollow sphere morphologies and were also shown to have good thermochromic properties.

Ji *et al.* have reported on the hydrothermal treatment of V_2O_5 with H_2O_2 to synthesise the hydrated form, this was followed by reduction with hydrazine and annealing under an N_2 atmosphere.[27] This produced phase pure VO_2 nanoparticles with thermochromic properties.

Doping studies have also been performed under hydrothermal conditions, Gao *et al.* studied the effects of antimony doping on the size and shape of VO_2 nanoparticles synthesised under hydrothermal conditions.[26] It was found that the oxidation state of the antimony altered the size of the nanoparticle formed, with the Sb^{3+} causing the creation of a greater number of oxygen vacancies as the nanoparticles formed which resulted in a smaller crystal size. This was attributed to the Sb^{3+} having a greater atomic radius and lower oxidation state than V^{4+}.

1.6.1 Nucleation and growth of particles

In a hydrothermal synthesis, there are 3 main processes that occur, these are as described by the LaMer model of nanoparticle formation.[91] The first step is the formation of a precursor solution; the formation of the precursor solution is often achieved through sol-gel synthesis. The solution is then either put into a sealed autoclave and heated to the desired temperature for a certain amount of time (this is known as a batch hydrothermal process); or a continuous hydrothermal process can be used, here the precursor is feed into a stream of super-critical (or superheated) water, where rapid hydrolysis and dehydration occurs.[86]

Regardless of the hydrothermal process employed, the next two steps are nucleation of particles, where the particles spontaneously nucleate in solution forming larger clusters. This then leads to particle growth, where the small clusters grow by consuming the precursor solution surrounding them. This is summarised in Figure 1.05

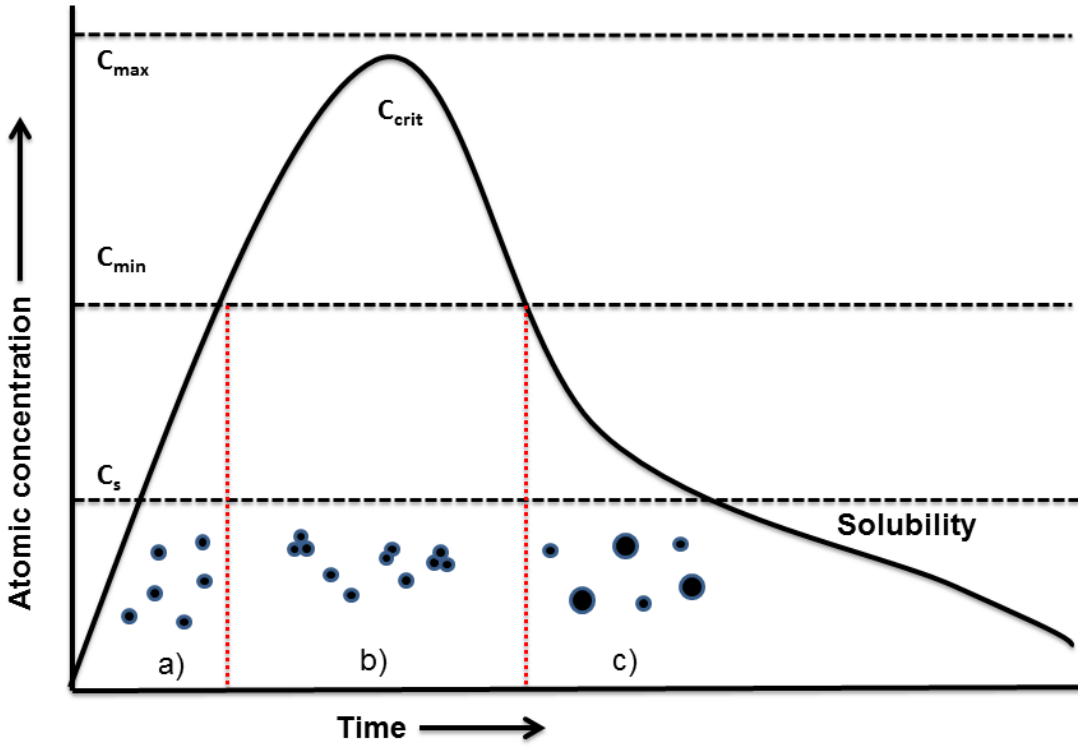

Figure 1.05: LaMer model of nanoparticle formation from aqueous conditions. Where, **a)** generation of atoms, **b)** self-nucleation of particles, **c)** particle growth, $\mathbf{C_s}$ = saturation concentration, $\mathbf{C_{min}}$ = minimum concentration for particle nucleation, $\mathbf{C_{max}}$ = critical limiting supersaturation and $\mathbf{C_{crit}}$ = critical concentration.

This process can also be described by a Gibbs energy plot for the nucleation of particles, Figure 1.06. Gibbs energy describes the thermodynamic processes that act during particle formation and growth. For nanoparticle synthesis (from a solution containing individual atoms) the reaction proceeds by the removal of solvent molecules from the precursor followed by the formation of a lattice by the precursor molecules. While the formation of a lattice reduces the overall free energy, releasing energy in the process, the removal of solvent molecules requires the input of energy. The change in Gibbs energy for the nucleation and growth of nanoparticles from solution can be expressed as the sum of these changes in energy, Equation 1.1.[92, 93]

$$\Delta G = -\frac{4}{3}\pi r^3 \Delta G_v + 4\pi r^2 \gamma \qquad (1.1)$$

Where: **ΔG** is the change in Gibbs energy; **r** is the particle radius; $\mathbf{\Delta G_v}$ is the free energy change associated with the change in volume by the formation of the nanoparticles; **γ** is the surface energy of the nanoparticles.

Briefly, in order for a process to be favourable, the overall change to the Gibbs energy must be negative. For the formation of nanoparticles from solution, there are two competing factors. The first is the surface free energy (**ΔG_s**) which acts against nucleation and the second is the volume free energy (**ΔG_v**) which favours nucleation and particle growth. For particles to spontaneously nucleate from solution, a critical energy (**ΔG***) must be overcome. In hydrothermal processes, this is achieved through the use of high reaction temperatures and pressures.

The growth of the nanoparticles, in hydrothermal processes, can be controlled through the use of surfactants,[84, 85, 94, 95] concentration of precursor solutions,[96, 97] pH,[96, 98] temperature,[99, 100] use of templates/directing agents,[101-103] length of hydrothermal treatment[99, 104, 105] and the use of dopants.[106, 107]

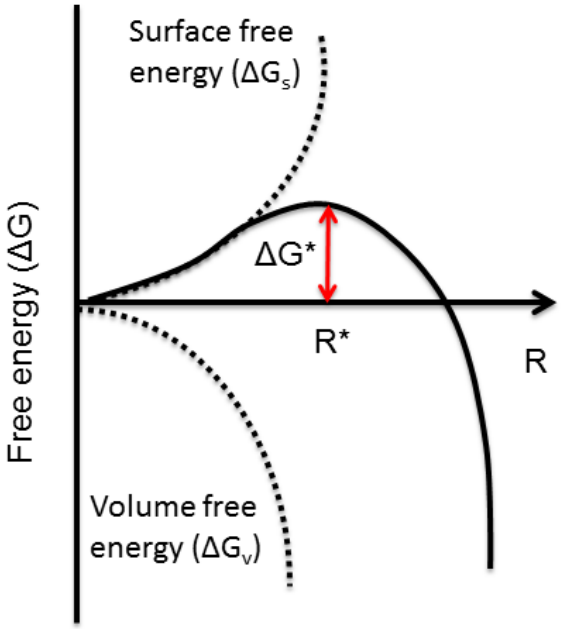

Figure 1.06: Gibbs energy plot, where: **R** = particle radius, **R*** = critical particle radius, **ΔG*** = critical free energy for spontaneous particle nucleation (barrier energy to formation of nanoparticles).

1.6.2 Sol-gel synthesis of VO_2

As hydrothermal techniques are solution based reactions, a discussion of sol-gel techniques is essential to understand the differing methods for producing VO_2 from solution based methods. A sol-gel is a colloidal solution that contains the precursors for the material in-situ. In a review of VO_2 production techniques, Nag *et al.* state

that sol-gel techniques are employed due to the ability to cover wide areas at low cost and also the possibility of metal doping.[108]

In 1983 Greenberg reported on the formation of VO_2 *via* gel hydration.[109] In this synthesis slides were dip-coated into a solution containing vanadyl triisopropoxide, and subsequently reduced. The VO_2 films were then analysed using XRD and UV/Vis spectroscopy.

The earliest VO_2 sol-gel synthesis was reported with the use of either oxoisopropoxides or butoxides. Lakeman *et al.* stated that this was because the annealing conditions were more important for the formation of the correct oxidation state on the vanadium metal than the initial precursors.[110] Speck *et al.* reported in 1988 on the formation of VO_2 thin films *via* a sol-gel process.[111] In this study, a sol-gel was formed *via* the reaction of vanadium (IV) chloride and lithium diethylamide, this was followed by a the addition of isopropoxide to give a vanadium tetra-isopropoxide sol. Slides were then dip-coated into the prepared sol-gel and annealed between 400-700 °C under a nitrogen atmosphere.

Keppens *et al.*[112] and Yin *et al.*[113] have reported on an aqueous sol-gel route to VO_2 thin films. This involves the addition of molten V_2O_5 to distilled water. Slides were dip-coated into the resulting sol-gel, before been heated in a reducing atmosphere ($CO:CO_2$ = 1:1) and finally been annealed under nitrogen to give VO_2. An advantage of this sol-gel synthesis is the ability to add other water soluble dopants into the sol.[114] Sol-gel synthetic techniques have since been refined to allow the production of VO_2 in fewer steps. Partlow *et al.* successfully obtained VO_2 thin films from a sol-gel of vanadium oxide isopropoxide [$VO(OC_3H_7)_3$], the film characteristics were tested by XRD, UV/Vis spectroscopy and SEM, showing that the films were thermochromic and having a phase transition between monoclinic and tetragonal at ~68 °C.[115]

Huang *et al.* have also described a sol-gel route to VO_2 nanotube arrays,[116] in this synthesis ammonium metavanadate [NH_4VO_3] was reacted with oxalic acid [$H_2C_2O_4$] to give a dark blue solution, this was then annealed under a N_2 atmosphere to obtain VO_2 nanotubes. A third sol-gel route towards VO_2 was described by Pan *et al.* this route involved the addition of [$VO(acac)_2$] to methanol.[25] As with the first synthetic route, this method required no reduction of the vanadium centre, as the vanadium is in the 4+ state in [$VO(acac)_2$]. All previous sol-gel routes had to incorporate an annealing step under a N_2 atmosphere.

1.7 Doping of VO_2 to decrease the MST

Although V_2O_3[10] (MST = -123 °C/ 150 K) and V_2O_5[2] (MST= 350 °/ 623 K) show the same switching behaviour, VO_2 has the closest phase transition to room temperature ~ 68 °C. This temperature is, however, too high for use in solar control coatings.

The temperature of the MST can be altered by including dopants in the crystal lattice. Dopants incorporated into VO_2 have included W^{6+},[32, 57, 117] Nb^{5+},[9, 43, 118] Mo^{5+},[23, 31, 119] Fe^{3+},[120] Ti^{4+},[121, 122] Cr^{3+},[4, 123] F^{-}[124] and Mg^{2+}.[30, 125] It was found that Fe^{3+} and Ti^{4+} increased the MST temperature whereas W^{6+}, Nb^{5+}, Mo^{5+}, F^{-} and Mg^{2+} decreased the MST temperature. The largest decrease in the MST temperature was found to be for W, where for each atom 1% incorporated into the crystal lattice the MST temperature decreased by ~25 °C.[57, 126] Doping with metals such as W^{6+} does have a maximum atom %, this is because W is only partially soluble in solid solution. Above 2.8 at% the W begins to form islands within the crystal lattice.[33] When VO_2 is doped with metals, it can be observed that the ionic radius plays a key role. Ions with an ionic radius larger than V^{4+} (0.058 nm), such as W^{6+} (0.060 nm) and Nb^{5+} (0.078 nm), tend to reduce the MST switching temperature. Ions with an ionic radius smaller than V^{4+}, such as Ti^{4+} and Al^{3+},[122, 127] tend to increase the MST switching temperature. The explanation for this behaviour is that the larger ions ensure that the vanadium centres stay in the V^{4+} state. Smaller ions on cause the formation of V^{5+} defects within the lattice, although no reasons are presented for why this increases the MST temperature.

A second more in depth explanation examines the effect of oxidation state on the band structure. In this theory, as postulated by Goodenough, the incorporation of dopant ions into the crystal lattice forms a secondary phase in between the semi-conducting and metallic phases.[7] These phases are either associated with the monoclinic or tetragonal crystal structure. Goodenough argued that low valent ions form a second semi-conducting phase that is monoclinic and so increases the MST switching temperature, whilst high valent ions form a phase that is tetragonal in nature and so decrease the MST switching temperature.

These observations can further be supported by considering the contribution of d electrons from the dopant ions into the band structure of the crystal lattice. High valent cations, such as W^{6+}, Nb^{5+} and Mo^{5+}, are able to interact through π orbitals. As the electrons around a 3rd row transition metal are loosely held, the W ion has electron density available to donate. These electrons have an energy similar to the

π* orbitals of the V atom. Increasing the electron density in the π* orbital destabilises the monoclinic phase as it weakens the V-V bonds. This also has the effect of charge compensation as the formal oxidation state on the vanadium atoms becomes V^{3+}. This has the effect of lowering the MST switching temperature. The same is true for anions such as F^-. This is as stated by Goodenough[7] and Tang *et al*.[126]

Low valent cations tend to be stabilise the antiferroelectric distortion, as the electron density on these cations interact with the π orbitals on the V atoms, strengthening the V-V bonds. Coupled to this the monoclinic phase has co-ordination sites that are more suited to low valent ions. This explains why ions, such as Cr^{3+}, tend to increase the MST switching temperature. This is as argued by Pan *et al.*[25] and Burkhardt *et al.*[128]

VO_2 displays a hysteresis loop as the phase changes from monoclinic to tetragonal. This hysteresis loop can be monitored *via* UV/Vis spectroscopy, XRD and Raman spectroscopy. Ideally the hysteresis loop should be over a small as possible temperature range for the purpose of using VO_2 in solar control coatings. The addition of dopants, such as W^{6+}, increases the hysteresis loop.[129] As this increase in the hysteresis loop is undesirable, recent research has focused on reducing both the MST temperature and the hysteresis loop. One method for achieving this is by co-doping the VO_2. Co-doping systems such as W and Ti, have been shown to successfully reduce both the temperature and hysteresis loop in the VO_2 thin films. Takahashi *et al.* co-doped VO_2 thin films with W and Ti. This study suggested that the reduction in the hysteresis loop was due to mechanical stress factors and not an electronic interaction.[130]

As well as altering the MST temperature and hysteresis loop width, doping can cause other changes to the characteristics of VO_2 thin films and powders. One such property that has been shown to be affected is the colour of the film produced.[24, 57, 117, 124] This is purely an aesthetic property but an important issue regarding the use of VO_2 films as solar control coatings. Undoped VO_2 thin films are a yellow/brown colour, this has two effects, firstly it diminishes the amount of visible light being transmitted by the windows and secondly brown is an undesirable colour for use in windows in buildings. The colour of the films can be altered upon doping, incorporation of W^{6+} ions lead to the films becoming blue in colour, as reported by Manning *et al.*[57] and Peng *et al*.[117] This occurs when there is roughly 2% atom

incorporation by weight. Rougier *et al.* state that the blue colour apparent in the W doped films are due to the inclusion of WO_3 crystallites.[131]

Another method to alter the appearance of VO_2 films is to incorporate F^- ions into the crystal lattice. In experiments by Kiri *et al* showed that as the % atom incorporation increases the films become transparent to visible light, due to the absorption band edge of the films moving towards the UV region, this is as argued by Burkhardt *et al*.[132] The authors determined that due to the electronegativity of the fluorine there was a shift of the d bands to higher energy levels, the second reason argued is that as the fluorine destabilises the V^{4+}-V^{4+} homopolar bonds by 'injecting' electron density into the V 3d orbitals. This causes the films to become transparent to visible light. The drawback of using F^- ions into the films is that fluorine doping has little effect on the MST switching temperature.[124]

Co-doping of W and F into the VO_2 lattice has been shown to improve the transmission of visible light whilst also bringing down the MST switching temperature of the deposited films.[128, 132] This suggests that the F and W act independently of each other on the VO_2 crystal lattice, with the F^- ions affecting the band onset of the VO_2 whilst the W^{6+} destabilises the monoclinic phase by its interactions with the π* orbitals of the V^{4+} centres. The main drawback of a method such as this is that it requires extra steps in order to be produced and so increases the costs of producing films; this would have a direct knock-on effect to the consumer in the cost of the product which could become prohibitive.

Doping of Mg has also been shown to improve the visible light transmission of VO_2 materials.[30, 133, 134] Granqvist *et al*. have modelled the interaction of Mg with VO_2 and suggested that the effect is similar to that seen with fluorine.[134] As with the addition of fluorine, magnesium doping does not have a large effect on the MST phase transition temperature.

1.8 Reduction of the MST in VO_2 thin films through strain effects

The MST switching temperature can be altered by strain effects within the material. Nagashima *et al*[135] and Kikuzuki *et al*[136] showed that by ensuring a lattice mis-match between the substrate and VO_2 crystal lattice, the resulting strain effect made the MST switching temperature decrease. This is due to the difference in energy states between the monoclinic and tetragonal phase. By using a tetragonal TiO_2 phase (rutile), this ensured that the tetragonal phase of VO_2 was energetically favoured.

Muraoka *et al.* performed a series of depositions of VO_2 onto TiO_2 substrates.[137] It was found that the MST temperature was altered due to the strain effects created by the lattice mismatch between the film and substrate, with films grown on a (001) TiO_2 substrate having a decrease in the MST temperature due to in-plane tensile stress, while films grown on a (110) TiO_2 substrate showed an increase in the MST temperature.

Strain effects are also present when an extremely thin film <100 nm is deposited onto a substrate. Cao *et al* have reported on the reduction of the MST to room temperature due to the use of strain effects alone.[138] In this study, single crystals of VO_2 were grown and subjected to strain effects. It was found that by the application of strain, the MST temperature could be brought down to around room temperature. Gregg *et al.* have also reported on strain effects VO_2.[139] In this study thin films of VO_2 were grown on α-Al_2O_3 substrates. Strain was then applied mechanically to the substrates and the effect on the resistance of the VO_2 films was measured. The reason that strain has an effect on the MST temperature in VO_2 is due to the system trying to reduce the energy in the crystal lattice, as extra strain energy is applied the crystal lattice adopts a higher symmetry formation, this lowers the energy of the system.[140]

A further way to control the metal to semiconductor phase transition switching temperature of VO_2 is to change the size of the crystallites. This is due to the effect of strain on the phase transition. Highly strained surfaces will be stabilised by adopting the least strained crystal formation. This means in a VO_2 system the MST temperature can be lowered due to strain effects. Kiri *et al.* noted that when F-doping VO_2 the reduction in the MST temperature was most likely due to an increase in the strain of the films.[124]

Nagashima *et al.* have also studied the effects of strain on the MST temperature in VO_2.[141] It was found that the film thickness could be used to lower the MST, with films with a thickness of 15 nm or less showing the MST at 300 K as opposed to 341 K for bulk VO_2. This was attributed to the effects of strain on the film surface. Samples with a thickness of less than 15 nm showed very few cracks in the morphology of the film, whereas samples with thickness greater than 15 nm showed many cracks in the morphology. This suggests that thicker samples have less strain than thinner samples, this means that thinner samples have a higher surface energy and will tend towards the lowest energy configuration. As these films were grown on

TiO_2 (001) the tetragonal phases have a greater phase match than the monoclinic on tetragonal and so the semi-metallic tetragonal VO_2 phase is favoured.

1.9 Composite and multi-layered VO_2 thin films

VO_2 thin films have been synthesised on TiO_2 supports. This can also infer increased chemical stability and can also create multifunctional films due to the photoinduced superhydrophilicity of TiO_2 under UV irradiation and the anti-microbial nature of such films.[142]

Qureshi *et al*. reported on composite films of TiO_2/VO_2 produced by APCVD.[143] It was found that a multi-functional thermochromic and self-cleaning film could be produced from a chemical vapour deposition route. Wilkinson *et al.* reported on the combinatorial APCVD of VO_2/TiO_2 films.[144] It was found that the incorporation of V^{4+} into the TiO_2 lattice resulted in a decreased photocatalytic activity. However, the incorporation of Ti^{4+} into the VO_2 lattice resulted in a decrease in the MST, most likely due to increased strain within the films as a result of the lattice mis-match between the VO_2 and TiO_2 crystallites.

Chen *et al.* reported on the use of TiO_2 and SiO_2 layers in VO_2 films to act as anti-reflection coatings.[145] It was found that the thickness of the TiO_2, SiO_2 and VO_2 films strongly controlled the observed thermochromism. The inclusion of TiO_2 enabled the transmission of visible wavelengths to be increased whilst maintaining good switching properties. Huang *et al*. have reported on the synthesis of a SiO_2/VO_2, TiO_2/VO_2 and ZrO_2/VO_2 thin films *via* sol-gel methods.[146] In all cases, the inclusion of a material with a different refractive index led to an improvement in optical properties when compared with a single VO_2 analogue. The optical properties were dependent on film thickness, with the thinnest VO_2 depositions showing the greatest visible light transmission.

1.10 Properties of VO_2 nanoparticles

VO_2 nanoparticles have been synthesised by sol-gel,[147, 148] hydrothermal[26, 90] and ion-implantation techniques.[149, 150] Nanoparticles of VO_2 have received much attention over recent years due to the possibility of alleviating the poor visible light characteristics and improving the colour of VO_2 solar control coatings.[151]

1.10.1 Altering the optical properties of nanoparticles

The functional properties of VO_2 can also be altered by the growth of nanoparticles. As nanoparticles tend to be highly strained, the MST switching temperature can be lowered through the control of the particles growth rate. Another area that is becoming increasingly researched is the optical characteristics of nanoparticle VO_2. VO_2 is a brown colour, which is undesirable, if nanoparticles are grown that are smaller than the wavelength of visible light then the particles will not absorb in the visible range of the electromagnetic spectrum and the powders/films produced will be transparent to visible light.

Li *et al.* have shown through experimental work and calculation that nanoparticular VO_2 is able to transmit visible light with high efficiency whilst still remaining the thermochromic nature of the material.[152]

Li *et al.* have also conducted calculations into VO_2 core-shell structures.[153] This work focused on taking an SiO_2 shell and coating it with VO_2, the functional properties of these systems were then calculated and compared against experimental data. It was found that thin-walled VO_2 nanoshells showed the same thermochromic properties as solid nanoparticles. It was noted that the core-shell VO_2 had a decrease in the transmission of visible light.

Appavoo *et al.* studied the effects of crystallite size on the hysteresis width of the transition between the monoclinic and tetragonal phases of VO_2 using Plasmon Resonance Spectroscopy.[154] Here it was found that the larger the crystallite size the smaller the hysteresis width of the transition between the monoclinic and tetragonal phases, this was attributed to the number of defects in the structure that could act as nucleation sites for the atomic rearrangement that occurs when a phase change happens. Larger particles have fewer grain boundaries, which results in the creation of a greater number of defects and hence more nucleation sites.

Zhou *et al.* reported on the Mg-doping of VO_2 nanoparticles by a hydrothermal synthesis.[30] When XRD studies were combined with density functional theory calculations, it suggested that the primitive cell of the VO_2 increased on the addition of Mg into the lattice, as well as this the a and b cell parameters increased whilst the c parameter decreased suggesting a greater amount of strain in the doped films when compared with the non-doped systems.

1.10.2 Core-shell VO_2 nanoparticles

The synthesis of core-shell VO_2 nanoparticles can allow for the fine tuning of optical properties, resistance to chemical attack and improvement in the solar modulation of the VO_2. Gao *et al.* reported on core-shell of SiO_2/VO_2 structures.[155] It was found that by the addition of the SiO_2 shell, the transmittance of the material could be increased by ~20%, which would enable the films to have a lighter colour making them more applicable for use in fenestration. The drawback with this technique is that it also reduces the intensity of the thermochromic response.

Li *et al.* have also published on the core/shell route, using SiO_2/VO_2 structures.[28] In this study, a hydrothermal synthesis first produced VO_2(B) nano-plates this was followed by a post-annealing step to produce VO_2(M), the plates were produced either with an SiO_2 shell or just as pure VO_2. In this study it was found that the inclusion of the SiO_2 shell increased the intensity of the thermochromic effect. This effect was attributed to the development of nano-pores during the annealing process, as VO_2(B) has a lower density than VO_2(M), this meant that there was a greater surface area and so a larger thermochromic effect.

1.11 Thesis outline

This thesis focuses on the synthesis of VO_2 thin films multi-layers and nanoparticles for use as thermochromic materials for solar modulation in building architecture. The development of a new precursor route to CVD of VO_2 thin films will be introduced and discussed. This will lead on to the production of multi-layered and multi-functional VO_2 thin films, with a discussion of the improvement observed in the properties of the multi-layered films when compared to single layer VO_2 analogues.

The design of a fluidised bed CVD reactor will be introduced. This reactor was designed especially for this research project. Initial reactions will be introduced and discussed, with deposition of TiO_2 onto powder substrates used as a case study to demonstrate the system.

Finally, the use of continuous flow hydrothermal synthesis for the production of VO_2 nanoparticles will be demonstrated. Both undoped and Nb-doped VO_2 systems will be discussed, with explanations given for the differences observed in properties and morphologies of the nanoparticles. Finally, the results discussed in this thesis are summarised with potential future work from the results obtained.

Chapter 2

Depositions of thin films of VO_2 by Atmospheric Pressure Chemical Vapour Deposition

Chapter 2: Depositions of thin films of VO_2 by Atmospheric Pressure Chemical Vapour Deposition

2.1 Introduction

Atmospheric Pressure Chemical Vapour Deposition (APCVD) is a commonly used industrial technique for the deposition of thin films onto substrates. These thin films often serve a functional purpose, such as TiO_2 thin films which give self-cleaning properties when deposited onto glass substrates.[156, 157] APCVD has also been demonstrated for depositing films of VO_2 onto glass substrates.[16, 18, 58] An issue, however, with the use of thin films of VO_2 is the yellow/brown colour of the films, which is aesthetically unpleasing and results in a decrease in the transmission of visible wavelengths.[30, 121, 151]

Modelling of VO_2 systems have suggested that a possible route to diminish the effect of the colour would be the production of very thin films (<100 nm).[135] As the films should be weakly absorbing of visible wavelengths, but still interact with near IR wavelengths.[151] Groups working on such thin films are primarily using reactive magnetron sputtering.[9, 147, 158]

Thin films of monoclinic VO_2 have been deposited by sol-gel,[24, 111, 114] magnetron sputtering,[9, 159, 160] aerosol assisted chemical vapour deposition[43, 61, 124] and atmospheric pressure chemical vapour deposition.[16, 52, 161] APCVD was the chosen method for producing the VO_2 films deposited for this chapter due to the fast growth rates, uniform coverage, high crystallinity and inexpensive precursors used in the APCVD process.[162]

Being able to reliably deposit thin films of VO_2 (<100 nm) by APCVD would allow for development of thermochromic technologies. VO_2 thin films, from APCVD, have been previously deposited by the reaction of VCl_4 and H_2O,[16] $VOCl_3$ and H_2O[58] and $[VO(acac)_2]$.[163] The use of ethyl acetate as an oxygen precursor for APCVD has been previously demonstrated for TiO_2 thin films,[157] but not for VO_2. Presented in this chapter are VO_2 thin films deposited by the reaction of VCl_4 and ethyl acetate.

2.1.1 The Atmospheric Pressure Chemical Vapour Deposition reactor

The APCVD syntheses reported here were deposited on a horizontal cold-walled reactor. The reactor design is shown schematically in figure 2.01. The precursors were contained in bubblers under nitrogen (N_2) gas flow, which was used as a carrier gas. The bubblers consisted of stainless steel cylinders with brass jackets and heating bands. All lines were heated using heating tapes (*Electrothermal* 400 W, 230 V). The precursors were mixed in stainless steel mixing chambers. The temperature of all components of the system was controlled by k-type thermocouples with *Thermotron* controllers.

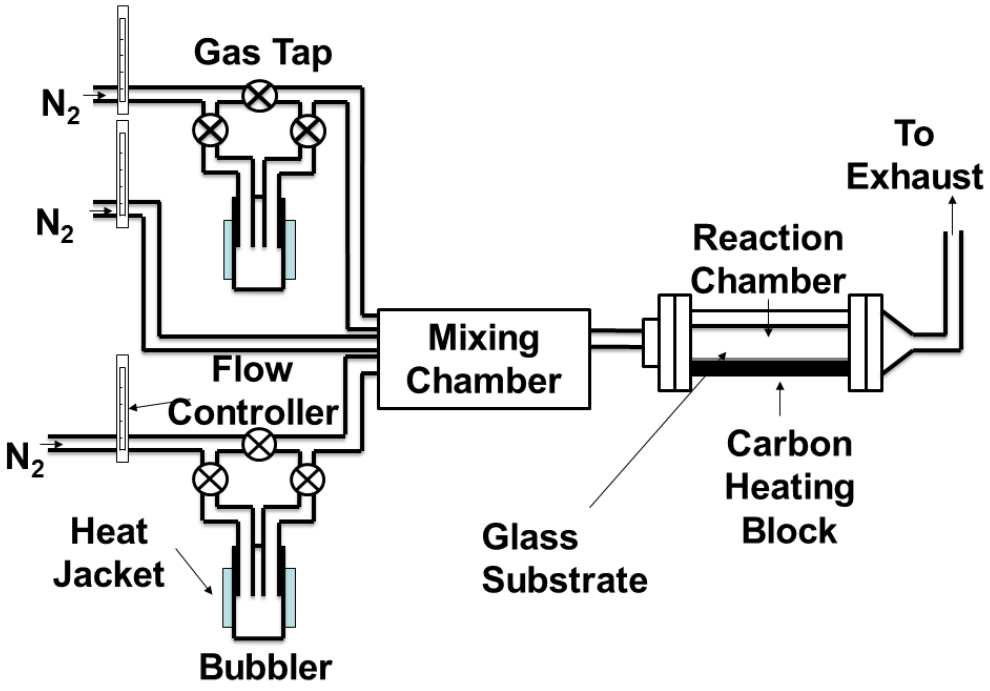

Figure 2.01: Schematic diagram showing the Atmospheric Pressure Chemical Vapour Deposition rig.

2.2 Synthesis of VO2 thin films by APCVD

2.2.1 Aim

To determine whether thin films (<100 nm) can be achieved by the reaction of VCl_4 and ethyl acetate in APCVD conditions. To ascertain the growth mechanism and rates of the VO_2 thin films. To determine how the thickness of the films affects the thermochromic and visible light transmission of the VO_2.

2.2.2 Experimental

For the following reactions the vanadium precursor source used was vanadium (IV) chloride (VCl_4, 99.9%) and the oxygen precursor source used was ethyl acetate anhydrous ($C_4H_8O_2$, 99.8%) both precursors were purchased from *Sigma Aldrich UK*. All chemicals were used without additional treatment. Glass-substrates consisted of a 3.4 mm silica coated barrier glass (50 nm SiO_2 layer) obtained from *Pilkington*. The glass substrate was 90 x 300 mm. Prior to deposition all substrates were cleaned with acetone, 2-propanol and water and left to air dry. Oxygen-free nitrogen (99.9 % purity) was purchased from *BOC* and used as the carrier gas for all reactions.

For the synthesis of VO_2 layers, VCl_4 was placed in bubbler 1 and ethyl acetate was in bubbler 2. Bubbler 1 and 2 were heated to 80 and 40 °C respectively. This achieved a suitable vapour pressure from the precursors, as determined from the vapour pressure equation, equation 2.1.[162]

$$a = \frac{Vp \times F}{(760 - V_p) \times 24.4} \qquad (2.1)$$

Where, *a* is the amount of material introduced (in mol min^{-1}), V_p is the vapour pressure of the material at the temperature in the bubbler (mmHg),[164] *F* is the flow rate of the carrier gas (L min^{-1}).

2.2.3 Initial reactions

Initial depositions of vanadium oxide films were performed using the vapour pressures established for $TiCl_4$ reacting with ethyl acetate to synthesise TiO_2 thin films. It seemed likely that the formation of VO_2 would be favoured by the same mass transport of precursors to the APCVD reactor. In a typical APCVD reaction to form TiO_2 from $TiCl_4$ and ethyl acetate, an excess of ethyl acetate has been found to

give reproducible results.[165] This gives a ratio of 1:2.4 $TiCl_4$: ethyl acetate. Therefore, a ratio of 1:2.4 was also used for the reaction of VCl_4: ethyl acetate. The deposition lengths were also fixed initially at 3 minutes, as this gave a reasonable mass flow of precursors into the reaction chamber, ensuring that the films deposited would be of a reasonable thickness for analysis.

2.2.4 Sample Descriptions for thin film studies

In a typical synthesis, the reactor was set to 550 °C (ramp rate 7 °C min^{-1}). The plain N_2 gas flow set to 20 L min-1 and the plain flow lines heated to 200 °C. The mixing chamber was set to 150 °C. For the deposition of VO_2, the VCl_4 bubbler was set to 80 °C and had a N_2 gas flow set at 0.7 L min^{-1}. The $C_4H_8O_4$ bubbler was set to 40 °C and had a N_2 gas flow set at 0.2 L min^{-1}. Depositions would last between 15 seconds and 3 minutes. After a deposition, the sample would be left to cool under a flow of nitrogen and would only be removed when the temperature was below 90 °C. Sample descriptions and synthesis conditions are summarised in table 2.1. The thin films were characterised as deposited, there was no post-treatment of any of the films.

Name	Description	Deposition length
VO_2-1	VO_2 thin film on glass	15 seconds
VO_2-2	VO_2 thin film on glass	30 seconds
VO_2-3	VO_2 thin film on glass	1 minute
VO_2-4	VO_2 thin film on glass	3 minutes

Table 2.1: Sample descriptions and deposition lengths for VO_2 depositions on glass substrates.

2.2.5 Film Characterisation

X-ray diffraction (XRD) studies were carried out using a Bruker-Axs D8 (GADDS) diffractometer. The instrument operates with a Cu X-ray source, monochromated ($K\alpha_1$ and $K\alpha_2$) and a 2D area X-ray detector with a resolution of 0.01º (glancing incident angle, θ = 0.3º). The diffraction patterns obtained were compared with database standards from the Inorganic Crystal Structure Database (ICSD), Karlsruhe, Germany. Raman spectroscopy was carried out using a *Renishaw 1000* spectrometer equipped with a 633 nm laser. The Raman system was calibrated using a silicon reference. UV/vis spectroscopy was performed using a Perkin Elmer

Lambda 950 UV/Vis/NIR Spectrophotometer. The transmission spectra were recorded directly on the films as deposited, held in a specially designed heating cell allowing the beam to pass through the sample directly into the integrating sphere. A *Labsphere* reflectance standard was used as reference in the UV/vis measurements. The heating of the samples for thermochromic measurements in the UV/Vis spectrometer was achieved by an aluminium temperature cell controlled by RS cartridge heaters, Eurotherm temperature controllers and k-type thermocouples. Scanning electron microscopy (SEM) was carried out using a Jeol JSM-6700F and secondary electron image on a Hitachi S-3400N field emission instruments (20 KV) and the Oxford software INCA. X-Ray photoelectron spectroscopy (XPS) was performed using a Thermo Scientific K-alpha spectrometer with monochromated Al Kα radiation, a dual beam charge compensation system and constant pass energy of 50 eV (spot size 400 μm). Survey scans were collected in the range 0-1200 eV. XPS data was fitted using CasaXPS software, the vanadium $2p_{3/2}$ and O1s peaks were modelled with Gaussian functions. The Gaussian functions had a FWHM value of 1.8 and 1.7 for V^{5+} and V^{4+} respectively (with a tolerance of ±0.2) the oxygen had a FWHM of 1.8 (with a tolerance of ±0.2) these values were obtained from literature measurements.[166, 167]

2.3 Results and Discussion

2.3.1 Initial reactions

Thin films of monoclinic VO_2 were deposited by the reaction of vanadium (IV) chloride and ethyl acetate by APCVD. The overall reaction of VCl_4 and ethyl acetate is described in equation 2.2. Previous APCVD reactions had used water as the oxygen source, with lower mass flow rates and slower film growth rates.[31, 57, 58, 168]

$$VCl_4 + C_4H_8O_2 \rightarrow VO_2 + \text{by-products} \qquad (2.2)$$

The mechanism by which VCl_4 and ethyl acetate react is unknown. A possible mechanism involves the hydrolysis of VCl_4 *via* decomposition of the ethyl acetate to form ethenone (ketene) and ethanol and subsequent dehydration of ethanol to form ethene and water.[169] Proposed mechanism route shown in equation 2.3.

$$CH_3COOC_2H_5 \rightarrow CH_3CH_2OH + C_2H_2O$$

$$CH_3CH_2OH \rightarrow H_2O + C_2H_4$$

$$2H_2O + VCl_4 \rightarrow VO_2 + 4HCl \qquad (2.3)$$

It can be seen from the above reaction that for each VCl_4 molecule reacted, 2 molecules of ethyl acetate must be decomposed for the formation of VO_2. If the ratio of ethyl acetate were higher, the formation of V_2O_5 would be favoured. If the ratio of ethyl acetate were lower, the formation of V_2O_3 would be favoured.[2] The reaction outlined above will not be the only reaction occurring within the reactor chamber, therefore the oxygen precursor normally needs to be in excess to achieve the desired phase.[62]

Table 2.2 outlines the deposition conditions and vanadium oxide phases identified for the initial reactions on the APCVD rig.

Reactor Temp (°C)	**VCl_4 Mass flow rate (mol min^{-1})**	**Ethyl acetate Mass flow rate (mol min^{-1})**	**Phase(s) present**
550	0.00288	0.00554	Magneli e.g. V_4O_9, V_3O_7
550	0.00288	0.00288	VO_2(M)
550	0.00554	0.00554	VO_2(M)
550	0.00554	0.00288	VO_2(M)

Table 2.2: Initial deposition conditions for the formation of vanadium oxide thin films by the reaction of VCl_4 and ethyl acetate by APCVD.

The higher flow rate of ethyl acetate resulted in the formation of an over oxidised vanadium oxide film, commonly referred to as a Magneli phase. These are crystal structures that contain a mix of vanadium oxidation states and do not display thermochromic behaviour.[170, 171] This was a surprising result when compared with the $TiCl_4$/ethyl acetate system, and is attributed to the greater reactivity of VCl_4, which has been shown to have a higher rate of thermally induced decomposition when compared to $TiCl_4$.[172]

With the remaining initial films deposited, the superior films were the ones deposited with a ratio of 2:1 VCl_4: ethyl acetate. This was due to the films being monoclinic VO_2 and also suffering the least from carbon contamination, which would make the films a darker brown colour. As VO_2 films already suffer from poor visible light transmission, any increase in visible wavelength absorption is a particularly large problem in the synthesis of VO_2 thin films.[125]

The effect of deposition temperature on the phase of vanadium oxide achieved in the deposited films was also investigated. The temperature of the reactor was set to 500, 525 and 550 °C, with VO_2 films being deposited for 3 minutes for each sample. Whilst all reaction temperatures produced monoclinic VO_2 films, the films produced at lower temperatures suffered from increased carbon contamination, as assessed by a visual inspection of the deposited films, and were also less reproducible than the films deposited at 550 °C. For this reason, for the subsequent thin films VO_2 depositions by the reaction of VCl_4 and ethyl acetate by APCVD, the reaction conditions the temperature of deposition was set to 550 °C with the mass flow rates of the VCl_4 and ethyl acetate being set to 0.00554 and 0.00288 mol min^{-1} respectively.

2.3.2 Phase identification of depositions

Thin films of monoclinic VO_2 were deposited by the reaction of vanadium (IV) chloride and ethyl acetate under APCVD conditions. Depositions were varied between 15 seconds and 3 minutes. Sample descriptions can be found in Table 2.1.

The VO_2 thin films, deposited from APCVD, where characterised initially by XRD and Raman spectroscopy. The samples VO_2-1 and VO_2-2 were very thin and so did not defract X-rays well, figure 2.02 shows typical X-ray patterns for samples VO_2-3 and VO_2-4. The peak at 27.8° corresponds to the (011) plane of VO_2. The peak at 37.1° can also be observed, which is assigned to the closely spaced group of the (202), (211) and (200) planes. As there were very few reflections, the XRD patterns were assigned using literature values (ICSD 34033). The data presented here is typical of VO_2 thin films from CVD processes.[58, 61, 163]

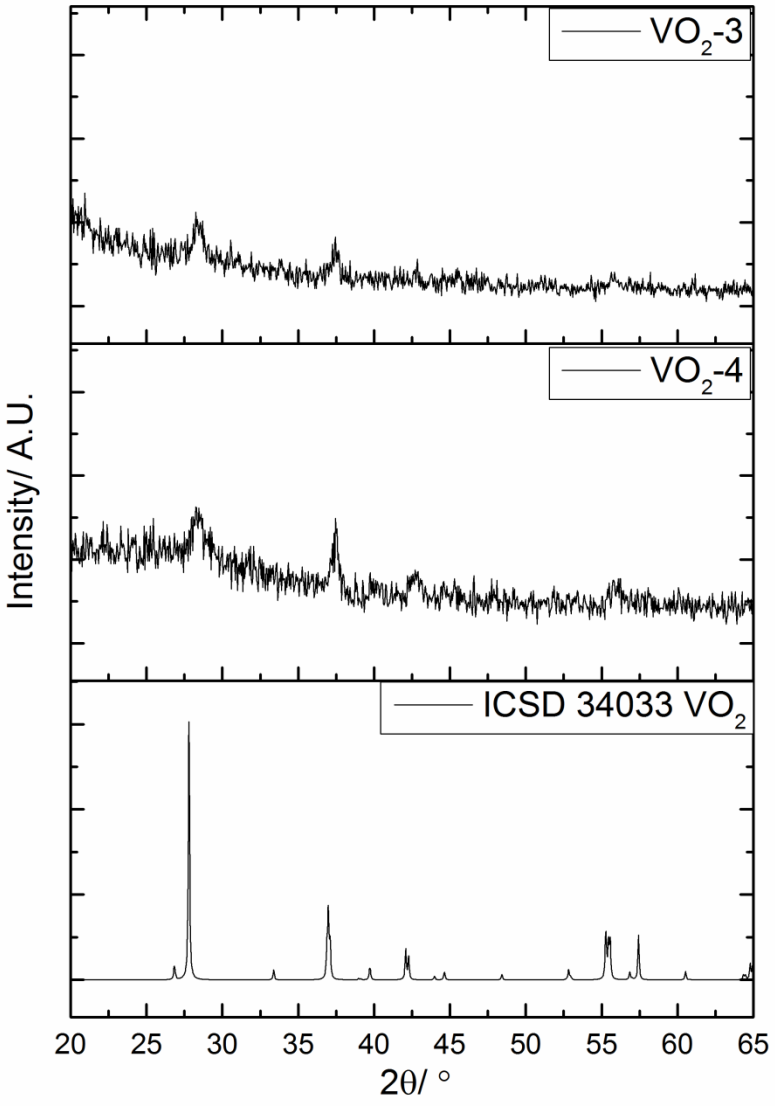

Figure 2.02: Typical XRD patterns for monoclinic VO_2 thin films deposited by APCVD.

Raman spectroscopy is a complementary phase identification technique to XRD. Being a more surface sensitive technique, compared to XRD, it can be used to elucidate the phases present in thin films. A typical Raman spectrum for VO_2 thin films deposited by APCVD is shown in figure 2.03. The Raman shift values match those described by *Barreca et al*.[173] The bands present at 142, 191, 221, 261, 303, 337, 393, 487 and 614 cm^{-1} are within ± 2 cm^{-1} of the literature values. All bands present in the Raman spectrum are assigned to monoclinic VO_2, with the bands at 191, 221, 303, 337, 393, 487 and 614 cm^{-1} being assigned to the A_g mode, the band at 261 cm^{-1} being assigned to the B_g mode and the band at 142 cm^{-1} being unassigned.[174-177] The Raman band at 614 cm^{-1} is likely due to the stretching of V-

O-V bridging bonds, with the other bands being due to the bending of V-O bonds.[178, 179]

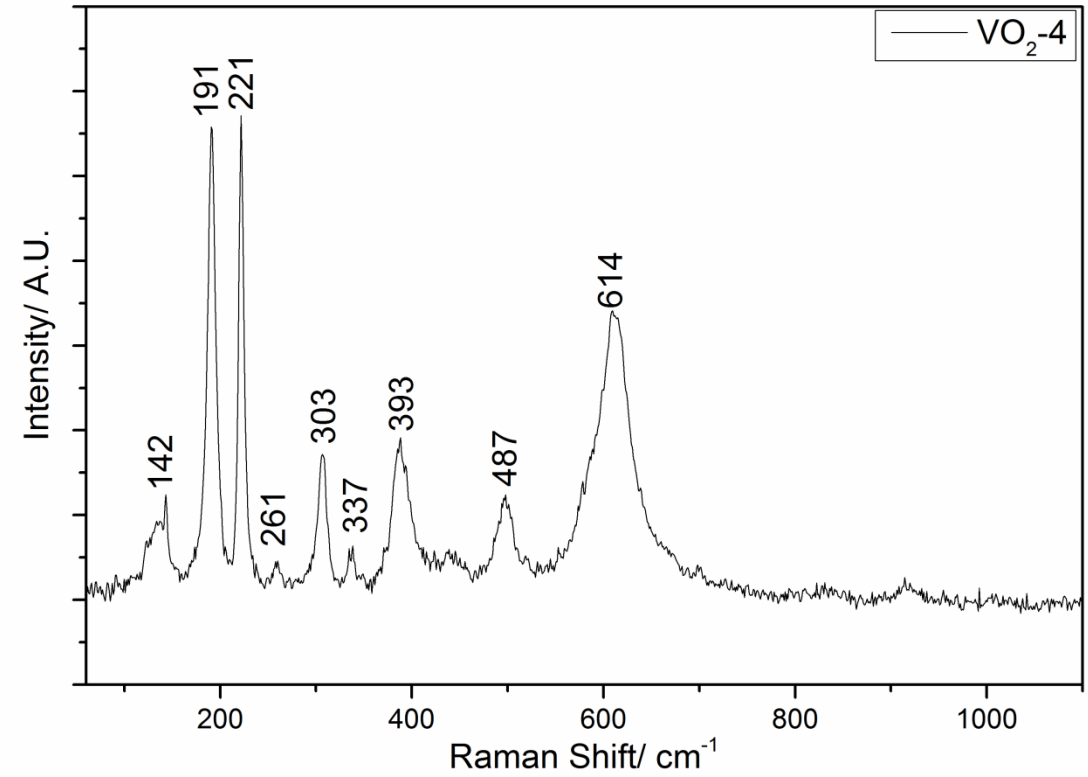

Figure 2.03: Typical Raman spectrum for VO_2 thin film deposited by APCVD.

From all the Raman spectra the only phase identified was monoclinic VO_2, there were no other primary phases (V_2O_3 and V_2O_5) or Magneli phases identified. From the XRD and Raman data, it can be concluded that phase pure monoclinic VO_2 can be deposited by the reaction of VCl_4 with ethyl acetate at 550 °C, although the XRD intensities suggest that the material is poorly crystalline.

2.3.3 Morphology, growth mechanisms and growth rate

Scanning Electron Microscopy was employed to determine the morphology, likely growth mechanisms and growth rates of the deposited films.

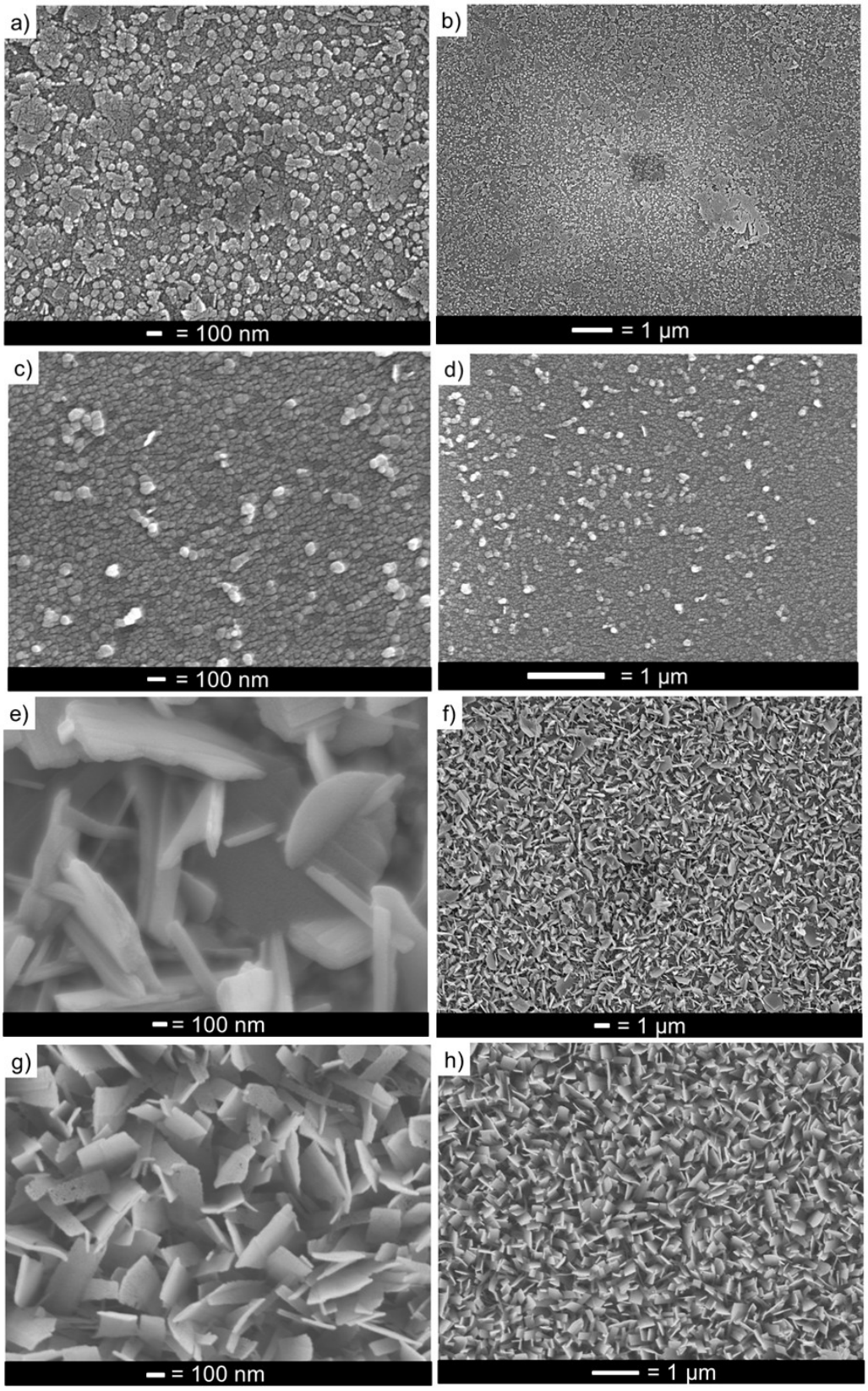

Figure 2.04: SEM images for VO_2 films synthesised from APCVD; **a)** and **b)** 15 second deposition, sample VO_2-1, **c)** and **d)** 30 second deposition, sample VO_2-2, **e)** and **f)** 1 minute deposition, sample VO_2-3, **g)** and **h)** 3 minute deposition, sample VO_2-4.

The initial growth of the VO_2 films, as shown in figure 2.04 (a) and (b), suggests that a Stranski-Krastanov mechanism is the most likely way in which the VO_2 films grow in the reaction between VCl_4 and ethyl acetate.[63] This is suggested by the mixture of layer like structures and island formations in the film. After 30 seconds, it can be clearly seen in the SEM image that an island type morphology is dominant. The films have also become less homogeneous at the larger scales, with figure 2.04 (d) showing that some of the islands are growing more quickly than their neighbours. After 1 minute deposition time, the only morphology present is a plate-like structure (figure 2.04 (e)). The film is now significantly rougher, as shown in figure 2.04 (f). The morphology of the thickest VO_2 film is shown in figure 2.04(g) and (f). The morphology is similar to that seen in the 1 minute VO_2 film, however, there is more hierarchical structuring in the thicker sample. It is also interesting to note that the particle sizes and morphology are more uniform in the 3 minute VO_2 film when compared to the 1 minute VO_2 film. This suggests that as the deposition length increases, there are competing factors to the orientation and growth of the film, with the longer deposition times favouring the formation of a more hierarchical morphology. There is also a definitive direction in the growth of the plate-like structures seen in the thicker sample, this was not apparent in the 1 minute sample.

Taking all the SEM images together suggests that under the deposition conditions, there is a time dependence to the morphology present in the sample. With shorter deposition lengths favouring small, island type formations and smoother films, whereas longer deposition lengths favour large, plate like structures and rougher films.

Island formations have been previously observed for VO_2 films deposited by the reaction of VCl_4 and H_2O under APCVD conditions.[58] The plate-like structures were not observed in this study, but this could be due to the mass-flow rate of precursors into the reactor, as the use of ethyl acetate as the oxygen precursor results in much higher mass transport due to higher vapour pressures.

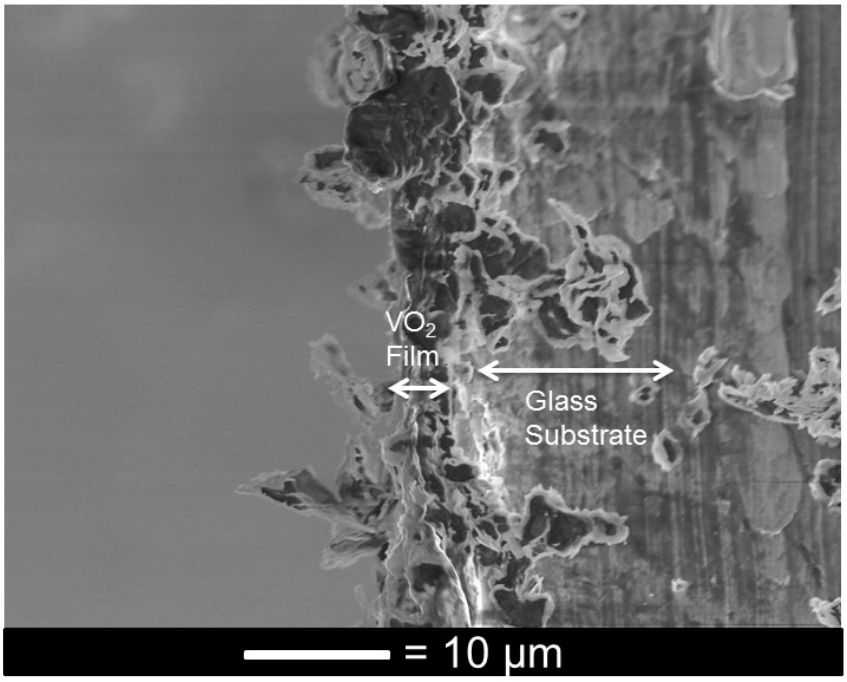

Figure 2.05: Side on SEM image for 3 minute VO_2 film on glass, sample VO_2-4. The surface roughness is demonstrated by the crystal growth from the surface of the film, with average heights of ~10 µm above the film. The average film thickness is ~1 µm.

Side on SEM images were obtained for the 3 minute VO_2 film, figure 2.05. The surface roughness of the thicker VO_2 samples is even more apparent in this image, with crystal structures extending ~10 µm from the surface of the film. This is indicative of a Stranski-Krastanov type growth mechanism. Once the original layer is deposited the VO_2 has appears to have a stronger adherence to itself than the glass substrate, resulting in the large formations apparent in the side on SEM image. This would help to explain why the films were poorly adherent and easily removed by lightly rubbing with a cloth.

The main film can also be seen in the image, with a thickness of ~1 µm. This gives a growth rate of ~350 nm min^{-1} for the VO_2 films grown.

2.3.4 X-ray Photoelectron Spectroscopy

To determine the oxidation state of the vanadium in the as deposited VO_2 thin films, X-ray Photoelectron Spectroscopy (XPS) measurements were obtained. The binding energies for all elements were measured against carbon C1s (285.0 eV).

The surface vanadium oxidation state, as shown in figure 2.06, was a mixture of V^{5+} (517.2 eV) and V^{4+} (515.7 eV). These values have been previously quoted for vanadium oxide species in the literature.[166] This is not a surprising result, as surface vanadium species will readily oxidise, and has been previously observed for monoclinic VO_2 thin films.[180]

Sputtering of the films revealed that below the surface, the bulk of the film still contained a mixture of V^{4+} and V^{5+} species, figure 2.07. Although there is still vanadium 5+ present, it is difficult to determine the relative proportions of 4+ to 5+ due to the known loss of oxygen from a crystal lattice when etching films. It can be demonstrated, however, that there is vanadium present throughout the structure of the film.

The relatively large proportion of V^{5+} species at the surface meant that the oxygen XPS signals had a large O-V^{5+} component. After ion etching, Figure 2.08, there is still a large O-V^{5+} component to the deconvoluted O1s XPS spectrum, but it can be seen that there is also a O-V^{4+} component to the signal- suggesting that there is VO_2 present in the sample. The additional environment present in the spectrum is attributed to hydroxyl groups.

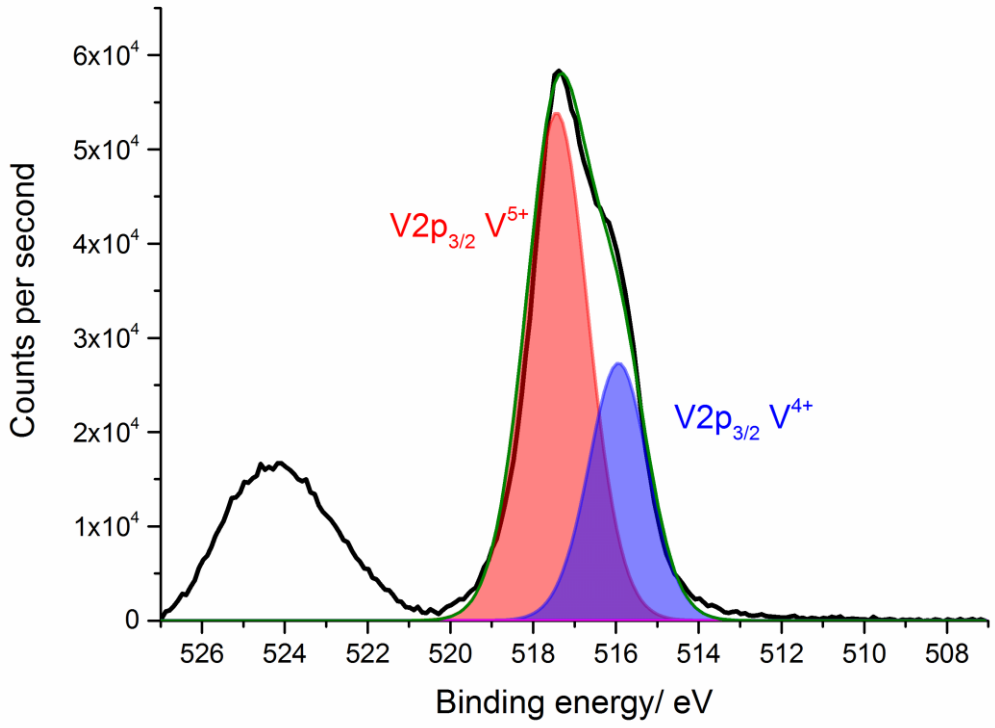

Figure 2.06: Surface XPS spectrum for vanadium binding energy from VO_2 thin film, deposited by reaction of VCl_4 and ethyl acetate by APCVD at 550 °C.

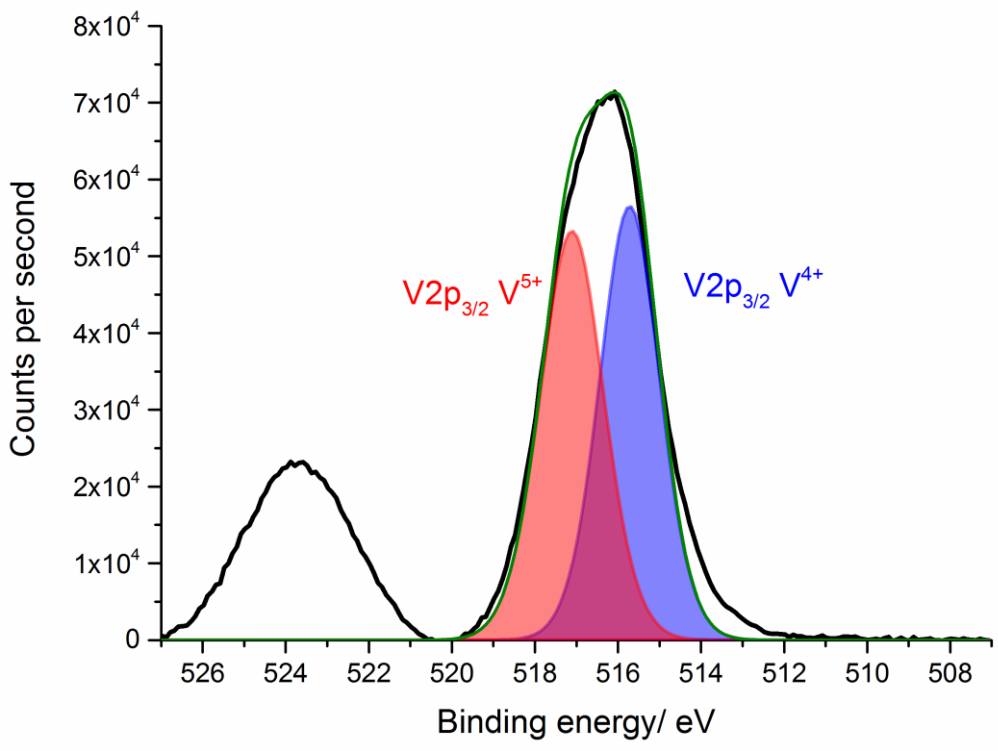

Figure 2.07: V2p XPS spectrum after ion etching for 30 secs for VO_2 thin film, deposited by reaction of VCl_4 and ethyl acetate by APCVD at 550 °C.

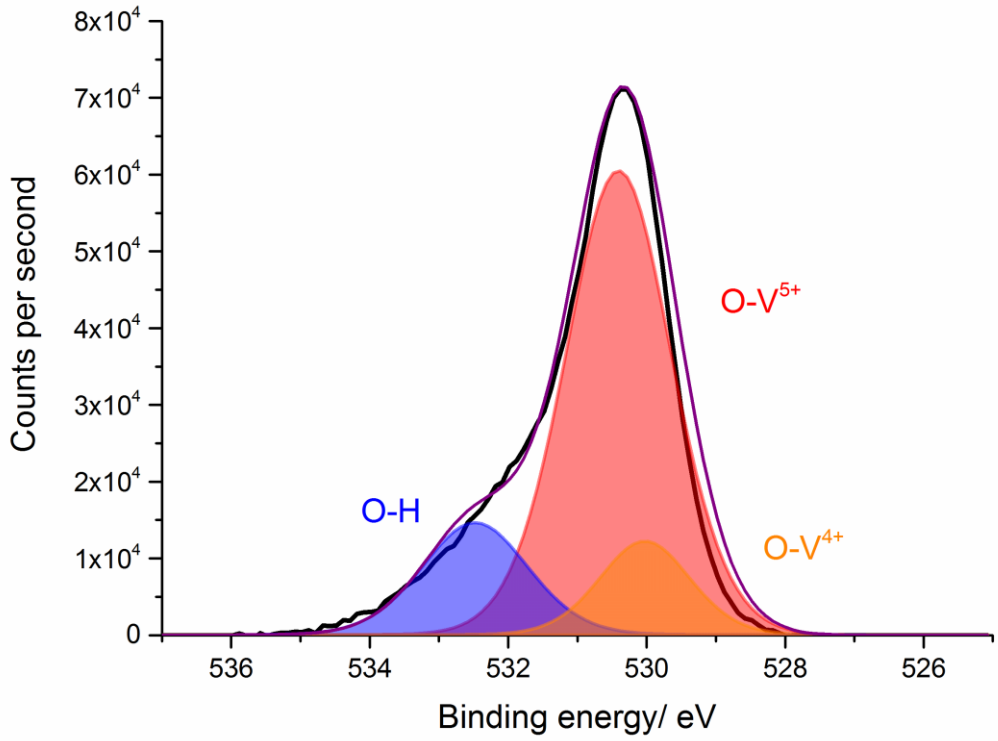

Figure 2.08: Typical O1s XPS spectrum for VO_2 thin film, after 30 s of ion etching, deposited by reaction of VCl_4 and ethyl acetate by APCVD at 550 °C.

2.3.5 Thermochromic properties of VO_2 thin films

Variable temperature UV/Vis/NIR spectroscopy was employed to probe the thermochromic properties of the deposited VO_2 films. It is clear from the variable temperature UV/Vis transmission spectra (figure 2.09) that all the samples produced are thermochromic as the transmission of the films decrease when heated past the MST phase transition. All samples showed a reversible switch, returning to their original transmission values when left to cool to room temperature.

Previous groups have published on the deposition of VO_2 thin films. Blackman *et al*. reported on the deposition of monoclinic VO_2 by APCVD.[181] In this study it was found that films of ~80 nm thickness displayed a 35% switch in transmission at 2500 nm. Binions *et al*. have also reported on the deposition of monoclinic VO_2 by APCVD.[163] In this study films below 80 nm thickness displayed switching of up to 25% at 2500 nm, films thicker than 80 nm showed a switch of between 25-50% in transmission at 2500 nm. Manning *et al.* have reported on the synthesis of VO_2 from APCVD.[32] In this study, typically the thin films showed a switch of 30% at 2500 nm, with one film showing a switch of 45% in transmission at 2500 nm. The samples described here show switching at 2500 nm of 10%, 20%, 25% and 50% for samples VO_2-1 to VO_2-4 respectively. It can be seen that although the thinner of the samples show a smaller switch than achieved by Blackman *et al*. the other values compare well with previously reported switching behaviour for VO_2 thin films deposited by APCVD.

Although the UV/Vis data clearly shows the thermochromic switching behaviour of the samples, it is unclear which of the samples has the highest solar modulation. Due to the fact that the Earth's atmosphere absorbs certain wavelengths more strongly than others, one way to determine the modulation of thermochromic films is to apply weighted solar values to the data.[134, 182, 183] The weighted solar spectrum is shown in figure 2.10. This accounts for ~99% of terrestrial solar energy, so is a good measure of the effectiveness of the switching in the films.

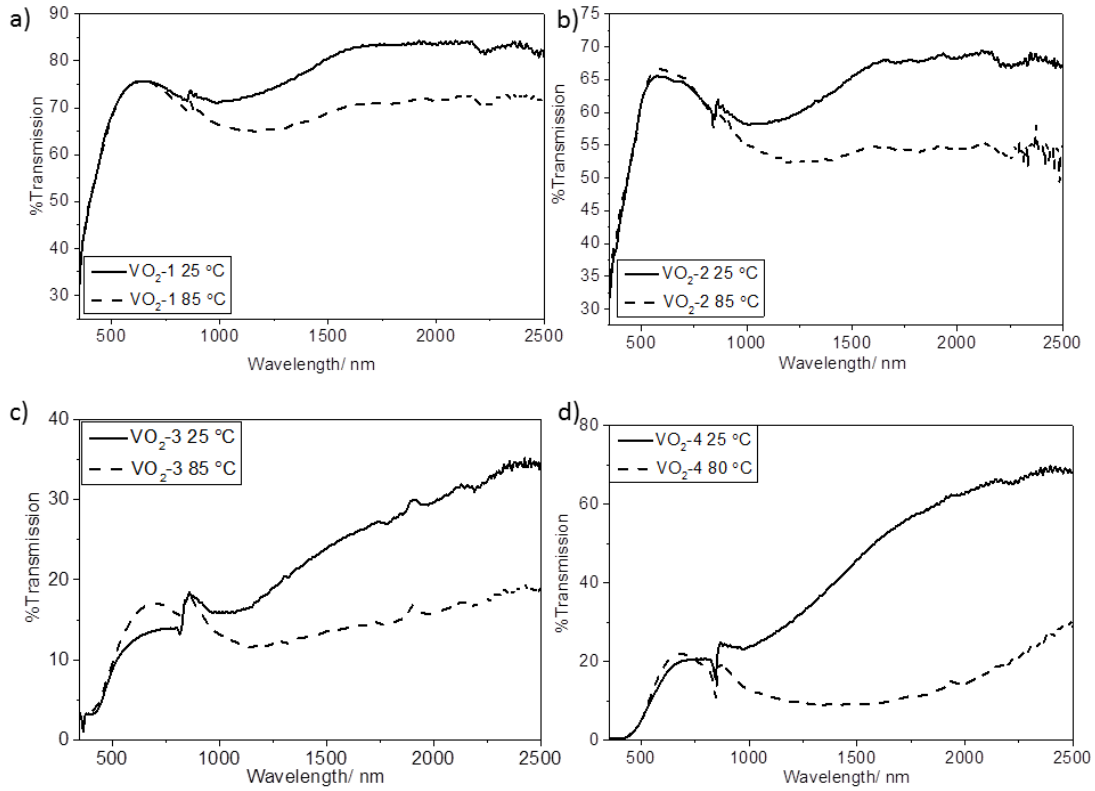

Figure 2.09: Variable temperature transmission UV/Vis spectra for **(a)** 15 second VO_2 film, sample VO_2-1, **(b)** 30 second VO_2 film, sample VO_2-2, **(c)** 1 minute VO_2 film, sample VO_2-3 and **(d)** 3 minute VO_2 film, sample VO_2-4. All samples produced by reaction of VCl_4 and ethyl acetate by APCVD at 550 °C.

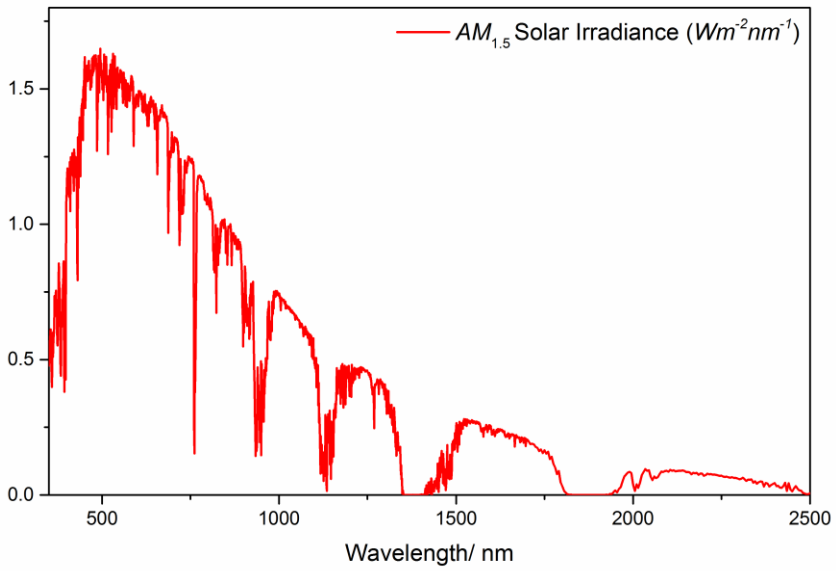

Figure 2.10: Weighted solar spectrum showing relative proportions of wavelengths that reach the Earth's surface through the atmosphere.

The solar modulation values can be obtained from equation 2.4.

$$T_{sol}^{\sigma} = \frac{\int_{\lambda=350\,nm}^{2500\,nm} AM_{1.5}(\lambda)T^{\sigma}(\lambda)d\lambda}{\int_{\lambda=350\,nm}^{2500\,nm} AM_{1.5}(\lambda)d\lambda} \qquad (2.4)$$

Where:

T_{sol}^{σ} = Solar averaged transmittance

λ = Wavelength of light (between 350 and 2500 nm)

$AM_{1.5}$ = Weighted solar irradiance spectrum, at a tilt angle of light on a south facing surface at 37° from horizontal

T^{σ} = Transmission of VO_2 thin film either hot (85 °C) or cold (25 °C)

To normalise the solar averaged transmittance, equation 2.5 is used:

$$\Delta T_{sol} = T_{sol}^{cold} - T_{sol}^{hot} \qquad (2.5)$$

Where:

ΔT_{sol} = The % transmission difference between the cold and hot states

T_{sol}^{cold} = The weighted transmission of the VO_2 film in the cold state

T_{sol}^{hot} = The weighted transmission of the VO_2 film in the hot state

%Solar modulation for the samples is summarised in table 2.2.

Sample	Weighted Solar Modulation (%)
VO_2-1	4.83
VO_2-2	4.13
VO_2-3	3.15
VO_2-4	14.1

Table 2.3: %Solar modulation for VO_2 thin film samples

A value of 15% change in solar modulation is a very large change for a vanadium (IV) oxide thin film.[182] This shows that the best performing single component thin films have to be thick to achieve the greatest change from the hot and cold states. It can be seen from the UV/Vis spectra that this type of modulation comes with the

penalty of very low visible light transmittance due to the dark yellow/brown colour of the deposited film.

The surprising result was the effectiveness of the thinnest VO_2 film, sample VO_2-1. When compared to the next two thicker film samples, it has a higher overall change than either sample VO_2-2 or VO_2-3. This suggests that as the film thickness is increased there is an initial region where the thermochromic properties, when weighted against the terrestrial solar spectrum, are poorer. Eventually when the film is thick enough, this is suppressed by a much larger switch, in near IR wavelengths, between the hot and cold states.

As with the weighting applied to the thermochromic effect of the films, a weighting should also be applied to the visible light transmission of a spectrum. This is due to the ability of the human eye to perceive and differentiate between different wavelengths and intensities.[184] This produces a bell-shaped curve centred on a wavelength of 580 nm. This measure is known as the *photopically averaged transmittance* T_{lum}.[185]

T_{lum} values can be obtained from:

$$T_{lum}^{\sigma} = \int_{\lambda=350\ nm}^{780\ nm} \bar{y}(\lambda) T^{\sigma} d\lambda / \int_{\lambda=350\ nm}^{780\ nm} \bar{y}(\lambda) d\lambda \quad (2.6)$$

Where:

T_{lum}^{σ}= Photopically averaged transmittance

λ =Wavelength of light (between 380 and 780 nm, the limits of human vision)

$\bar{y}(\lambda)$ = Photopic luminous efficiency of human eye

T^{σ} = Transmission of VO_2 thin film either hot (85 °C) or cold (25 °C)

As with the solar averaged data, the difference between the hot and cold states could also be determined by:

$$\Delta T_{lum} = T_{lum}^{cold} - T_{lum}^{hot} \quad (2.7)$$

Where:

ΔT_{lum} = The % difference between the visible light transmission between the hot and cold states

T_{lum}^{cold} = The weighted visible light transmission of the cold state

T_{lum}^{hot} = The weighted visible light transmission of the hot state

Sample	T_{lum}^{cold}	T_{lum}^{hot}	ΔT_{lum}
VO_2-1	73.04 %	72.98 %	0.06 %
VO_2-2	64.47 %	65.31 %	-0.85 %
VO_2-3	11.15 %	13.29 %	-2.14 %
VO_2-4	11.80 %	13.53 %	-1.74 %

Table 2.4: % weighted visible transmission for cold (25 °C) and hot (85 °C) VO_2 films and %change in transmission between cold and hot states.

It can be seen from Table 2.4 that the best film in terms of visible light transmission is the thinnest VO_2 film. This film also has the lowest %change between the hot and cold states, which is important as the thermochromic film should not show a visible change when the material is switching between the semi-conducting and semi-metallic states.

Interestingly, the worst performing film for both the solar modulation and visible light transmission values is sample VO_2-3. This is a surprising result as this is an intermediate film thickness and it would be expected that the solar modulation and visible light transmission values would reflect this. Whilst the thickest of the VO_2 films, sample VO_2-4, shows poor visible light properties, it is surprising to note that there does not appear to be a linear relationship between film thickness and visible light transmission. This suggests that there is a region where the visible light transmission remains reasonably constant, but the thermochromic properties can be improved.

The UV/Vis spectra were also used to obtain hysteresis loops for the phase change from monoclinic to tetragonal. For the three thicker samples, the change was abrupt and occurred at ~68 °C, which is the temperature associated with undoped VO_2 thin films.[1] The exception was the thinnest of the VO_2 films deposited, sample VO_2-1, which showed a reduced phase transition temperature.

Figure 2.11(a) shows the UV/Vis transmission spectra for the sample as it is heated from 25 to 70 °C and the hysteresis data is shown in figure 2.11(b), showing both the heating and cooling of this sample. The UV/Vis spectra show that the change from the highly transmissive monoclinic to the less transmissive tetragonal phase is

occurring over a large temperature window. This has been previously observed in thin films of VO_2 and has been attributed to reductions in crystallite size and the orientation of the particles in the film.[186, 187] Smaller crystallite sizes lead to a greater number of defects in the structure, these defects then act as 'nucleation' sites for the relief of stress through atomic rearrangements.[188] As the thinnest VO_2 film has both small crystallite sizes and a disordered crystal structure, it is expected to suffer from the widest hysteresis between the monoclinic and tetragonal phases. The hysteresis width unfortunately would make these films unsuitable for energy efficient coatings, as an abrupt change from transmissive to reflective is desirable for comfort.[1, 16, 151]

Although sample VO_2-1 had a wide hysteresis, it can also be demonstrated from the hysteresis curve that complete phase transformation had occurred by 60 °C, with significant switching (~10% change from cold state) by 50 °C. This is a large reduction from the other undoped samples.

There have been previous reports that very thin films, below 100 nm thickness, have reductions in the MST phase transition,[15, 135] which has been attributed to strain within the film.[59, 137] As the film deposited here is below 100 nm in thickness, it is highly likely that the reduction in the MST phase transition is due to the strain inherent in the film, favouring the adoption of the less strained tetragonal crystal structure.

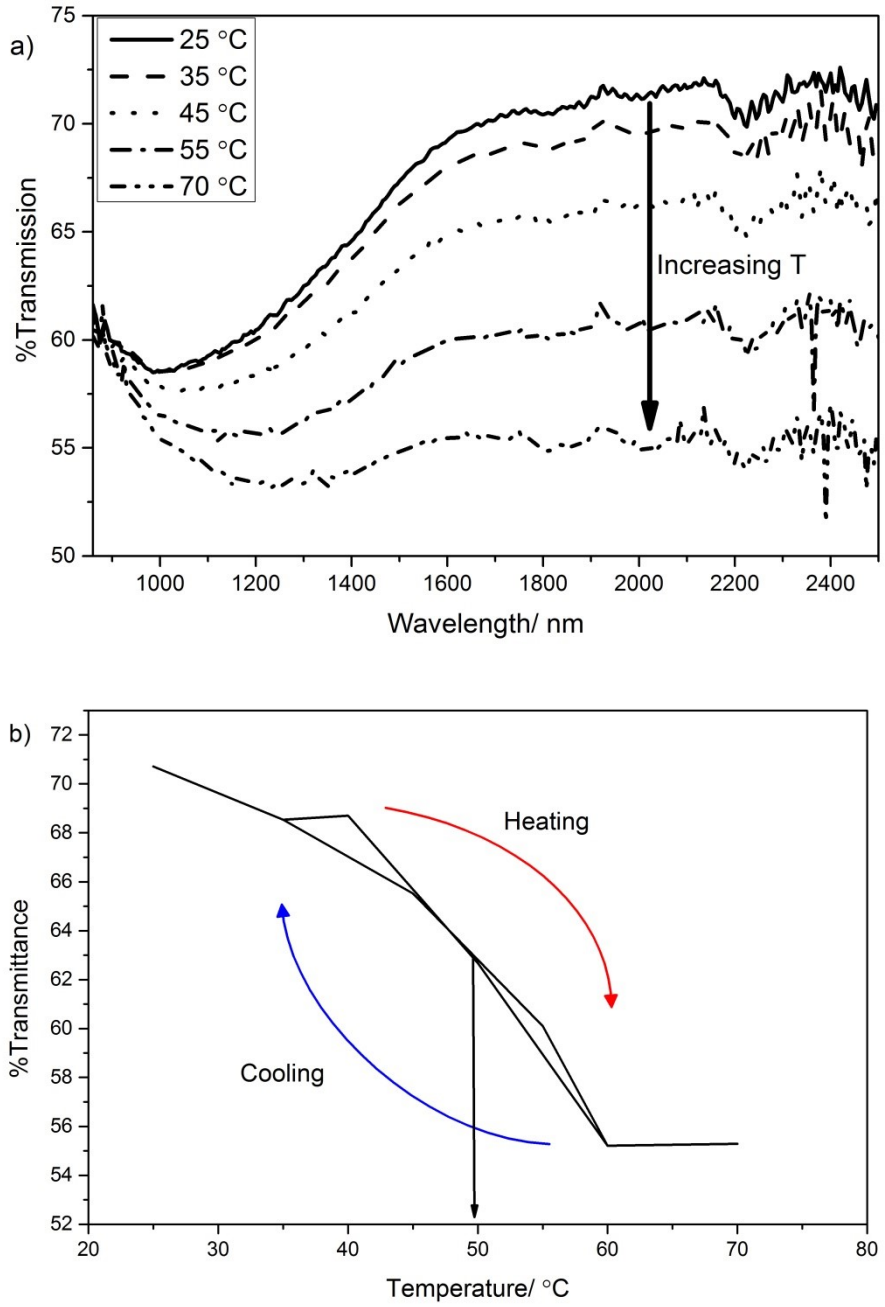

Figure 2.11: (a) Variable temperature UV/Vis spectra showing the change in near IR wavelengths as sample VO_2-1 is heated from 25 to 70 °C and **(b)** hysteresis switching curve at 2500 nm for both heating and cooling of sample VO_2-1.

Previous APCVD depositions of monoclinic VO_2 thin films had used water as the oxygen source,[32, 57, 58, 168] or $[VO(acac)_2]$ with a stream of 2% O_2 in N_2.[161, 163] Due to the higher mass flow rates used in the reaction between VCl_4 and ethyl acetate, the film growth rates were ~350 nm min^{-1}, which is substantially faster than $[VO(acac)_2]$ reactions which had growth rates of ~40 nm min^{-1},[161] but comparable to VCl_4/H_2O

reactions which had growth rates of ~300 nm min^{-1}.[57] The deposition temperature used in the reactions in this chapter was 550 °C, which is higher than either of the quoted APCVD reactions above, which were at or below 500 °C. The thermochromic response recorded from the films deposited by the reaction of VCl_4 and ethyl acetate were higher than those deposited by VCl_4/H_2O or $[VO(acac)_2]$, this is likely due to the higher deposition temperature increasing the crystallinity of the deposited films.

2.4 Conclusions

The method reported in this chapter has demonstrated the reaction VCl_4 and ethyl acetate to synthesise high quality VO_2 films. The deposition of thermochromic VO_2 thin films has been shown to be highly reproducible. When comparing the reaction of $TiCl_4$ and VCl_4 it was found that VCl_4 required a lower concentration of ethyl acetate which was attributed to the higher rate of thermally induced decomposition of the VCl_4. The ratio of VCl_4 and ethyl acetate also affected the carbon contamination of the film produced, as assessed by eye. A ratio of 2:1 VCl_4 : ethyl acetate found to give the best films when assessed by eye, whilst also maintaining the thermochromic behaviour. The deposition temperature was found to not have a large effect on the phase of vanadium oxide formed, but did affect the colour with lower temperatures resulting in darker films when inspected by eye.

The thickness of the films could be easily controlled by varying the deposition time, with thicknesses below 100 nm achieved. The thinnest film showed extremely high visible light transmission, whilst still maintaining a solar modulation comparable to films that were significantly thicker, which was a very surprising result and demonstrates that APCVD can be used to produce high quality films with thicknesses <100 nm. The thinner films, however, suffered from widening of the hysteresis (~20 °C) between the monoclinic and tetragonal phases, which is an issue for their application as energy efficient coatings. The thickest VO_2 film showed the greatest solar modulation between the hot and cold states, but this came at the expense of poor visible light transmission, which once again prevents their use for energy efficient coatings on windows.

The microstructure of the films showed a dramatic change from the thinnest through to the thickest, with a change from a disordered layer/island formation in the thin films to a much more ordered plate-like structure in the thicker films. This change

was accompanied by a greater surface roughness and poorer substrate adhesion- as demonstrated by the ease of removing the films by lightly rubbing.

If the high visible light transmission of the very thin films could be combined with the high solar modulation and small hysteresis of the thicker films, it would be a significant step towards the utilisation of CVD techniques to produce high quality thermochromic coatings for energy efficient applications. Demonstrated in the next chapter is a method for producing multi-layered $VO_2/SiO_2/TiO_2$ systems from APCVD, which allows improved visible light transmission to be achieved along with high solar modulation when compared to single film VO_2 analogues.

Chapter 3

Multi-layered $VO_2/SiO_2/TiO_2$ films by Atmospheric Pressure Chemical Vapour Deposition

Chapter 3: Multi-layered $VO_2/SiO_2/TiO_2$ films by Atmospheric Pressure Chemical Vapour Deposition

3.1 Introduction

Due to the aesthetically unattractive brown/yellow colour and poor visible light transmission of VO_2 thin films, there has been wide ranging research into how to lessen the colour and increase the transmission of visible wavelengths. Successful strategies have included the doping of Mg into VO_2,[30, 134] core-shell nanoparticles[153, 189, 190] and multi-layered thin films,[151, 160, 191] where the VO_2 is 'sandwiched' with alternating layers of a dielectric material, such as SiO_2.

With the above mentioned routes to diminishing both the haze and colour of the films, the multi-layered thin films offer a further advantage. These films can increase the visible light transmission,[145, 192] help to alter the colour of the VO_2 films[160, 193] and give other functionalities, such as self-cleaning[194, 195] or increased conductivity.[196, 197] The synthesis of such multi-functional thin films is therefore an area that is increasingly being researched.

Granqvist *et al*. have reported on the multi-layered VO_2/SiO_2 systems from magnetron sputtering.[160] It was found that the inclusion of the SiO_2 layer lessened the haze from the films by altering the refractive index. There have also been modelling on these types of multi-layered systems demonstrating that the colour and visible light transmission of the films is dependent on the thicknesses of the different layers.[133, 183]

Multi-layered VO_2 films have also been synthesised by the incorporation of nanoparticles, synthesised by hydrothermal methods, into polymers which are then spin coated into layers.[145, 192, 198] Here it was found that the visible light transmission was increased with the addition of multi-layers.

The above synthetic routes suffer from difficulties in scaling for industrial purposes, so ideally a route, such as chemical vapour deposition, would be used to produce multi-layered VO_2 films. APCVD has been previously demonstrated for combinatorial layers of VO_2/TiO_2,[143, 144] but has never been demonstrated for multi-layered $VO_2/SiO_2/TiO_2$ systems.

3.1.1 The Atmospheric Pressure Chemical Vapour Deposition reactor

The APCVD syntheses reported here were deposited on a horizontal cold-walled reactor. (The reactor design is the same as shown schematically in chapter 2, figure 2.01). The precursors were contained in bubblers under nitrogen (N_2) gas flow, which was used as a carrier gas. The bubblers consisted of stainless steel cylinders with brass jackets and heating bands. All lines were heated using heating tapes (*Electrothermal* 400 W, 230 V). The precursors were mixed in stainless steel mixing chambers. The temperature of all components of the system was controlled by k-type thermocouples with *Thermotron* controllers.

3.2 Synthesis of multi-layered $VO_2/SiO_2/TiO_2$ thin films

3.2.1 Aim

To determine whether multi-layered films of $VO_2/SiO_2/TiO_2$ can be synthesised by APCVD. To determine the thermochromic properties of these multi-layers and compare against single layer VO_2 analogues. To determine whether there is a change in the visible light transmission of the films by the inclusion of multi-layers. To determine whether the multi-layered films show self-cleaning, as well as thermochromic, properties.

3.2.2 Experimental

For the following reactions the vanadium precursor source used was vanadium (IV) chloride (VCl_4, 99.9%), the oxygen precursor source used was ethyl acetate anhydrous ($C_4H_8O_2$, 99.8%), the silicon precursor used was tetraethyl orthosilicate ($Si(OC_2H_5)_4$, 98%) and the titanium precursor used was titanium (IV) chloride ($TiCl_4$, 99.9%), all precursors were purchased from *Sigma Aldrich UK*. All chemicals were used without additional treatment. Glass-substrates consisted of a 3.4 mm silica coated barrier glass (50 nm SiO_2 layer) obtained from *Pilkington*. The glass substrate was 90 x 300 mm. Prior to deposition all substrates were cleaned with acetone, 2-propanol and water and left to air dry. Oxygen-free nitrogen (99.9 % purity) was purchased from *BOC* and used as the carrier gas for all reactions.

For the synthesis of $VO_2/SiO_2/TiO_2$ multi-layers; VCl_4 was placed in bubbler 1, ethyl acetate was placed in bubbler 2, tetraethyl orthosilicate was placed in bubbler 3 and $TiCl_4$ was placed in bubbler 4. Bubblers 1, 2, 3 and 4 were heated to 80, 40, 130

and 75 °C respectively. This achieved a suitable vapour pressure from the precursors, as determined from the vapour pressure equation (Chapter 2, Equation 2.1). This gave mass flow rates of 0.00554, 0.00288, 0.00554 and 0.00288 mol min^{-1} for VCl_4, ethyl acetate, tetraethyl orthosilicate and $TiCl_4$ respectively.

3.2.3 Sample descriptions for multi-layer $VO_2/SiO_2/TiO_2$ thin films

In a typical synthesis, the reactor would be set to 550 °C (ramp rate 7 °C min^{-1}). The plain N_2 gas flow set to 20 L min-1 and the plain flow lines heated to 200 °C. The mixing chamber was set to 150 °C. For the deposition of VO_2; the VCl_4 bubbler was set to 80 °C and had a N_2 gas flow set at 0.7 L min^{-1} and the $C_4H_8O_4$ bubbler was set to 40 °C and had a N_2 gas flow set at 0.2 L min^{-1}. For the deposition of SiO_2; the tetraethyl orthosilicate bubbler was set to 130 °C and had a N_2 gas flow of 0.7 L min^{-1}, and the $C_4H_8O_4$ was set to 40 °C and had a N_2 gas flow of 0.2 L min^{-1}. For the deposition of TiO_2, the $TiCl_4$ bubbler was set to 75 °C and had a N_2 gas flow of 0.6 L min^{-1} and the $C_4H_8O_4$ was set to 40 °C and had a N_2 gas flow of 0.6 L min^{-1}. Depositions of each individual layer would last between 1 and 3 minutes.

In a typical multi-layered film synthesis, the 4 bubblers would all be opened to allow the nitrogen carrier gas to flow through the precursor. When an individual layer was being deposited, the precursors would be switched, from flowing to the exhaust to the reaction chamber, by use of a three-way valve. After the deposition length had passed the precursor feeds would be switched back to flowing to the exhaust. In this way it was possible to synthesise multiple layers of different materials. After all the layers had been synthesised, the bubblers would be switched back, so that the nitrogen carrier gas no longer flowed through the precursors.

After a deposition, the sample would be left to cool under a flow of nitrogen and would only be removed when the temperature was below 90 °C. Sample descriptions and synthesis conditions are summarised in Table 3.1 (for single layered films) and Table 3.2 (for multi-layered films). The thin films were characterised as deposited, there was no post-treatment of any of the films.

Name	Sample Description	Precursors	Temp (°C)	Flow rate (L min^{-1})	Deposition Length (min)
V-1	VO_2 Single layer 1 min deposition	VCl_4 $C_4H_8O_4$	80 40	0.7 0.2	1
V-3	VO_2 Single layer 3 min deposition	VCl_4 $C_4H_8O_4$	80 40	0.7 0.2	2

Table 3.1: Sample descriptions and deposition lengths for single layered VO_2 depositions on glass substrates by APCVD.

Name	Sample Description	Layer	Precursors	Temp (°C)	Flow rate (L min^{-1})
VST-1	$VO_2/SiO_2/TiO_2$ Multilayer 1 min deposition of each layer	VO_2	VCl_4 $C_4H_8O_4$	80 40	0.7 0.2
		SiO_2	$Si(OC_2H_5)_4$ $C_4H_8O_4$	130 40	0.7 0.2
		TiO_2	$TiCl_4$ $C_4H_8O_4$	75 40	0.6 0.6
VST-3	$VO_2/SiO_2/TiO_2$ Multilayer 3 min deposition of VO_2 and SiO_2 layers, 1 min deposition of TiO_2 layer	VO_2	VCl_4 $C_4H_8O_4$	80 40	0.7 0.2
		SiO_2	$Si(OC_2H_5)_4$ $C_4H_8O_4$	130 40	0.7 0.2
		TiO_2	$TiCl_4$ $C_4H_8O_4$	75 40	0.6 0.6

Table 3.2: Sample descriptions for multi-layered films of $VO_2/SiO_2/TiO_2$ synthesised on glass substrates by APCVD.

3.2.4 Film Characterisation

X-ray diffraction (XRD) studies were carried out using a Bruker-Axs D8 (GADDS) diffractometer. The instrument operates with a Cu X-ray source, monochromated ($K\alpha_1$ and $K\alpha_2$) and a 2D area X-ray detector with a resolution of 0.01º (glancing incident angle, θ = 0.3º). The diffraction patterns obtained were compared with database standards from the Inorganic Crystal Structure Database (ICSD), Karlsruhe, Germany. UV/vis spectroscopy was performed using a Perkin Elmer Lambda 950 UV/Vis/NIR Spectrophotometer. The transmission spectra were recorded directly on the films as deposited, held in a specially designed heating cell allowing the beam to pass through the sample directly into the integrating sphere. A *Labsphere* reflectance standard was used as reference in the UV/vis measurements. The heating of the samples for thermochromic measurements in the UV/Vis spectrometer was achieved by an aluminium temperature cell controlled by RS cartridge heaters, Eurotherm temperature controllers and k-type thermocouples. Scanning electron microscopy (SEM) was carried out using a Jeol JSM-6700F and secondary electron image on a Hitachi S-3400N field emission instruments (20 KV) and the Oxford software INCA. X-Ray photoelectron spectroscopy (XPS) was performed using a Thermo Scientific K-alpha spectrometer with monochromated Al Kα radiation, a dual beam charge compensation system and constant pass energy of 50 eV (spot size 400 μm). Survey scans were collected in the range 0-1200 eV. XPS data was fitted using CasaXPS software, the vanadium and titanium $2p_{3/2}$ and Si 2p peaks were modelled with Gaussian functions. The Gaussian functions had a FWHM value of 1.8, 1.7, 1.9 and 1.2 for V^{5+}, V^{4+}, Ti^{3+}/Ti^{4+} and Si^{4+} respectively (with a tolerance of ±0.2) these values were obtained from literature measurements.[166, 199, 200]

3.2.5 Photocatalytic testing

For the evaluation of their photocatalytic activity, samples had a layer of stearic acid applied by dip-coating from a chloroform solution (0.05 M). The samples were left to air dry for ~15 mins. The degradation of the acid was monitored by infrared spectroscopy (2700 – 3000 cm^{-1}) using a *Perkin Elmer RX-I* Fourier transform infrared spectrometer. The samples were irradiated in a home-built light box equipped with six blacklight blue fluorescent tubes (UVA 6×18W) and an extractor fan. The irradiance (4 ± 0.2 mW cm^{-2}) at sample position was measured using a *UVX* radiometer (*UVP*). The area of the sample under illumination was 3.14 cm^2.

3.3 Results and discussion

Multi and single layered films of VO_2 were deposited under APCVD conditions by the reaction of vanadium, silicon and titanium precursors with ethyl acetate. In all cases the ethyl acetate acted as the oxygen source for the reactions.

$$VCl_4 + C_4H_8O_2 \rightarrow VO_2 + \text{by-products} \quad (3.1)$$

$$Si(OC_2H_5)_4 + C_4H_8O_2 \rightarrow SiO_2 + \text{by-products} \quad (3.2)$$

$$TiCl_4 + C_4H_8O_2 \rightarrow TiO_2 + \text{by-products} \quad (3.3)$$

The overall reactions are summarised in Equations 3.1, 3.2 and 3.3. As ethyl acetate is the oxygen source in each case. The most likely reaction mechanism would be as stated in Chapter 2, Equation 2.3.

3.3.1 Phase identification

XRD patterns were obtained for all the films synthesised, Figure 3.01. The single layer VO_2 films (Figure 3.01 (a)), samples V-1 and V-3, showed peaks that could be identified as monoclinic VO_2. As with the previous depositions of thin films of VO_2, the diffraction peak intensities were weak.

The multi-layered films (Figure 3.01 (b)), samples VST-1 and VST-3, showed XRD patterns consistent with the formation of TiO_2. Interestingly, the thinner of the depositions, VST-1, displayed only rutile reflections in the data, whilst the thicker multi-layer, VST-3, showed diffraction peaks that could be matched to both anatase and rutile phases. As both samples were deposited at the same temperature, this suggests that there could be a templating effect from the underlying SiO_2 favouring the formation of the rutile phase- as the SiO_2 can be seen to have columnar growth in the SEM images. This was supported by a slight shift in the peak positions for the anatase and rutile reflections, suggesting that the titania is being strained by an underlying template. It has been previously observed that the thickness of SiO_2 barrier layers can affect the phase of TiO_2 achieved from CVD methods.[201]

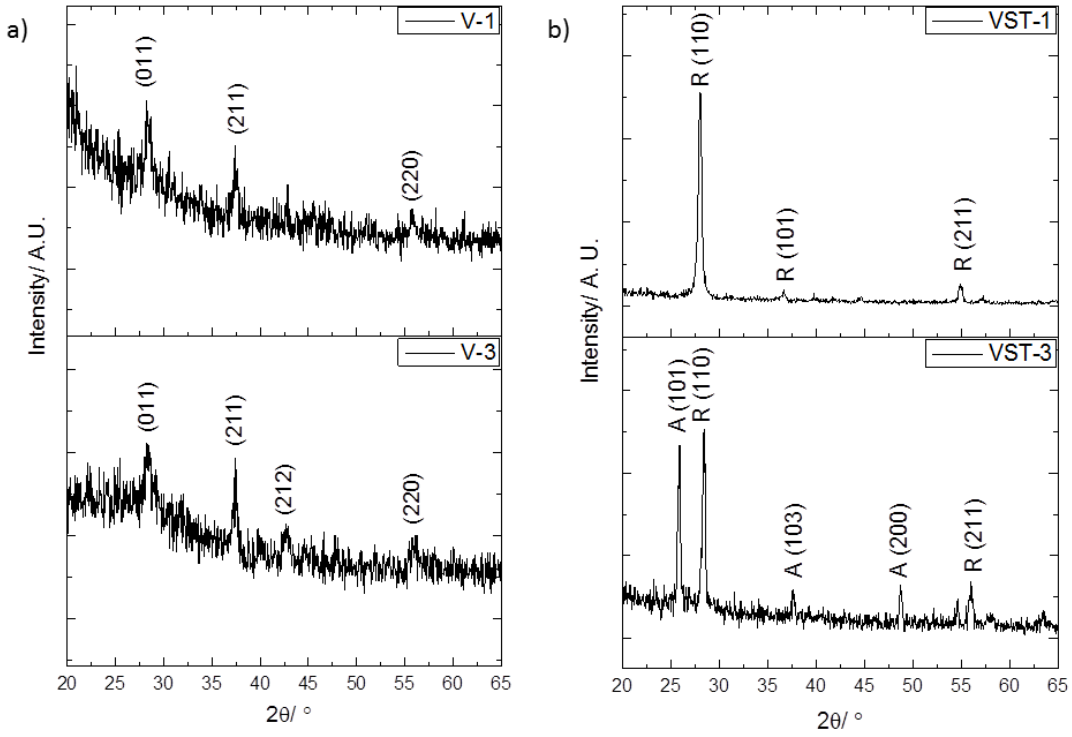

Figure 3.01: XRD patterns for **a)** single layer VO_2 thin films, V-1: 1 minute VO_2 deposition and V-3: 3 minute VO_2 deposition and **b)** Multi-layered $VO_2/SiO_2/TiO_2$ films, VST-1 1 minute deposition of VO_2, SiO_2 and TiO_2 and VST-3 3 minute depositions of VO_2 and SiO_2 and 1 minute deposition of TiO_2. The monoclinic VO_2, rutile (R) and anatase (A) planes have been identified in the XRD patterns.

3.3.2 Morphology and growth rates of deposited films

SEM images were obtained for the single and multi-layered VO_2 thin films, Figure 3.02. The as deposited single layer VO_2 films, Figure 3.02 (a) and (b), show similar morphologies to those described for films deposited under the same conditions in Chapter 2. This shows that the films deposited by the reaction of VCl_4 and ethyl acetate can be reliably reproduced.

Figure 3.02 (c) shows the structure observed in the SiO_2 layer, to observe this morphology, a film of VO_2 with an overlayer of SiO_2 was synthesised. The VO_2 and SiO_2 were synthesised under the same reaction conditions as those outlined in Table 3.1. Each layer was deposited for 1 minute at 550 °C. The morphology observed in this structure shows a very porous nature, with lots of voids evident, the voids are also large being on the order of 100s of nm in size.

Figure 3.02 (d) shows a typical morphology for the TiO_2 layer in the multi-layered films, samples VST-1 and VST-3, the particles are pyramidal in shape. This type of morphology has been previously reported for TiO_2 films deposited by APCVD methods.[169, 202] In comparison to the VO_2 and SiO_2 morphologies, the TiO_2 shows significantly reduced surface roughness in the SEM image.

Figure 3.02 (e) and (f) show side on SEM images for the thinner of the multi-layer films, sample VST-1. This is representative of the morphology observed in both the multi-layered structures. It can be seen that there are 3 distinct regions on the glass substrate; these are highlighted in Figure 3.02 (f). The VO_2 and TiO_2 layers show a dense closely packed structure, with few voids obvious. This is in comparison with the SiO_2 layer, which displays column like structures in the SEM image. When this is combined with the information from Figure 3.02 (c), it suggests that the SiO_2 is highly porous with many void regions, most likely containing air pockets.

The thicknesses of the layers from the side on SEM images also allowed growth rates to be estimated. As the film shown is sample VST-1, where each layer was deposited for 1 minute, the growth rates were estimated as; VO_2 = ~300 nm min^{-1}, SiO_2 = ~1300 nm min^{-1} and TiO_2 = ~100 nm min^{-1}. The VO_2 growth rates are comparable with the rates seen in Chapter 2.

Water contact angle measurements were obtained for all the samples deposited. Samples V-1 and V-3 showed superhydrophilic angles, both being below 2°. This was attributed to the surface roughness of each of these films as observed in the SEM images. This wetting process has been described by Wenzel.[203]

The water contact angles for the multi-layered films were between 70-90° for samples VST-1 and VST-3. These are consistent with water contact angle measurements for TiO_2 films deposited by CVD methods.[204]

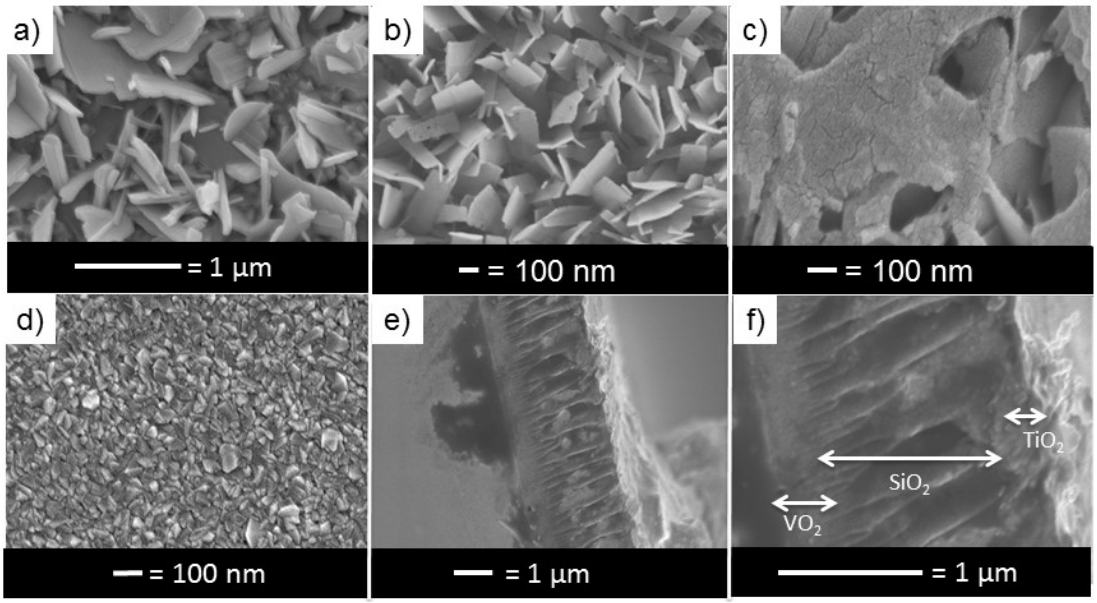

Figure 3.02: SEM images for samples top down; **a)** 1 minute VO_2 layer, V-1, **b)** 3 minute VO_2 layer, V-3, **c)** SiO_2 layer showing presence of voids within structure, **d)** typical TiO_2 film, sample VST-1, **e)** side-on SEM image showing the presence of different structures in multi-layer and **f)** magnified side-on SEM image giving information on the growth rates of each of the component layers for sample VST-1.

3.3.3 X-ray Photoelectron Spectroscopy

To determine the oxidation states of the vanadium, titanium and silicon, XPS measurements were obtained for the samples. All samples were also sputtered to elucidate the mixing of the various elements present. The binding energies for all elements were measured against carbon C1s (285.0 eV).

The single layered VO_2 samples, V-1 and V-3, had surface vanadium species that were a mixture of V^{5+} (517.16 eV) and V^{4+} (515.65 eV). As stated in the previous chapter, these are in agreement with literature values.[166] When these films were sputtered, the only vanadium signal remaining in the spectra was for V^{4+}, leading to the conclusion that the films were bulk VO_2 with surface V_2O_5 species- as concluded for the samples synthesised in Chapter 2 (Figures 2.06 and 2.07).

The multi-layered films, VST-1 and VST-3, showed more complex spectra. The only metallic species present at the surface of the films were Ti^{4+}, Figure 3.03 (a). This gave a binding energy of 485.7 eV, which is consistent with Ti^{4+} in TiO_2.[205] The multi-layered films were also sputtered to reveal the oxidation states and

concentrations of elements within the films. The titanium signals in the samples all showed a broadening of the Ti binding energy $2p_{3/2}$ peak (when sputtered) Figure 3.03 (b). This was deconvoluted to give a mixture of Ti^{4+} and Ti^{3+} in the sample.[206]

There were 2 silicon environments detected in the samples was for Si^{4+}, Figure 3.04. This gave binding energies of 103.6 eV consistent with Si^{4+} in SiO_2,[207] and 102.7 eV consistent with $SiO_{1.35}$.[208] The latter binding energy is attributed to the etching process.

To detect the vanadium species present in the samples required long sputtering times, this is attributed to the thickness of the SiO_2 layers as seen in the SEM images, Figure 3.02 (e) and (f). The vanadium species detected, Figure 3.05, showed a mixture of V^{5+} (517.2 eV) and V^{4+} (515.7 eV).

From the XPS spectra, it is confirmed that there is TiO_2 at the surface as Ti^{4+}, with the bulk being a mixture of Ti^{3+} and Ti^{4+}. The silicon in the sample is present as Si^{4+}, with the higher binding energy, at 103.6 eV, indicative of SiO_2. The vanadium is deep within the layer, supporting the SEM data, and is a mixture of V^{5+} and V^{4+}, which is consistent with the results seen in chapter 2.

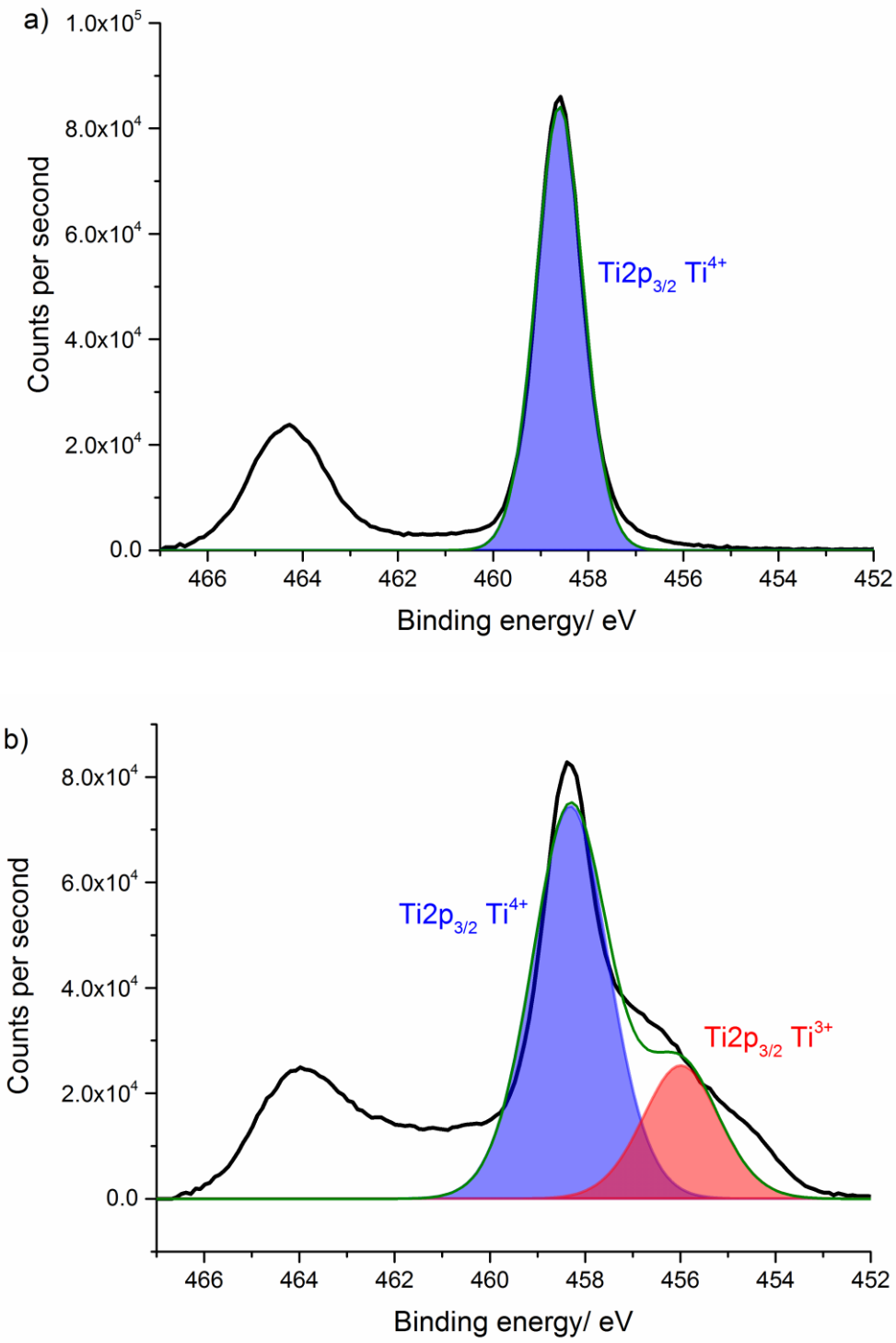

Figure 3.03: XPS spectra for titanium binding energies **a)** surface titanium species present in multi-layered film, sample VST-1 and **b)** titanium species present after etching of the film, sample VST-1.

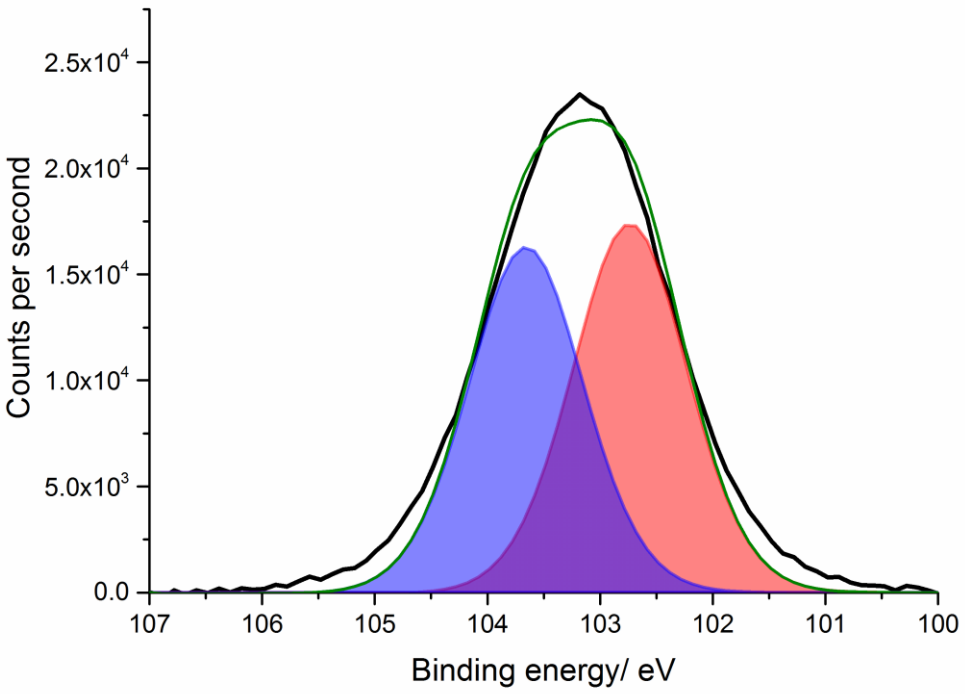

Figure 3.04: XPS spectra for silicon binding energy of silicon in SiO_2 layer of multi-layered film, sample VST-3.

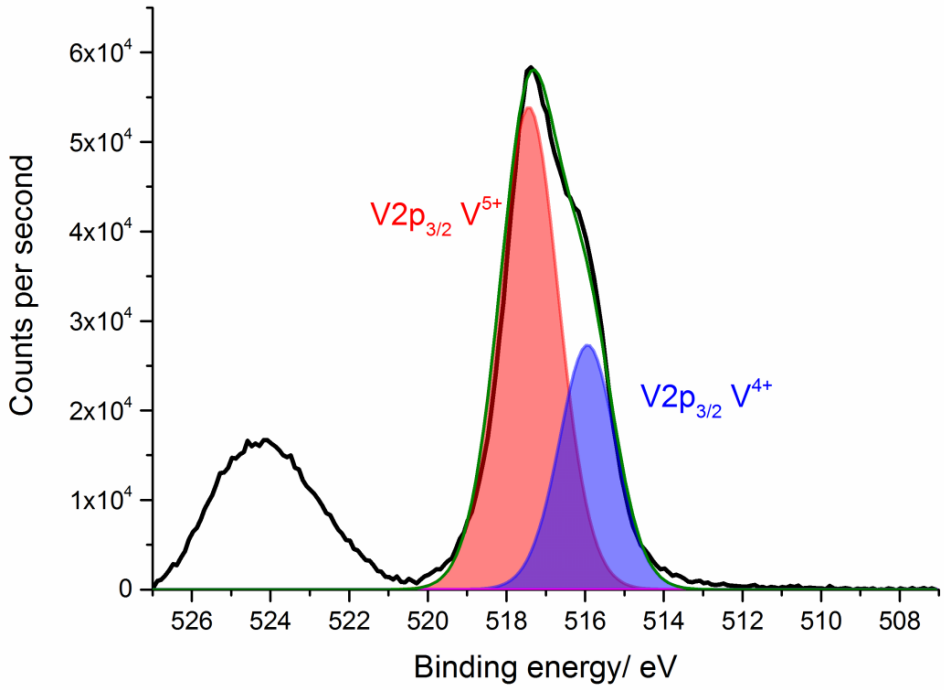

Figure 3.05: XPS spectra for vanadium binding energy of vanadium of multi-layered film, sample VST-1.

3.3.4 Thermochromic and optical properties of films

Variable temperature UV/Vis/NIR spectra were obtained for the deposited films, Figure 3.06, which showed that all samples synthesised had a temperature induced phase change and were thermochromic in near IR wavelengths. It can be seen that the sample that shows the largest change is VST-3, Figure 3.06 (d). T_c for all samples shown is ~68 °C.

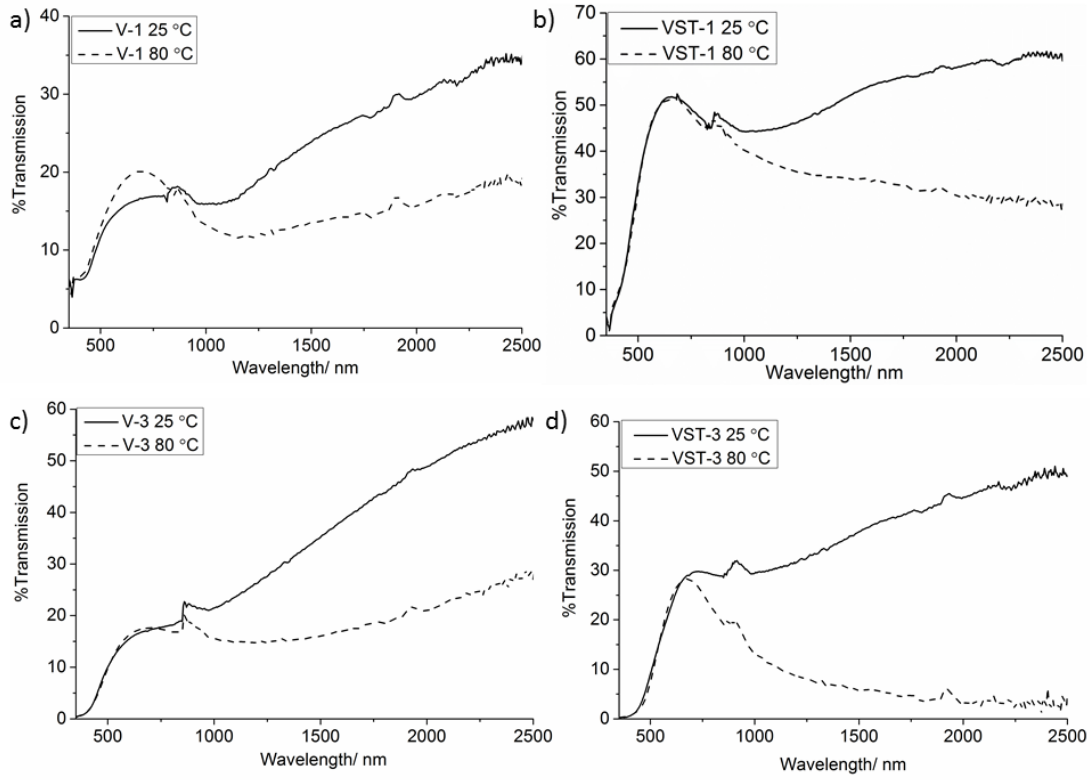

Figure 3.06: Variable temperature UV/Vis transmission spectra showing thermochromic behaviour for **a)** sample V-1, single layer of VO_2 deposited for 1 minute, **b)** sample VST-1, multi-layered $VO_2/SiO_2/TiO_2$ each layer has been deposited for 1 minute, **c)** sample V-3, single layer of VO_2 deposited for 3 minutes and **d)** sample VST-3, multi-layered $VO_2/SiO_2/TiO_2$ the VO_2 and SiO_2 layers have been deposited for 3 minutes the TiO_2 has been deposited for 1 minute. All samples are shown at 25 °C (solid line) and 80 °C (dashed line). T_c for all samples = ~68 °C.

As with the samples in Chapter 2, in order to quantitatively measure the samples against each other, the UV/Vis spectra must be weighted for both solar modulation and for visible light transmission. The equations 2.4, 2.5, 2.6 and 2.7 were used to produce the values in Table 3.3. As shown, the film that shows the greatest solar modulation is VST-3. Whilst it isn't surprising that the thicker VO_2 depositions, V-3

and VST-3 show the greatest solar modulation, what is interesting is that there is almost a 2-fold difference in response, with VST-3 being far superior in response. It also shows close to the theoretical maximum response for a VO_2 system.[182] The thinner of the multi-layered systems, VST-1, also shows a significant increase in the solar modulation when compared to the single film analogue V-1. In this case, a more than 2-fold increase in response is observed. As both multi-layered samples showed an increase in the solar modulation response, this suggests that the multi-layer systems have a mechanism that increases the response.

The visible light properties of the films were also altered by the inclusion of the multi-layers. Both of the multi-layered systems showed an increase in the visible light transmission (T_{lum}) when compared with the single layer analogues. The largest difference was observed between sample V-1 and VST-1, where the multi-layered system showed ~30% increase in the visible light transmission. This is a large improvement and shows that the haziness associated with VO_2 thin films can be reduced by the inclusion of materials with a different refractive index. A smaller improvement was observed with the thicker samples, where a 4% improvement was observed between samples V-3 and VST-3. Similar improvements have been observed with multi-layered VO_2/SiO_2[146] and VO_2/TiO_2[137, 145, 191] systems synthesised by sputtering and sol-gel techniques.

The UV/Vis spectra suggest that the incorporation of VO_2 into multi-layered systems by the use of APCVD can be achieved, without any detrimental effects to the thermochromic response. The multi-layered films have improved visible light transmission and a larger solar modulation when compared to the single film analogues.

Sample	Weighted solar modulation (%)	T_{lum}^{cold}	T_{lum}^{hot}	ΔT_{lum}
V-1	3.14	14.15	16.55	-2.4
VST-1	7.63	44.24	44.19	0.05
V-3	8.09	13.60	14.08	-0.48
VST-3	15.29	17.81	18.23	-0.42

Table 3.3: Weighted solar and visible light (T_{lum}) values for all samples

3.3.5 Photocatalytic properties of the films

To determine the photocatalytic properties of the deposited films, stearic acid destruction measurements were obtained. Stearic acid is a model organic pollutant that is stable to UV degradation in the absence of a photocatalyst. The mineralisation of the acid results in the decomposition as shown in Equation 3.4. The mineralisation of stearic acid has zero order kinetics, and the degradation of the acid can be followed by FTIR measurements, as the C-H bands (between 2700-3000 cm^{-1}) will steadily decrease in intensity.

$$CH_3(CH_2)_{16}CO_2H + 26O_2 \xrightarrow{TiO_2(h\nu \geq E_{bg})} 18CO_2 + 18H_2O \qquad (3.4)$$

The single layer VO_2 samples, V-1 and V-3, showed no photo-induced destruction of the stearic acid. For comparison purposes, a pure phase anatase film (synthesised by APCVD) and an industry TiO_2 film used for self-cleaning applications (Pilkington Activ™) were also tested against the multi-layered samples, VST-1 and VST-3.

Figure 3.07 (a) and (b) show the integrated stearic acid areas and the rates of stearic acid destruction for these samples. It can be clearly seen that sample VST-1 is not active for the destruction of stearic acid, this is not surprising as this sample showed only rutile diffraction peaks in the XRD data, Figure 3.01. The rutile phase of TiO_2 has poor photocatalytic rates due to fast recombination of the photo-induced electron/hole pairs.[209] In contrast, sample VST-3 is shown to have a higher rate of destruction of stearic acid than Activ™ glass from Pilkington. As this is the glass used for self-cleaning applications, it can be determined that the multi-layered samples do show multi-functional properties. The rate of stearic acid destruction is lower for sample VST-3 than for the pure anatase thin film, this is due to two reasons, the first is that sample VST-3 is a mixed phase of anatase and rutile and so would likely suffer from higher rates of recombination rates, the second reason is due to thickness. The anatase layer deposited was ~500 nm in thickness, which is close to the ideal thickness for photocatalytic properties for anatase thin films.[210] This explains the apparent poor rate of the VST-3 sample when compared with the anatase sample.

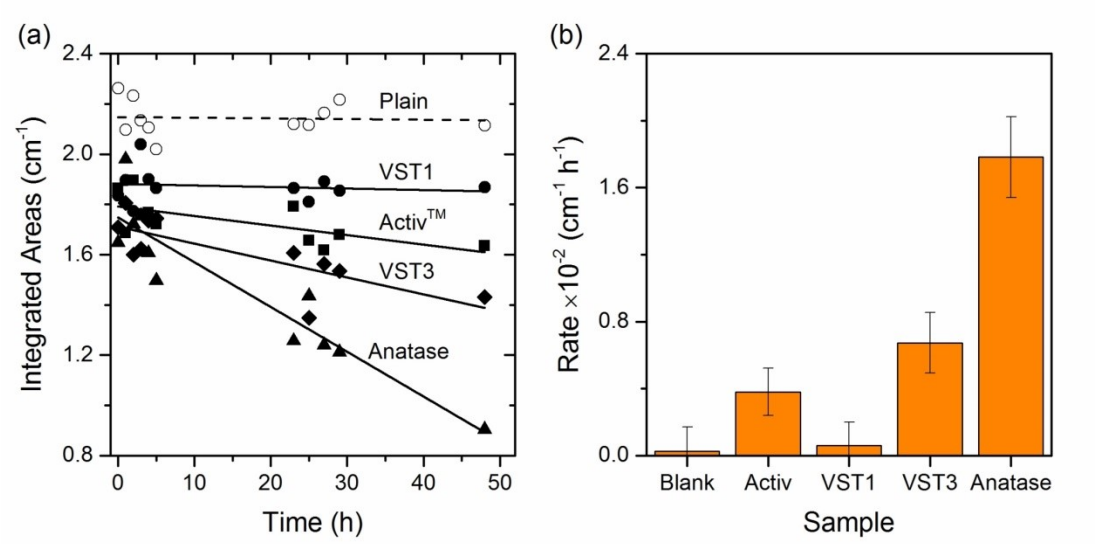

Figure 3.07: Photocatalytic destruction of stearic acid by samples exposed to UV light (λ = 365 nm) **a)** Integrated areas for stearic acid destruction showing samples VST-1, VST-3, Pilkington Activ^{TM} (industry standard TiO_2 thin film for self-cleaning applications) and a pure anatase film and **b)** Photocatalytic rates for the stearic acid destruction. The single vanadium films, V-1 and V-3, showed no photo-induced destruction of the stearic acid.

3.3.6 Modelling of multi-layered $VO_2/SiO_2/TiO_2$ thin films

Details on the model and parameters used can be found in Appendix 1. Modelling of sample VST-1 was performed to elucidate if there were any design rules that could be applied to multi-layered $VO_2/SiO_2/TiO_2$ films grown by APCVD. This was to allow the optimisation of the films and determine the effect of the SiO_2 layer on the improvement of the visible light properties. For these purposes, the SiO_2 layer was considered to have bulk characteristics and the refractive properties associated with a continuous layer of SiO_2 of ~1.4 µm.

As shown in Figure 3.08, when the multi-layered film was simulated with bulk like properties for the VO_2, SiO_2 and TiO_2, the resulting T_{lum} and ΔT_{sol} were both different from the actual results recorded for sample VST-1. For these models, the refractive index for TiO_2, SiO_2 and VO_2 were taken from Devore,[211] Palik[212] and Mlyuka[160] respectively. Figure 3.08 a) shows the calculated properties for a film with coherent visible light properties between all the layers. Sample VST-1, however, would show incoherence as the thickness of the SiO_2 layer is larger than the coherence length of broadband sunlight- it is not surprising that Figure 3.08 a) does not match the

UV/Vis spectra obtained for sample VST-1. It is also important to note that coherence within the SiO_2 would lead to resonant peaks in the transmittance spectra which were not observed in our UV-VIS measurements.

Therefore, an incoherence factor between the layers was modelled. This is shown in Figure 3.08 b). As shown, this is actually further from the observed results for sample VST-1 than the previous model, suggesting that the film has another mechanism which is improving the visible light characteristics.

The two first models assumed that the three layers were all uniform in thickness, to determine whether a varying film thickness would account for the enhanced visible light transmission of sample VST-1, a further model was calculated. Figure 3.08 c) shows the result of these calculations, as shown, the enhanced visible light properties cannot be accounted for by a difference in the film thicknesses of the different components in the multi-layered system.

These results suggested that the porous nature of the films were contributing a significant contribution to the improvement in the visible light transmission. Closer inspection of the sample V-1 compared to VST-1 showed the multi-layered film, VST-1, had a significant reduction in haze than the single film VO_2 analogue, V-1. It was, however, very difficult to give a direct contribution of the porous SiO_2 film. This was due to the fact that the structure was disordered and the pore sizes varied in size, this meant it was very difficult to simulate the interactions of light as it passed between the air in the pores and the SiO_2 layer. This is important as the change in refractive properties affects the scattering of light as it passes through the structure, the greater the scattering of visible wavelengths, with such a porous structure the refractive index of the SiO_2 will be lower.[213, 214] This would result in higher visible light transmission through the film.

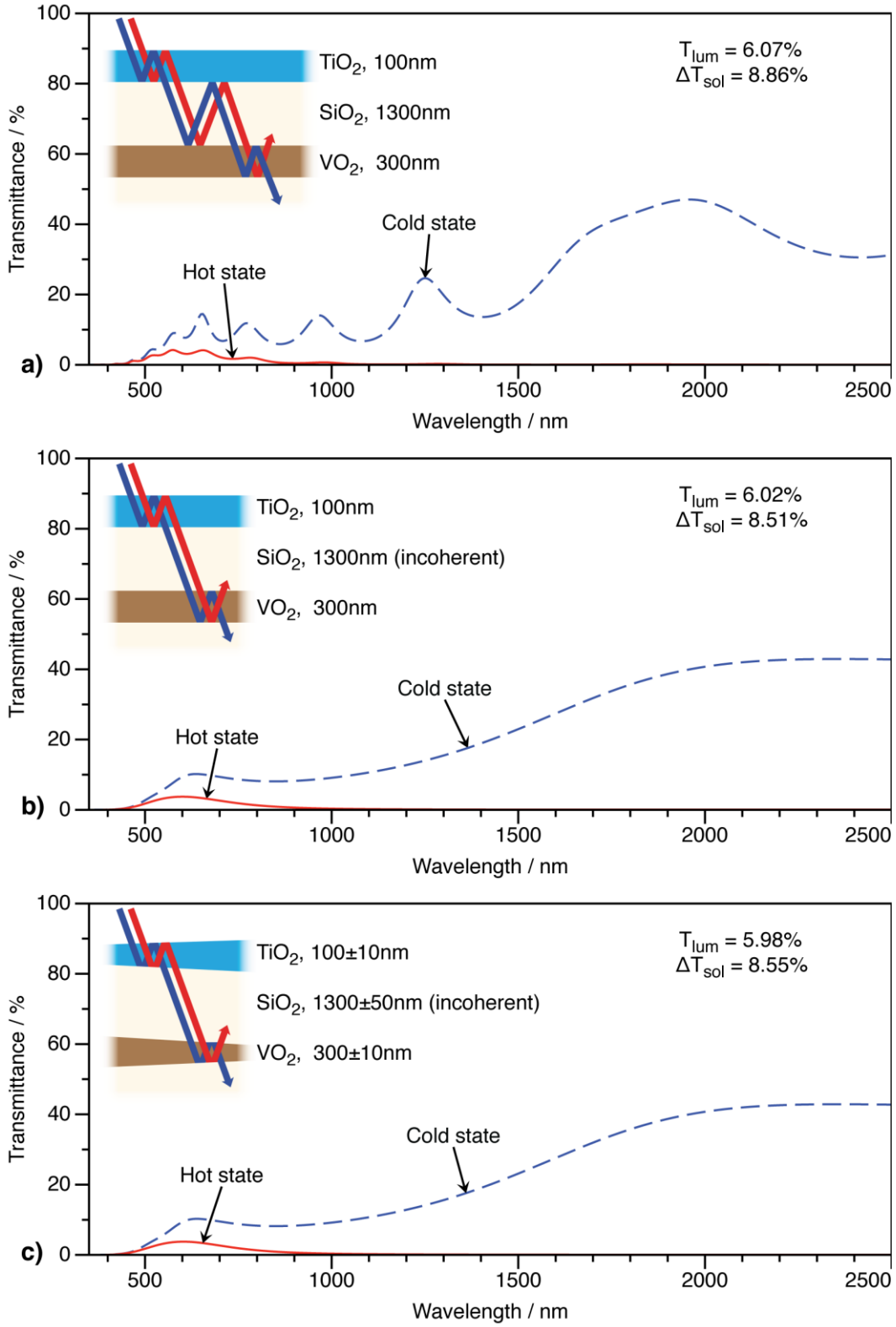

Figure 3.08: Calculated properties of multi-layered film with $VO_2/SiO_2/TiO_2$ **a)** Coherent conditions, uniform thickness of films, **b)** incoherent conditions, uniform thickness of films and **c)** incoherent film with non-uniform thickness values.

In order to elucidate the effect of the SiO_2 layer on the visible light response of the multi-layered films, a range of films with differing thicknesses of VO_2 were simulated. For these simulations, the SiO_2 layer was considered to be ~1.4 μm with a TiO_2 layer of 100 nm. All the layers were considered to display bulk-like properties. The simulation that obtained results that were comparable to those displayed for sample VST-1 had a layer of VO_2 that was only ~50 nm thick. These results are shown in Figure 3.09 a). The data was also used to simulate a UV/Vis spectra for the switching behaviour of such a film, Figure 3.09 b), as shown this is in good agreement with the spectra obtained for sample VST-1 (Figure 3.06 b)).

As shown in the graph, the T_{lum} and ΔT_{sol} are now in much better agreement with the values obtained for sample VST-1. The VO_2 layer from the simulation is an order of magnitude (~ x10) thinner than the VO_2 layer observed in the SEM images for sample VST-1, which were shown to be ~300 nm in thickness. Although this appears to suggest that the VO_2 is less thermochromically active, the modelling is for an ideal system and does not take into account defects in the structure, such as the presence of other vanadium oxides. Both of the multi-layered samples show superior solar modulation to their single layer analogues, which suggests that the SiO_2/TiO_2 overlayer is protecting the VO_2 allowing for a larger switch.

As the difference between the simulation and the synthesised films is the porosity of the SiO_2 layer, it must be considered that the improvement in the visible light transmission of sample VST-1, when compared with sample V-1, is due to the enhanced scattering of light by the difference in refractive properties between the air and the SiO_2 as visible wavelengths pass through the highly porous SiO_2 layer. The other result that can be taken from this is that it is possible to produce a film with the visible light transmission equivalent to a very thin layer (<50 nm) of VO_2, but with the solar modulation (thermochromic response) of a significantly thicker film (>200 nm).

It has been previously observed for TiO_2[215, 216] and SiO_2/TiO_2[217] systems that inducing porosity on the length scale of visible wavelengths can cause a significant improvement in visible light transmission due to enhanced scattering of light. It is very likely that due to the size of the pores in the SiO_2 layer, that a similar process is occurring in sample VST-1- with the subsequent improvement in visible light transmission and reduction of haziness.

Although sample VST-3 showed an improvement in visible light transmission when compared to sample V-3, the overall improvement was significantly lower than

observed in sample VST-1. This suggests that there is also an ideal thickness to the porous SiO_2 layer, which appears to be ~1.4 µm. Beyond this thickness, the samples begin to suffer from absorption of visible wavelengths as well as increased scattering, leading to a reduced difference in the visible light transmission between the multi-layered and single film analogues.

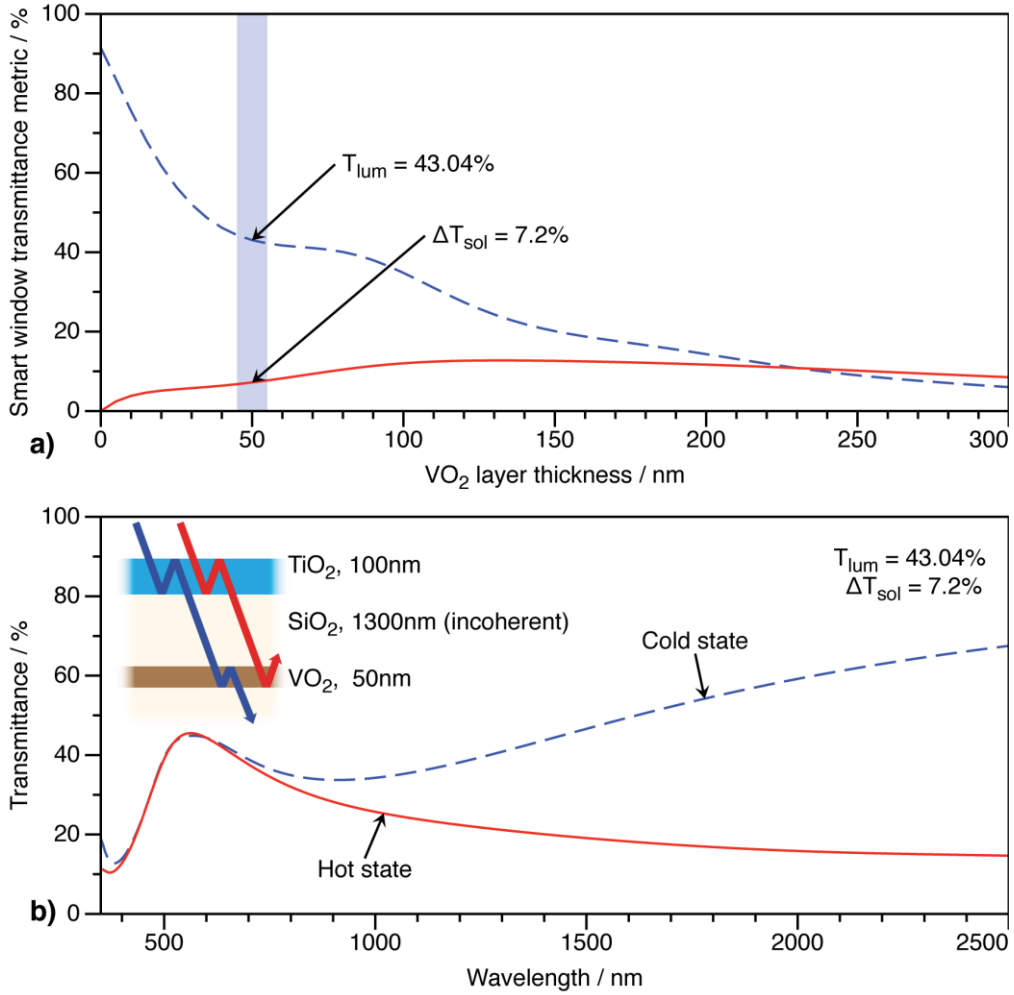

Figure 3.09: a) Calculated properties for a range of thicknesses of VO_2 thin films, showing that ~50 nm VO_2 thin film gives the same properties as those observed for sample VST-1 and **b)** Calculated properties of multi-layered film with similar visible light transmission and solar modulation as those observed in sample VST-1. The VO_2, SiO_2 and TiO_2 layers are considered to have bulk-like characteristics.

3.4 Conclusions

Multi-layered $VO_2/SiO_2/TiO_2$ thin films have been demonstrated for the first time from APCVD methods. XRD analysis proved that the multi-layered films had TiO_2 at

the surface, interestingly, the thinner of the multi-layered films showed only rutile diffraction peaks, whilst the thicker film showed a mixture of rutile and anatase diffraction peaks. This was attributed to strain from the underlying SiO_2 film favouring the formation of rutile TiO_2.

The morphology of the films was determined by SEM analysis. The single layer VO_2 films showed morphologies consistent with those previously observed, in Chapter 2, for VO_2 thin films deposited by the reaction of VCl_4 and ethyl acetate by APCVD. Surprisingly, the SiO_2 film was shown to consist of a column-like structure with large voids, presumably containing air pockets, in-between. The TiO_2 layers had a pyramidal like structure, which was consistent with previous reports of TiO_2 deposited by APCVD.

The thermochromic properties were determined by variable temperature UV/Vis spectroscopy. In all cases, the multi-layered films showed improved visible light transmission and solar modulation when compared to single layer analogues. A significant increase was observed for the thinner of the multi-layered films, with the sample showing a 30% improvement in the visible light transmission and a doubling of the solar modulation.

The multi-layered samples were also tested for photocatalytic properties. The photocatalytic destruction of stearic acid was measured, with the thicker multi-layered sample being proven to be more active than an industrial self-cleaning TiO_2 film, Pilkington Activ^{TM}. This proved that it was both possible to have a film with self-cleaning properties whilst also enhancing the visible light transmission and solar modulation by the application of a layer of SiO_2.

Finally, the multi-layered samples were simulated computationally to help elucidate the effect of the structure on the properties observed. The porosity of the SiO_2 layer was shown to be key to the improvement in visible light transmission. When compared to a simulated multi-layered film with a uniform SiO_2 layer with bulk-like properties, it was shown that the properties observed in the thinner multi-layered film was equivalent to a VO_2 film that was ~10 times thinner than the layer deposited. This proved that the scattering of visible light by the SiO_2 layer was the significant contributing factor to the improvement observed.

Although thin films of VO_2 (and other metal oxides) are important for applications such as coatings for windows, there are many other potential applications. One

such application would be the deposition of metal oxides, such as TiO_2, onto powder supports. Explored in the next chapter is a method to coat powders by a chemical vapour deposition route.

Chapter 4

Fluidised Bed Chemical Vapour Deposition of single and multi-shell TiO_2 on mica

Chapter 4: Fluidised Bed Chemical Vapour Deposition of single and multi-shell TiO_2 on mica

4.1 Introduction

Fluidised Bed Chemical Vapour Deposition (FBCVD) has been widely utilised in industrial applications for the production of corrosion and abrasion resistant coatings. The most common materials produced from FBCVD processes are titanium carbide,[65] silicon carbide[66, 218, 219] and aluminide coatings.[41, 54] Carbon nanotubes synthesis has also been demonstrated from FBCVD processes.[70] FBCVD is favoured for the production of these materials due to the high-throughput nature of the process, the ability to uniformly cover large areas of material and the fact that this process can be done 'on-line'- i.e. it can be incorporated into industrial processes with relative ease.[56]

FBCVD, however, is not a commonly used laboratory technique. This is due, in part, to the expense of designing and engineering such a system. Furthermore, the studies utilising FBCVD are primarily concerned with mechanically and chemically robust coatings and the large scale production of carbon nanotubes.[64, 70, 220, 221] This opens the possibility to design a FBCVD system that would allow for the development of functional coatings (e.g. photocatalytic or thermochromic) onto powder supports which could then be incorporated into applications where a traditional thin film would be unsuitable.

TiO_2 nanoparticles and thin films have been previously synthesised by CVD (e.g. Atmospheric Pressure,[53, 143, 222, 223] Aerosol Assisted;[42, 44, 224] and Plasma Enhanced CVD[48-50]), sol-gel[225-227] and hydrothermal synthesis.[106, 107, 228] Multi-shelled mixed anatase/rutile TiO_2 nanoparticles have also been reported from sol-gel synthesis.[229] FBCVD has been used to deposit TiO_2 single layers,[39, 55, 230] but there have been no reports of multi-layered films produced by FBCVD.

The FBCVD design described within this chapter was custom built for this research project. The original intention was to use the FBCVD reactor to deposit VO_2 onto powder substrates, these experiments were attempted, however, VO_2 was not shown to be successfully deposited. In order to determine whether the FBCVD reactor was able to deposit onto powder substrates, TiO_2 depositions were attempted. This allowed for the system to be demonstrated with a known material without the complex phase characteristics of vanadium oxides.[2]

Described within this chapter is a method for producing single and multi-shelled structures of TiO_2. TiO_2 was used as a case study due to the ability to control the phase present in the sample easily through deposition and post-annealing temperatures.[231] Multi-shelled and core-shell structures are primarily produced by 'wet' chemical routes such as sol-gel and hydrothermal synthesis.[189, 232-234] There have been no previous reports of producing such structures from CVD routes. A CVD route would allow for such structures to be synthesised by a high-throughput, industrially scalable process.

4.1.1 The Fluidised Bed Chemical Vapour Deposition reactor

The FBCVD syntheses reported here were performed on a custom built rig. The design chosen is along the lines of a stationary/bubbling FBCVD design- as discussed in the introduction.

The design shown was chosen due to its relative simplicity- there are no moving parts within the reactor, which reduces the possibility of breakages during operation. The fluidisation of the powder substrate was achieved by a flow of N_2 gas only. A pictorial representation of the fluidisation process is shown in Figure 4.01. Stainless steel gauzes (mesh size: 0.1 mm) are placed at the two ends of the reactor in order to prevent excess substrate escaping the reaction chamber during deposition. With this fixed bed reactor design only Geldart groups A and B substrates could be fluidised, Geldart fluidisation groups are discussed in Chapter 1 (section 1.5.5.2). The substrates that met these criteria were synthetic mica and the photocatalyst P25, with the synthetic mica showing superior fluidisation potential due to the P25 being hydroscopic. Silica flake was found to be too cohesive to achieve complete fluidisation with this design and would form clumps within the reactor.

For the synthesis of TiO_2 layers; $TiCl_4$ was placed in bubbler 1 and ethyl acetate was placed in bubbler 2. Bubblers 1 and 2 were heated to 75 and 40 °C respectively. This achieved a suitable vapour pressure from the precursors, as determined from the vapour pressure equation (Chapter 2, Equation 2.1). This gave mass flow rates of 0.00288 and 0.00554 mol min^{-1} for $TiCl_4$ and ethyl acetate respectively.

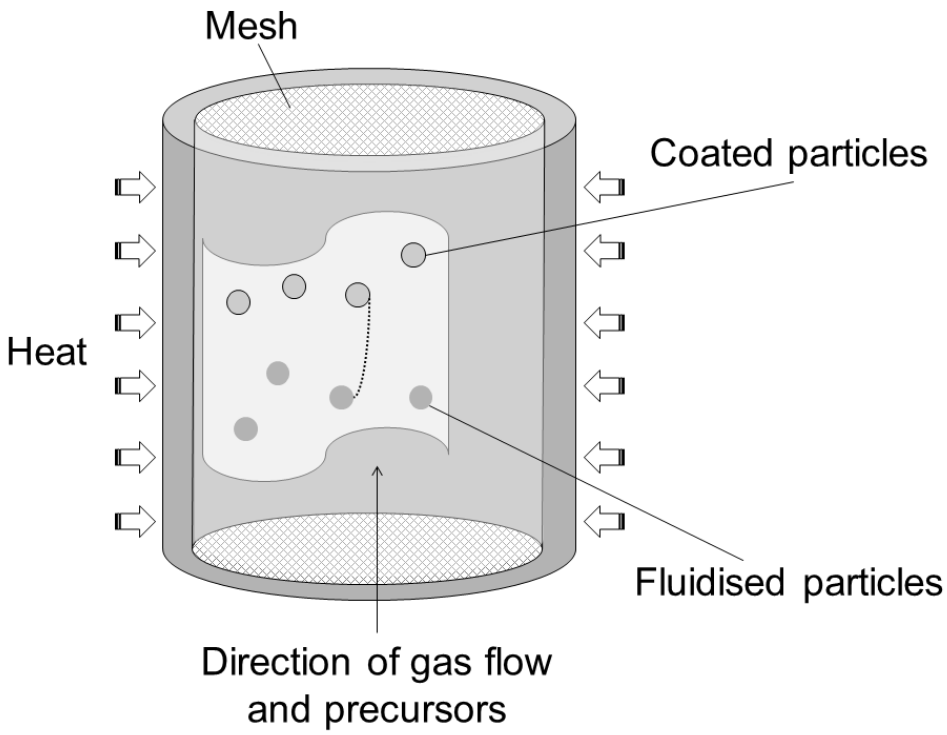

Figure 4.01: Pictorial representation of fluidisation of particles in the FBCVD reactor. Particles are suspended by the pressure exerted from a stream of N_2 gas entering the reactor from below. The N_2 gas also acts as a carrier gas for the volatile precursors used to coat the particles. Particles are heated from the sides of the reactor.

The reactor design is a hot-walled FBCVD system. Figure 4.02(a) shows a photograph and Figure 4.02(b) shows a schematic of the system. Precursors were heated in stainless steel bubblers, with brass jackets and heating bands. The temperature of the bubblers was controlled by *Thermotron* controllers with RS k-type thermocouples. The gas lines consisted of stainless steel pipes fitted with heating tapes (*Electrothermal* 400 W, 230 V) and controlled by *Thermotron* controllers with RS k-type thermocouples. The precursors were mixed in a stainless steel mixing chamber prior to entering the reactor. The reactor consisted of a vertically mounted tube furnace fitted with a *Eurotherm* controller.

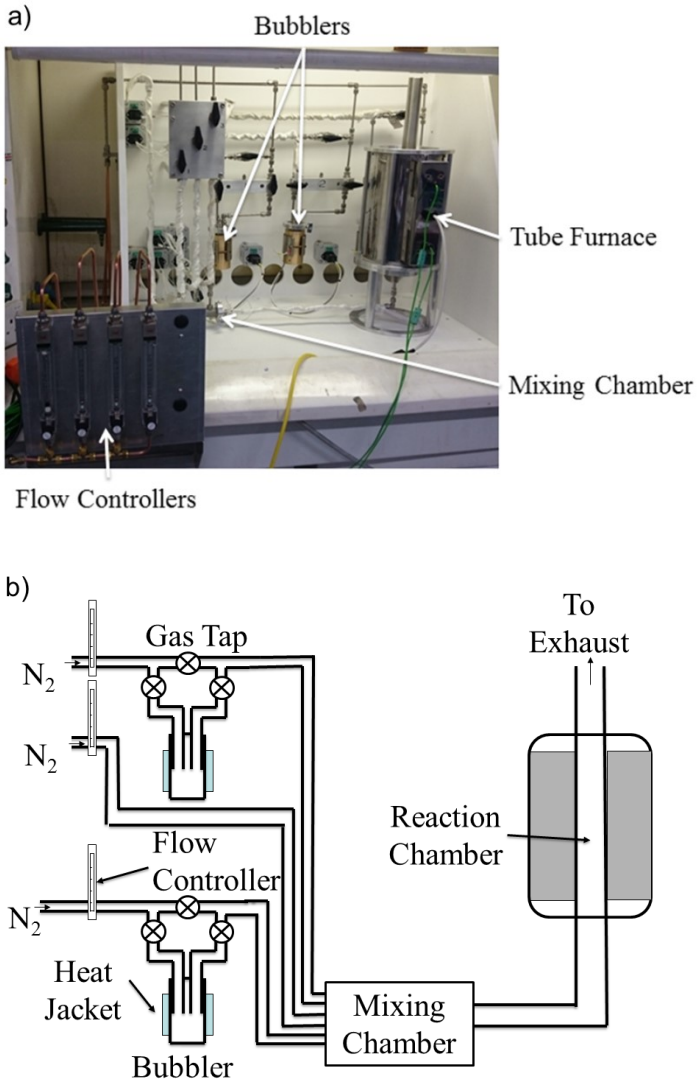

Figure 4.02: (a) Photograph showing FBCVD reactor in fumehood and **(b)** Schematic showing the FBCVD design.

4.2 Synthesis of anatase, rutile, mixed anatase/rutile single shelled and rutile@anatase multi-shelled particles

4.2.1 Aim

To determine the effectiveness of the FBCVD rig design outlined above, a case study involving the synthesis of TiO_2 coatings onto powder supports was undertaken. This was to evaluate the ability of the reactor to produce crystalline, uniform coatings and determine whether there were any significant drawbacks to the design.

4.2.2 Experimental

For the following reactions the titanium precursor source used was titanium (IV) chloride ($TiCl_4$, 99.9%) and the oxygen precursor source used was ethyl acetate anhydrous ($C_4H_8O_2$, 99.8%) both precursors were purchased from *Sigma Aldrich UK*. The substrate used was mica (*Symic C001*, synthetic fluorphlogopite:TiO_2 80:20), particle size range 10-40 µm, purchased from *Eckert*. All precursors and substrates were used as purchased without additional chemical treatment.

For the synthesis of TiO_2 layers, $TiCl_4$ was placed in bubbler 1 and ethyl acetate was placed in bubbler 2. Bubbler 1 and 2 was heated to 75 and 40 °C respectively. This achieved a suitable vapour pressure from the precursors. Approx. 3g of mica substrate was loaded into the reactor in a typical deposition. The reactor was set to 500 °C (ramp rate 10 °C min^{-1}), when this temperature was reached the reactor was left for a further 30 minutes to ensure uniform heating of the substrate. All lines were heated to 150 °C, ensuring the precursors did not condense inside. The mixing chamber was heated to 150 °C. When depositing, the plain flow N_2 would be increased to 10 L min^{-1} this achieved both the fluidisation of the powder substrate and also ensured that the precursors were sufficiently mixed. The flow controllers for bubbler 1 and 2 were set to 0.6 L min^{-1}, with nitrogen switched to pass through the precursor. This gave a mass flow rate of 1:2.4 $TiCl_4$: ethyl acetate, as a slight excess of the oxygen precursor was found to give reproducible results. The precursors would then be simultaneously switched into the mixing chamber by a 3-way valve. Depositions would typically last 30 minutes after which the 3-way valve would be switched back and the nitrogen flow to the precursor would be closed. The reactor was left to cool under a flow of nitrogen, with samples only being removed when the temperature was below 200 °C.

To ensure crystallinity samples were post-annealed, in air, between 500 and 1000 °C. This was achieved using a furnace (ramp rate 20 °C min^{-1}) fitted with a *Eurotherm* controller.

4.2.3 Sample descriptions

Two initial coatings of TiO_2 on mica substrates were synthesised, these were synthesised at 500 and 550 °C by a single 30 minute deposition. These samples were characterised by XRD to determine the crystallinity of the TiO_2 layer.

A further four TiO_2 coatings were synthesised on the FBCVD these were pure anatase, pure rutile, a mixed phase anatase/rutile and a multi-shelled anatase on rutile. The anatase, rutile and mixed samples were all achieved by a single 30 minute deposition followed by a post-annealing treatment. The multi-shelled structures were achieved by an initial 30 minute deposition followed by a post-treatment of the sample, before the sample was transferred back into the FBCVD and an additional layer was applied. Pictorial representations of the particles described can be found in Figure 4.03. This over-layer was also post-annealed to ensure crystallinity. The sample descriptions and conditions are summarised in Table 4.1.

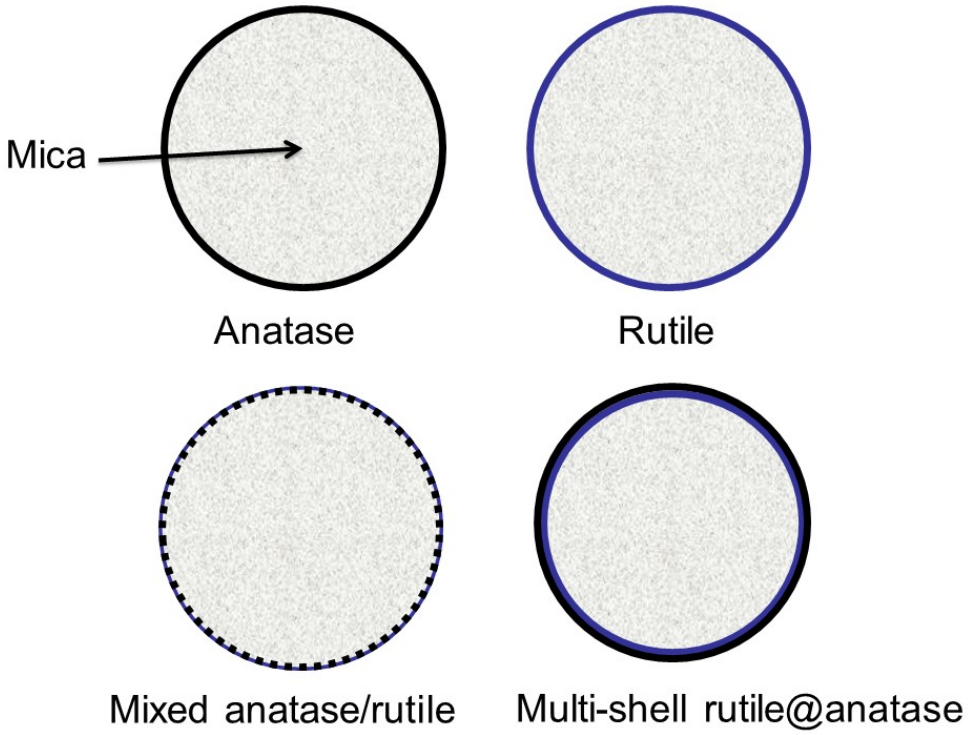

Figure 4.03: Pictorial representations of anatase, rutile and mixed single shelled particles and multi-shell rutile@anatase particles.

Name	Description	Deposition Conditions		Annealing Conditions	
		Time (mins)	Temp (°C)	Time (hrs)	Temp (°C)
TiO_2 on mica at 500 °C	Initial TiO_2 deposition on mica substrate	30	500	N/A	N/A
TiO_2 on mica at 550 °C	Initial TiO_2 deposition on mica substrate	30	550	N/A	N/A
Anatase	Pure anatase single shell on mica	30	500	10	500
Mixed Anatase/Rutile	Mixed phase anatase and rutile single shell on mica	30	500	10	750
Rutile	Pure rutile single shell on mica	30	500	10	1000
Multi-shell Rutile@Anatase	Double shell anatase on rutile on mica	30 30	500 500	10 10	1000 500

Table 4.1: Synthesis conditions of single and multi-shelled TiO_2 layers on mica supports

4.2.4 Film Characterisation

X-ray diffraction (XRD) studies were carried out using a *Stoe* (Mo) *StaniP* diffractometer. The instrument operates with a Mo X-ray source (Mo tube 50 kV 30 mA), monochromated (Pre-sample Ge (111) monochromator selects Kα1 only) and a *Dectris Mython* 1k silicon strip detector covering 18° (2θ). Samples were run in transmission mode, with the sample being rotated in the X-ray beam. The diffraction patterns obtained were compared with database standards from the Inorganic Crystal Structure Database (ICSD) based in Karlsruhe, Germany. Raman spectroscopy was carried out using a *Renishaw 1000* spectrometer equipped with a 633 nm laser. The Raman system was calibrated using a silicon reference. UV/vis spectroscopy was performed using a *Perkin Elmer Lambda 950* UV/Vis/NIR Spectrophotometer. The absorption spectra were recorded *via* diffuse reflectance, with the samples being deposited onto microscope slides. A *Labsphere* reflectance standard was used as reference in the UV/vis measurements. Transmission electron microscopy (TEM) images were obtained using a JEM-100CX II TEM with

a W source operating at an acceleration voltage of 100 kV. Micrographs were recorded on a *Gatan Erlangshen* ES500W. The powders were sonicated and suspended in methanol and drop-cast onto a 400 Cu mesh lacy carbon film grid (*Agar Scientific Ltd*.) for TEM analysis. Low-temperature nitrogen adsorption-desorption isotherms were measured at 77 K using a *Quantachrome Autosorb-IQ2* machine. Specific surface area was measured using the desorption isotherm within relative pressures of 0.01 and 0.3, in accordance with the Brunauer-Emmett-Teller (BET) method. Scherrer analysis was performed using the Scherrer equation,[235, 236] 4.1. Peak broadening due to the X-ray diffractometer was determined by comparison to a Y_2O_3 standard.

$$B(2\theta) = \frac{K\lambda}{Lcos\theta} \quad (4.1)$$

Where:

B(2θ) is the mean size of the crystallites

K is the shape factor (this is dimensionless) and can vary between 0.62 to 2.08

λ is the X-ray wavelength

L is the peak broadening at FWHM after the peak broadening due to the X-ray diffractometer is removed

θ is the Bragg angle

4.2.5 Photocatalytic testing

For the evaluation of their photocatalytic activity, the samples were dip-coated onto borosilicate glass slides from 1 wt.% aqueous solutions. The immersion time was 10 s and withdrawal of 30 cm min^{-1} during the dip coating process. The samples were then dried overnight at 100°C. A layer of stearic acid was drop-cast onto the samples from a chloroform solution (0.05 M). The degradation of the acid was monitored by infrared spectroscopy (2700 – 3000 cm^{-1}) using a *Perkin Elmer RX-I* Fourier transform infrared spectrometer. The samples were irradiated in a home-built light box equipped with six blacklight blue fluorescent tubes (UVA 6×18W) and an extractor fan. The irradiance (4 ± 0.2 mW cm^{-2}) at sample position was measured using a *UVX* radiometer (*UVP*). The area of the sample under illumination was 3.14 cm^2.

4.3 Results and discussion

Using a custom rig, designed and built for the project, thin films of TiO_2 were deposited on mica substrates. The reactor was a hot-walled design, with a tube furnace being both the reaction chamber and the heat source (shown in Figure 4.02). The TiO_2 films were synthesised by the reaction between $TiCl_4$ and ethyl acetate, Equation 4.2. As previously discussed, in chapter 2, the exact mechanism by which ethyl acetate decomposes in the reaction is unknown, but the mechanism described in Equation 2.3 is again the most likely route.

$$TiCl_4 + \text{ethyl acetate} \rightarrow TiO_2 + \text{byproducts} \quad (4.2)$$

Precursors were placed in bubblers, which allowed the control of partial pressures through temperature and flow rates. In a typical reaction, the $TiCl_4$ bubbler was heated to 75 °C and the ethyl acetate to 40 °C. Both bubblers had a N_2 flow rate of 0.6 L min^{-1} during depositions.

4.3.1 Initial depositions of TiO_2

To determine whether the FBCVD reactor was suitable for the deposition of thin films onto powder substrates, TiO_2 on mica depositions were performed. Two temperatures were chosen for the initial depositions, 500 and 550 °C. Depositions times were 30 minutes in length.

The as deposited TiO_2 films were characterised by XRD, Figure 4.04. Before depositing, the mica substrate had no reflections that could be assigned to anatase TiO_2. Post deposition, there are clear peaks present in the XRD data, with the peak at 11.58 2θ/ ° (anatase 101) being the most intense. The crystallinity, however, of both samples is poor. This suggests that there is poor thermal conductivity between the powder and the side of the FBCVD reactor. It was decided to post-anneal all subsequent samples to ensure crystallinity.

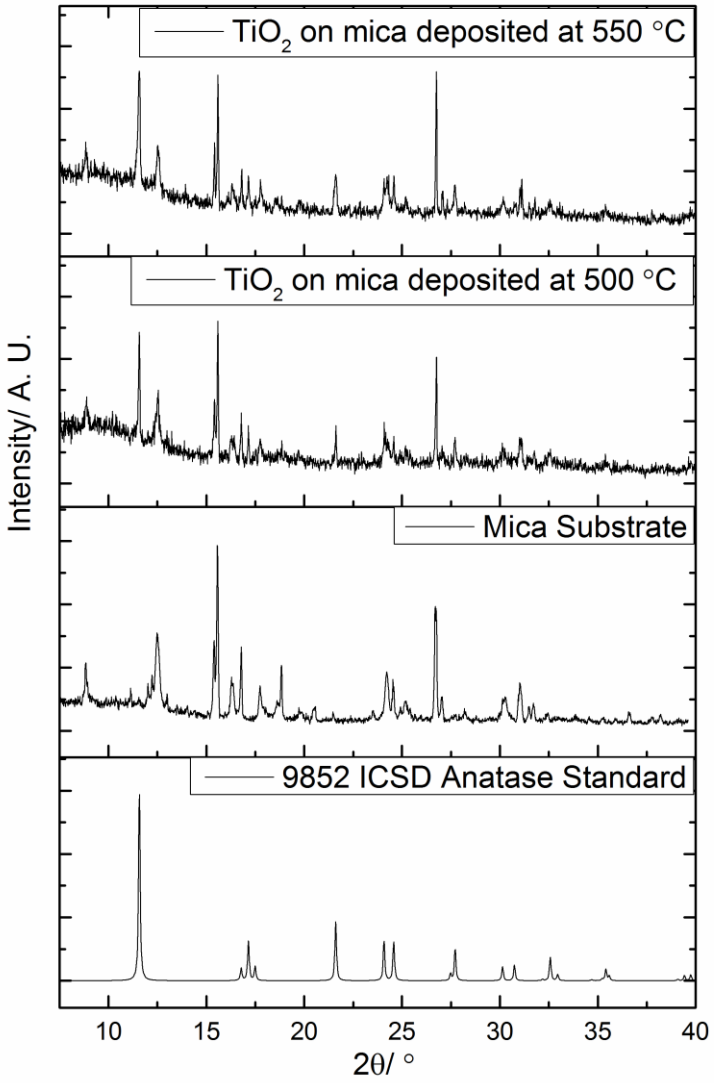

Figure 4.04: X-ray diffraction patterns for TiO_2 on mica depositions at 500 and 550 °C with the mica substrate and an anatase reference, ICSD 9852. The additional peaks in the patterns for the TiO_2 on mica are attributed to the mica substrate. λ = 0.7093 Å.

4.3.2 Deposition of anatase, rutile, mixed anatase/rutile single shelled and multi-shelled rutile@anatase films on mica

4.3.2.1 Optical properties

The as deposited films, prior to any post-annealing treatment, had a greyish colour which was attributed to the underlying mica substrate which was a silver/grey. When the powders had been post-annealed, the anatase sample maintained this original colour- suggesting that the TiO_2 film was transparent. The mixed anatase/rutile, pure rutile and rutile@anatase samples all had a golden/cream colour post-annealing. This colour was attributed to the rutile phase. Diffuse UV/Vis spectra

were obtained for all samples to determine the absorption characteristics and to calculate Tauc plots to estimate band-gap energies.

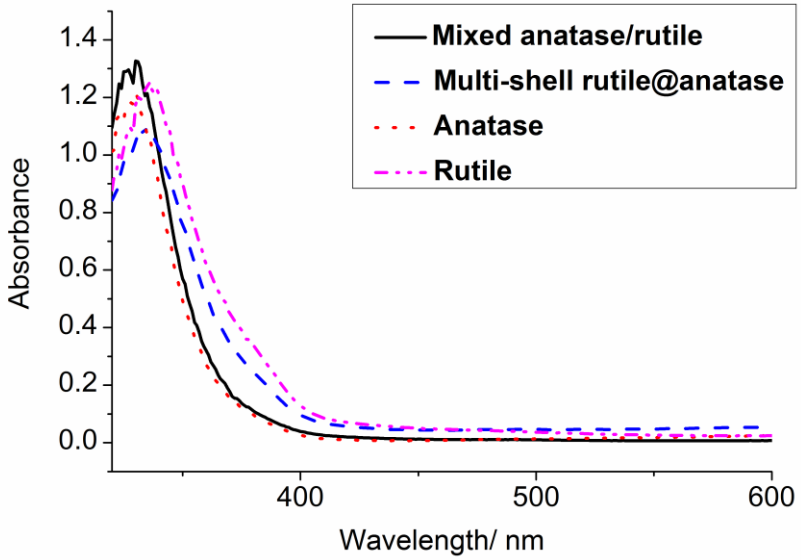

Figure 4.05: Diffuse UV/Vis absorbance spectra data for samples anatase, rutile, mixed anatase/rutile and multi-shell rutile@anatase.

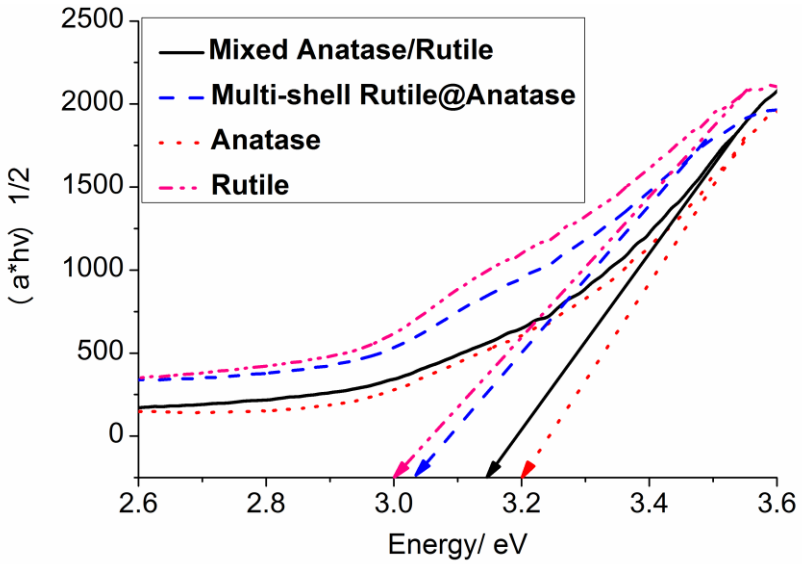

Figure 4.06: Tauc plots for samples anatase, rutile, mixed anatase/rutile and multi-shell rutile@anatase showing calculated band-gap energies.

The UV/Vis diffuse reflectance absorbance data, shown in Figure 4.05, showed a red-shift of the rutile sample, this is in agreement with literature values where rutile is quoted as having a band-gap of 3.0 eV compared to 3.2 eV for anatase.[237] The diffuse reflectance data also suggested that the mixed anatase/rutile had a large

anatase component, whereas the multi-shell rutile@anatase showed a larger rutile component. The absorbance measurements were used to calculate Tauc plots for the samples.[238, 239] A Tauc plot allows for the estimation of band-gap energies for undoped semi-conductors from absorbance data. When electrons are promoted from the valence into the conduction band (in a semi-conductor) there is a large increase in absorption in the associated electromagnetic wavelength region. If the energy of the incoming photons (eV) is plotted against the absorption of the material multiplied by the energy of the incoming photons (a*hv) a linear region on the curve denotes the on-set of the band-gap. The ½ on the y axis denotes that for TiO_2 this process is direct and allowed.

Figure 4.06 shows the Tauc plots for all samples, both the pure anatase and rutile samples values were in good agreement with those reported in the literature of 3.2 and 3.0 eV respectively.[240, 241] The mixed anatase/rutile showed a value of 3.18 eV and the multi-shell rutile@anatase had a value of 3.05 eV.

4.3.2.2 Phase identification

X-ray diffraction measurements were obtained to determine the phase purity of the samples synthesised, Figure 4.07. The anatase and rutile samples were found to be in good agreement with crystallographic standards obtained from the ICSD database. Surprisingly, both the multi-shell rutile@anatase and mixed anatase/rutile samples showed a similar proportion of the anatase and rutile phases when the intensity ratios of the peaks in the patterns were compared. This was not observed in the UV/Vis diffuse spectra, where the mixed anatase/rutile showed a greater anatase and the multi-shell rutile@anatase showed a larger rutile component.

Raman spectra were also obtained to elucidate the phases present at the surface of the samples, Figure 4.08. The anatase and rutile samples showed band structures in agreement with literature values.[242] The mixed anatase/rutile showed a band structure associated with a mixture of the two phases at the surface, with the 150 cm^{-1} (B_{1g}) rutile band being likely masked by the stronger 144 cm^{-1} (E_g) anatase band. The multi-shell rutile@anatase showed a band structure due to the anatase phase only. This suggests that the surface of the multi-shell sample is anatase with a large rutile core when the XRD and UV/Vis data are taken into account. This is the expected result from the deposition of a rutile layer followed by an anatase over-layer and suggests that it is possible to achieve multi-shelled structures of different

phases of TiO_2. This is interesting as often rutile TiO_2 will act as a "seed" for crystallisation and promote the rutile phase at lower temperatures.[243] The poor crystallinity of the TiO_2 films from the FBCVD reactor could explain why this is not seen, as an amorphous TiO_2 layer can buffer the seeding effect.[244, 245]

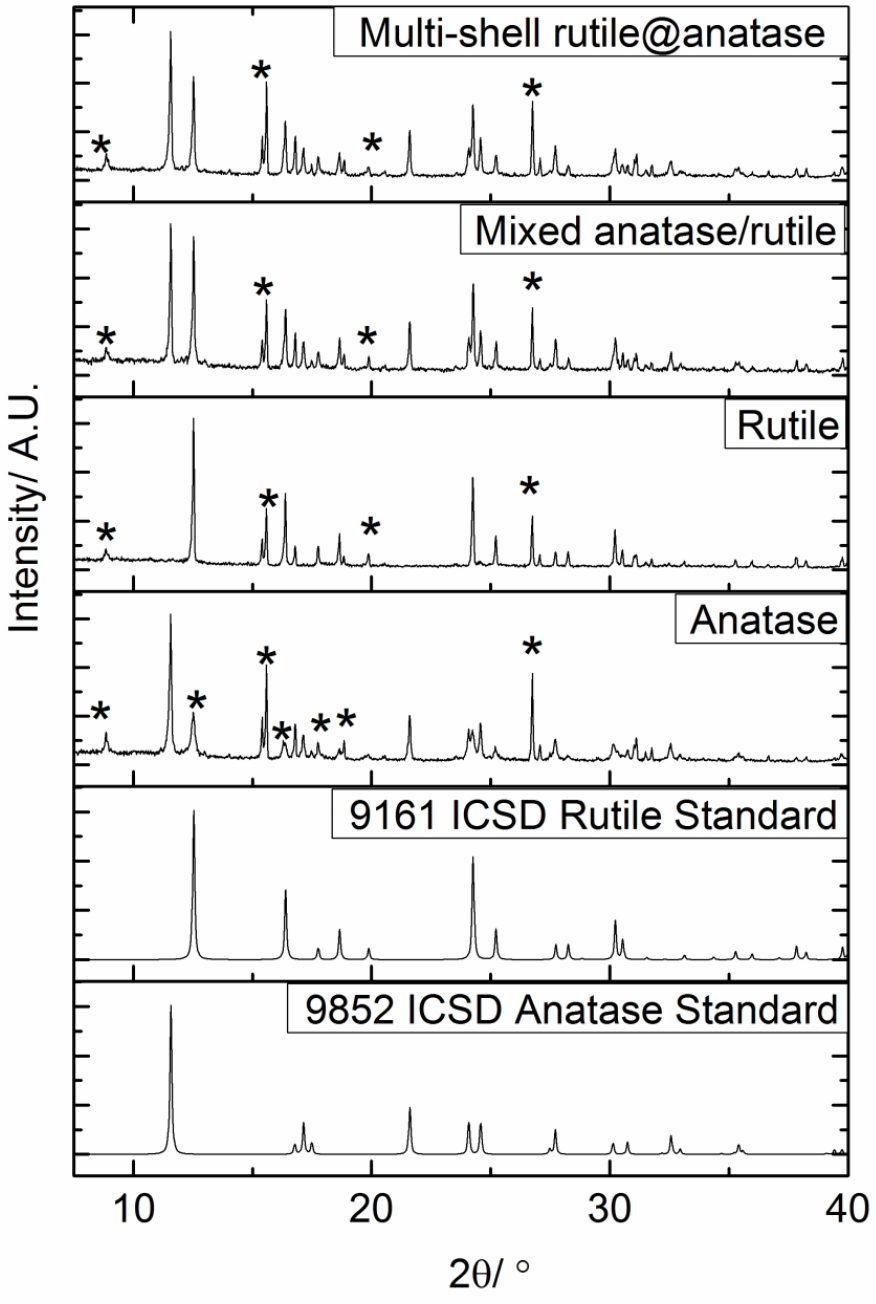

Figure 4.07: XRD patterns for samples anatase, rutile, mixed anatase/rutile, multi-shell rutile@anatase shown with ICSD standards for anatase and rutile TiO_2. Additional peaks are due to the mica substrate and are denoted by (*). λ = 0.7093 Å.

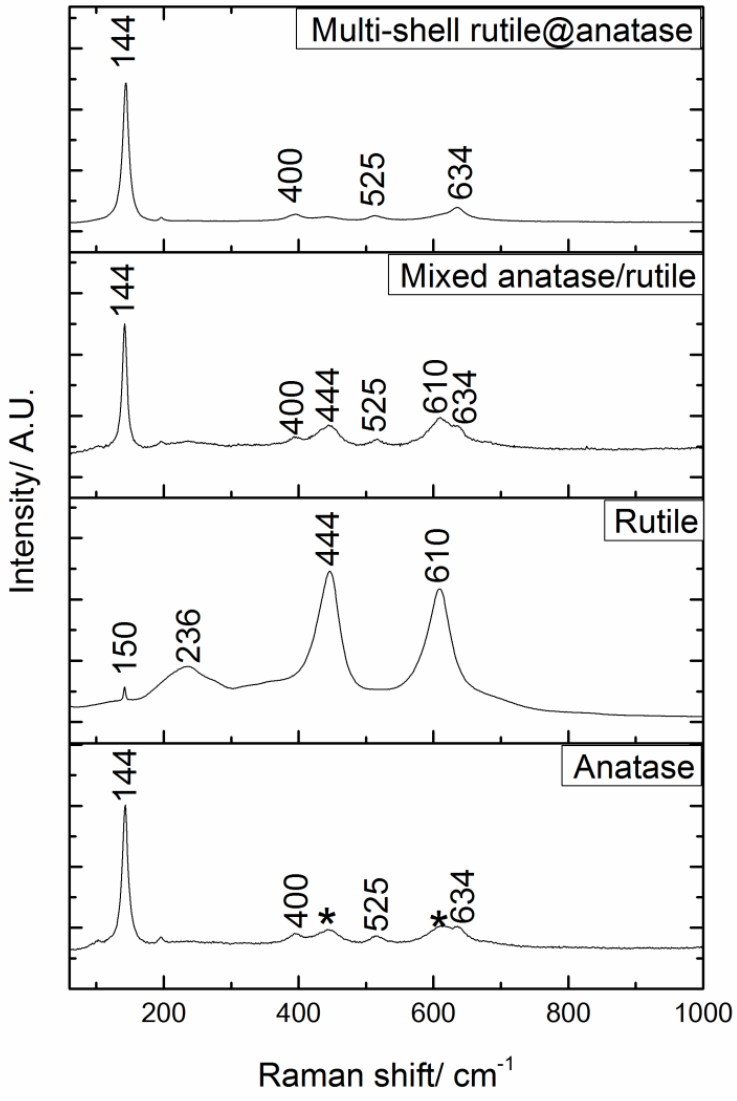

Figure 4.08: Raman spectra for samples anatase, rutile, mixed anatase/rutile and multi-shell rutile@anatase. All TiO_2 bands are numbered with mica bands being denoted by (*). Laser wavelength = 633 nm.

4.3.2.3 Morphology and film growth rates

To determine the morphology of the particles present in the samples, Transmission Electron Microscopy (TEM) images were taken, Figure 4.09. The anatase and multi-shell rutile@anatase both show a similar rounded particle shape with the anatase sample showing a larger range in particle sizes than the multi-shell rutile@anatase sample. The rutile sample showed a more hexagonal type structure to the particle shape with the particles being on average smaller than the anatase analogues. The

mixed anatase/rutile sample was in between the anatase and rutile structures displaying some hexagonal and more rounded particle shapes. Finally, only on the multi-shell rutile@anatase could evidence for multiple shells be observed. There were no obvious defects present in the multi-shell rutile@anatase particles, suggesting that there is uniform coverage of the TiO_2 layers.

To determine the growth rate of the TiO_2 layers by FBCVD, the multi-shelled TEM images were used. This was due to the clear contrast difference between the outer (anatase) shell and the inner (rutile) shell. As all depositions were 30 minutes in length, the average growth rates for all samples should be similar. The outer shell present in Figure 4.09(d) shows a thickness of approx. 50 nm. This suggests that the average growth rate for these samples is 1.7 nm per minute. Whilst this appears to be a low number, especially when compared to traditional CVD growth rates of 100s of nm per minute, the surface area of the substrate must be taken into consideration. In a traditional horizontal flat-bed CVD reactor, the substrate will have a surface area of a few m^2. The mica substrate had a surface area in the order of 10 m^3, with this being an order of magnitude difference the reduced growth rates on these powder samples is to be expected.

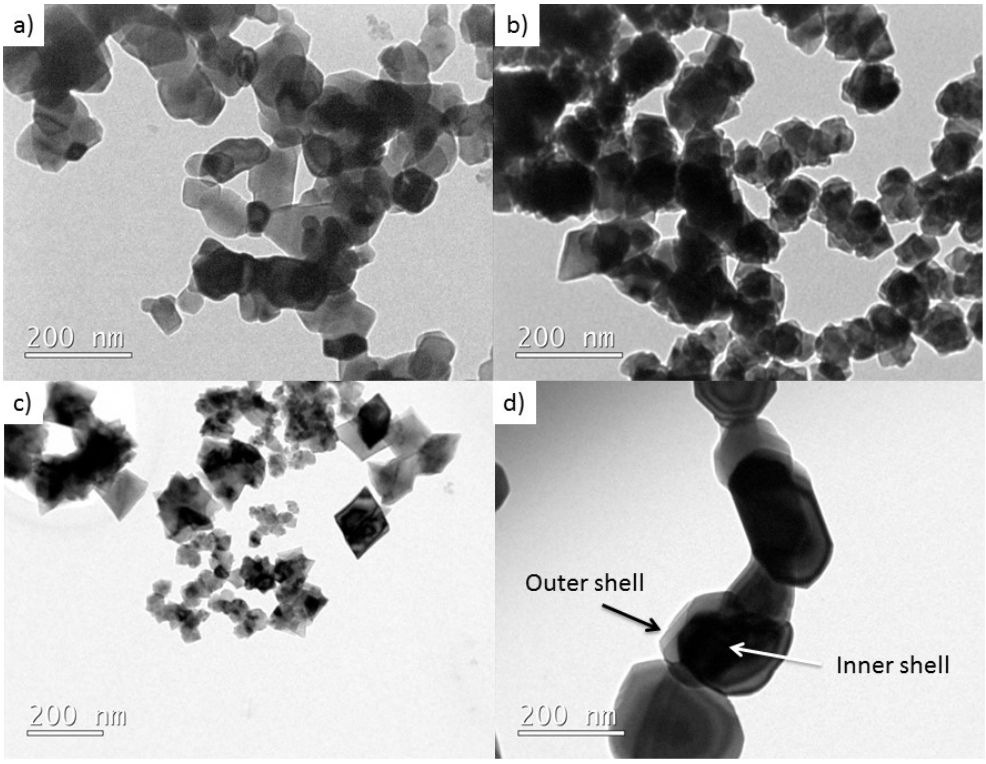

Figure 4.09: Transmission Electron Microscopy images for **(a)** Anatase, **(b)** Rutile, **(c)** Mixed anatase/rutile single shell structures and **(d)** multi-shell rutile@anatase showing outer and inner shell structure.

BET analysis was used to determine the surface areas of the samples, which gave values of 3-12 m^2 g^{-1}, Table 4.2, which is in accordance with literature values for similar sized TiO_2 particles.[246] These values are significantly lower than those for standard commercial powders, such as P25, with literature values of 56 m^2 g^{-1}.[247] The BET results could be matched with the particle sizes observed in the above TEM images, Figure 4.09. It can be seen that the anatase and rutile samples have similar particle sizes in the TEM images and this matches well with the BET analysis which gave both as 5 m^2 g^{-1}. The mixed phase sample, Figure 4.09 (c), has the smallest particle sizes and the largest surface area by BET analysis. The multi-shelled sample has the largest particles, so having the lowest surface area is not surprising. The relatively low surface areas determined also suggested that the samples exhibited low porosity, suggesting that there is good coverage by FBCVD synthesis.

Scherrer analysis of the particle sizes, Table 4.2, was also in agreement with the TEM images- with the average size estimated from the TEM being 50-70 nm. As shown, the Scherrer analysis gives very similar particle sizes.

Sample	S_{BET} (m^2 g^{-1})	Scherrer Size (nm)
Anatase	5	65
Mixed Anatase/Rutile	12	60
Rutile	5	58
Multi-shell Rutile@Anatase	3	63

Table 4.2: BET surface area analysis and Scherrer size analysis for samples Anatase, Mixed Anatase/Rutile, Rutile and Multi-shell Rutile@Anatase synthesised by FBCVD of $TiCl_4$ and Ethyl Acetate. All samples were post annealed (Table 4.1) before BET and Scherrer analysis.

4.3.2.4 Photocatalytic properties

To evaluate the photocatalytic properties of the samples, stearic acid destruction measurements were obtained. Stearic acid is a model organic pollutant that is stable to UV degradation in the absence of a photocatalyst. The mineralisation of the acid results in the decomposition as previously shown in Equation 3.4. The mineralisation of stearic acid has zero order kinetics, and the degradation of the acid can be followed by FTIR measurements, as the C-H bands (between 2700-3000 cm^{-1}) will steadily decrease in intensity as the acid is degraded, shown in Figure 4.10.

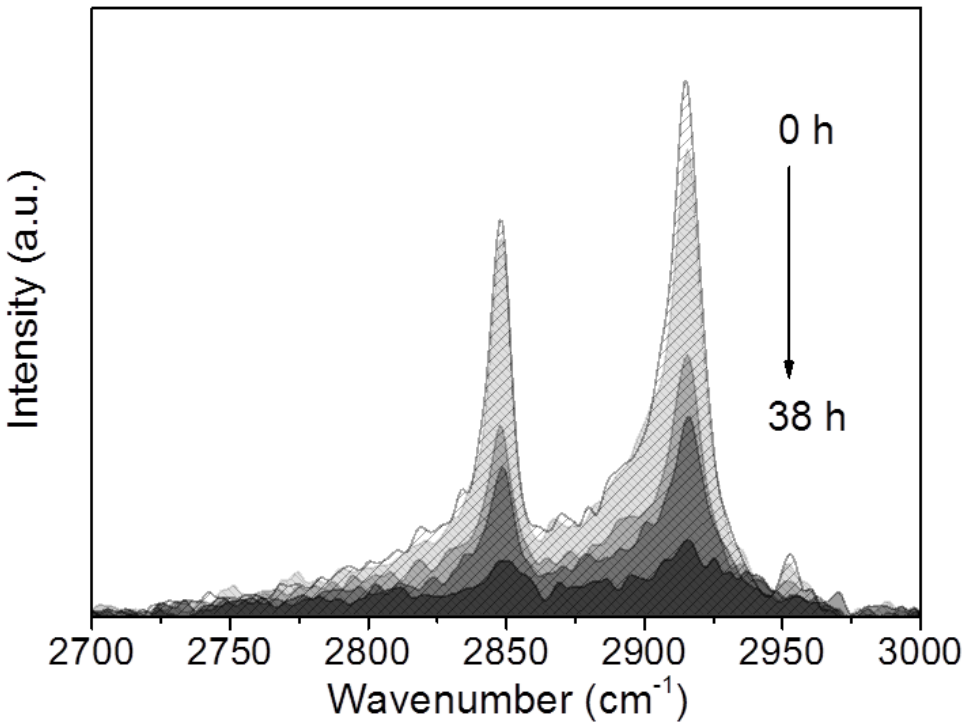

Figure 4.10: Typical IR spectrum of stearic acid showing the decrease in intensity of the characteristic C-H stretching frequencies during UV illumination on TiO_2 substrate over 38 hour exposure.

The integrated stearic acid destruction rates, Figure 4.11, show that the pure anatase sample has the highest photocatalytic potential of all the samples under UV irradiation. The rutile sample is practically inactive. Even though the rutile polymorph has a smaller band-gap, and so can utilise lower energy photons, it suffers from rapid recombination of photo-induced electrons and holes.[248, 249] The anatase sample is shown to have the greatest photocatalytic destruction of stearic acid under the UV irradiation. It is expected that the anatase polymorph will show higher photocatalytic rates than the rutile polymorph.[250]

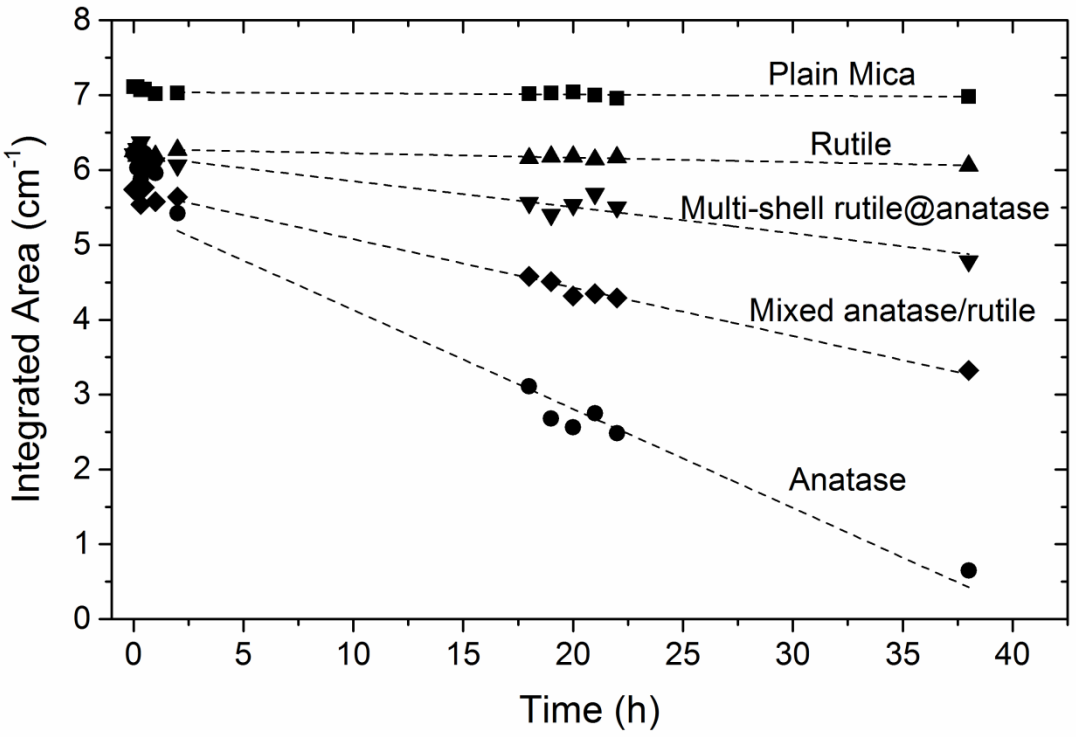

Figure 4.11: Integrated areas of stearic acid destruction for samples anatase, rutile, mixed anatase/rutile and multi-shell rutile@anatase under UVA irradiation (4 ± 0.2 mW cm^{-2}). Stearic acid destruction on uncoated mica substrate included as a reference.

The mixed anatase/rutile and multi-shell rutile@anatase samples showed rates that were intermediate of the two pure polymorphs of TiO_2. This was not unexpected when the UV/Vis and Tauc plots were taken into account. The photocatalytic rates observed mirrored the relative anatase/rutile contents of the samples, with the mixed anatase/rutile sample showing a higher anatase content and higher photocatalytic rate of stearic acid destruction, whilst the multi-shelled rutile@anatase sample showed a higher rutile content and a lower rate of stearic acid destruction.

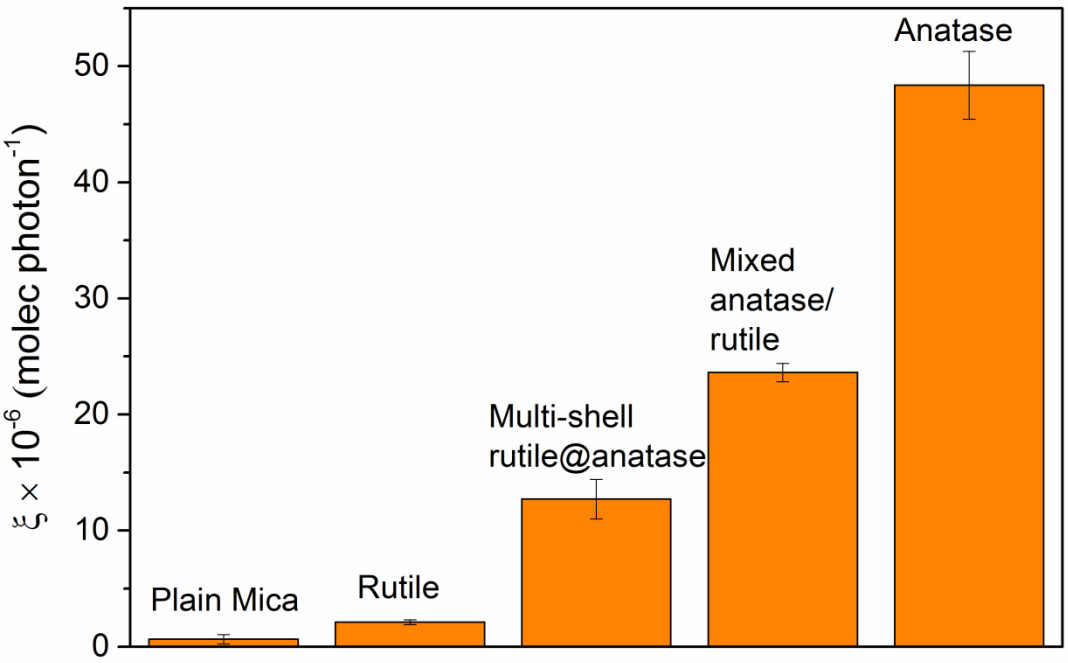

Figure 4.12: Formal quantum yields for all samples, showing the number of stearic acid molecules destroyed per photon absorbed.

The formal quantum yields (ξ), Figure 4.12, calculated for these samples are consistent with values for thin films (<100 nm) of TiO_2.[251] The photocatalytic activity can be expressed as formal quantum efficiency (ξ), defined as molecules degraded per incident photon (molec photon^{-1}). In this case, it was assumed that all incident photos were absorbed by the photocatalyst and they all had the same energy, corresponding to 365 nm (E = 3.39 eV).The formal quantum yields appear to be low at first glance, however for a single molecule of stearic acid to be completely destroyed requires 104 photons.[251] Once this is taken into account the process is not as inefficient as it first appears. It may seem surprising to state that these samples act more like thin films than nanoparticles of TiO_2, however, CVD techniques favour the formation of many small crystallites over single crystals. This is elucidated by the TEM images which clearly show layers rather than individual particles.

The surprising result was when the photocatalytic data was compared with other examples in the literature. There have been numerous reports of multi-component anatase/rutile systems that show superior photocatalytic rates to either pure anatase or rutile analogues.[244, 252, 253] This has been attributed by *Hurum et al*. to an effective charge transfer separation between the anatase and rutile polymorphs.[254] Further evidence for this process was shown by a study performed by *Scanlon et*

al.[255] This study also showed that the charge transfer from anatase to rutile was due to defects at the heterojunction level, with these defects acting as deep electron trap levels with the trapped electrons being ~1 eV below the rutile conduction band. A key proposed step in the photodegradation of organic molecules is the formation of hydroxyl and hydroperoxyl radicals (•OH, $•O_2H$), which are thought to form on the reaction of water with photogenerated holes.[256] Therefore, if the lifetime of the photogenerated holes can be increased, through a process such as electron trapping, there should be a subsequent increase in the photocatalytic destruction of organic molecules.

The results shown above would appear to contradict these other reported results. A reasonable explanation for the lower photocatalytic rates of both the mixed anatase/rutile and multi-shell rutile@anatase could be the exposure of the components. The multi-shell rutile@anatase structure has anatase at the surface of the particle, established from Raman spectroscopy, and a rutile core. This means that the rutile component is not exposed in this sample, exposure of both components of the system appear to be essential for increased photocatalytic activity. Studies where rutile TiO_2 has been both decorated and coated in anatase supports this.[252, 257] *Kandiel et al*.[252] synthesised rutile nanorods and decorated these with anatase nanospheres. Initially, photocatalytic rates of destruction increased, but as more anatase was deposited the rates decreased. *Zhang et al*.[257] observed a similar effect for H_2 evolution from anatase decorated rutile nanoparticles. When the anatase loading was increased above 15 wt.%, the activity of the samples began to decline.

Taking into account the need for both the rutile and anatase components to be exposed for increased photocatalytic rates, the results observed are not surprising. From the TEM images, it is clearly shown that the multi-shell rutile@anatase are uniformly coated with no obvious defects in the layers. This means that the electrons trapped in the rutile component are not going to be available for reduction of species on the surface of the particles. Instead, the rutile inner layer in each particle is going to act as a recombination centre- with subsequent reduction in photocatalytic rates.

The mixed anatase/rutile is slightly more complex, as the TEM images show a morphology that is intermediate of the pure rutile and anatase samples. This most likely means that there is a large, and relatively inactive, rutile component, with the

photocatalytic destruction of the stearic acid due to the anatase component that is still present in the sample.

4.4 Conclusions

The method reported in this chapter is a demonstration of a novel route towards multiple layered structures of TiO_2 on powder substrates *via* chemical vapour deposition. This is an easily scalable, cost-effective, cheap and high-throughput method for producing multi-shelled and core-shell structures of TiO_2- although currently a post-annealing process is required to ensure crystallinity. The CVD nature of the process also allows for the potential to tailor the material, through doping of the shells and shell thicknesses, to achieve the desired properties for the target material. There are also numerous combinations of materials that have been produced *via* CVD methods, which could potentially be produced on the FBCVD system, allowing for many potential multi-shelled systems to be investigated.

The initial experiments showed that while TiO_2 thin films could be deposited onto powder substrates, the crystallinity of the films were poor. This was addressed by a post-annealing process, which greatly improved the crystallinity and hence the photocatalytic properties of the films.

The poor crystallinity of the as deposited films was most likely due to poor thermal contact between the substrate and the reactor chamber. This did not, however, affect the ability to evenly coat the samples- as shown in the TEM images.

The single and multi-shelled materials synthesised have good coverage, as shown by the decrease in photocatalytic rates when in the multi-shell rutile@anatase. When the rutile component was encapsulated the result was a decrease in photocatalytic rates most likely due to a higher recombination rate of photo-induced electrons and holes. This demonstrated that the rutile and anatase polymorphs must both be exposed for an effective increase in photocatalysis to be observed, supporting research by other groups in the field.

The FBCVD method could be employed to coat desirable materials, such as photocatalysts, battery materials and thermochromic materials, onto templates to achieve morphologies that are not available by traditional CVD techniques. The current routes usually require methods, such as hydrothermal synthesis, that are not readily scalable and require long reaction times with expensive precursors.

Future work on the FBCVD system would be based around the production of core-shell structures for photocatalytic applications, such as $CuO@TiO_2$, $CdS@TiO_2$ and $ZnO@TiO_2$, as well as the production of exposed multi-layered systems. The latter idea could be achieved through the use of a template, such as carbon nanoparticles and fibres, which could be calcined after depositions of multiple layers leading to the exposure of both components of the system. These two research areas would allow for the study of both the interactions of these systems and the probing of the properties achieved as well as providing a scalable route to composite materials.

Chapter 5

Continuous Hydrothermal Flow Synthesis of VO_2 nanoparticles

Chapter 5: Hydrothermal Flow Synthesis of VO_2 nanoparticles

5.1 Introduction

The synthesis of monoclinic VO_2 nanoparticles has been an area of intense research for building fenestration.[152] This research is focused on reducing the absorption of visible wavelengths by VO_2 materials, which is aesthetically unpleasing brown/yellow colour. This is the primary reason for thin films of VO_2 not being implemented for energy efficient applications.[30, 133] Nanoparticle routes have been suggested as a possible route to alleviate the poor visible transmission inherent in thin films of VO_2.

Granqvist *et al*. have extensively modelled the use of nanoparticles of VO_2 and have suggested that reducing the size of the particles below 50 nm, as well as the incorporation of core-shell structures would maintain the thermochromic response whilst reducing absorption of visible wavelengths.[151, 183] This research has also been supported by experimental work which demonstrated the properties of such systems.[160]

Monoclinic VO_2 nanoparticles have been demonstrated by batch hydrothermal,[26, 29, 90, 258] ion implantation,[259, 260] reduction of V_2O_5 nanoparticles[261] and sol-gel synthetic techniques.[147] All of these methods, however, will be difficult to scale for industrial purposes due to long reaction times,[29, 262] i.e. 24-48 hours, low reaction yields,[147] high reaction temperatures[263, 264] (up to 800 °C) and expensive post formation processing to ensure phase purity.[190, 265]

Continuous Hydrothermal Flow Synthesis (CHFS) offers a possible route to produce highly crystalline monoclinic VO_2 nanoparticles in a high-throughput way. CHFS has been previously demonstrated for nanoparticle formation of TiO_2,[266] $NiCo_2O_4$,[267] In_2O_3,[268] Zn-Ce oxides[269] and ceramics.[270] In the CHFS process, nanoparticles are formed when an ambient stream of metal precursor is rapidly mixed with a supercritical (450 °C) stream of water. This usually results in the metal salt being hydrolysed and subsequently dehydrated forming the desired metal oxide.[86] This is a very rapid process, with typical reaction times of between 5-20 seconds.[271] This allows for large scale synthesis of nanoparticles, kg h^{-1}, with the reaction maintained as long as the metal precursor is fed and mixed with the supercritical water.[272]

Described within this chapter is a method for synthesising VO_2 nanoparticles from a CHFS process. The residence time (the length of time the nanoparticles were at the

mixing temperature, between 5-27 seconds) and mixing temperature were altered to determine the effect on the nanoparticles produced. This is the first demonstration of CHFS for the production of VO_2 nanoparticles, such a route would allow for the high-throughput synthesis of VO_2 nanoparticles with potential uses in battery[6, 8, 116] as well as thermochromic technologies.[28, 262]

5.1.1 The Continuous Hydrothermal Flow Synthesis reactor

The CHFS syntheses reported within this chapter were performed on a specially designed reactor. In a CHFS process, nanoparticles form when a stream of supercritical (or superheated) water (the supercritical water was at a temperature of 450 °C and 24.1 MPa) are mixed with a stream of an aqueous metal precursor (usually at room temperature). The mixing is achieved using a reactor (mixer) arrangement, during which a rapid conversion of the metal salt into metal oxide occurs by instantaneous hydrolysis and dehydration.[86] Figure 5.01 shows a schematic diagram of the CHFS process used to produce all samples discussed in this chapter. Three high-pressure diaphragm pumps P-1 to P-3 (Milton Roy, Primeroyal K) were used to supply reagents and water for the reactions. P-1 was used to supply the supercritical water for the process, the flow rate for this pump is defined as Q_{sw}. P-2 and P-3 were used to supply the aqueous metal precursor and D.I. water to the reactor respectively, as the streams are mixed before entering the reactor, the flow rates are defined together as Q_p.

Pump P-1 was used to supply a flow of deionised water, which was heated to 450 °C at a pressure of 24.1 MPa (i.e. above the critical point of water, T_c = 374 °C and P_c = 22.1 MPa) by pumping through a heating unit (7 kW). The combined feeds of P-2 and P-3 were mixed with the supercritical water feed, in a confined jet mixer (CJM), Figure 5.02. Within the mixer arrangement, supercritical water was mixed with the precursor streams this was achieved through a 1/4 ” Swagelok pipe fitted to a 3/8 ” cross using a 1/4 ” to 3/8 ” bored-through reducer, allowing the tube to extend into a stream of precursors issuing from P-2 and P-3, which were fed in below the outlet of the supercritical water. The nanoparticles formed remained at reaction (mixing) temperature for a particular ‘residence’ time. The nanoparticles were then rapidly cooled by passing through a pipe-in-pipe heat-exchanger. The resulting nanoparticle slurry was then collected in an open beaker at ~25 °C after passing through a back pressure regulator (TESCOM model 26-1762-24-194) valve.

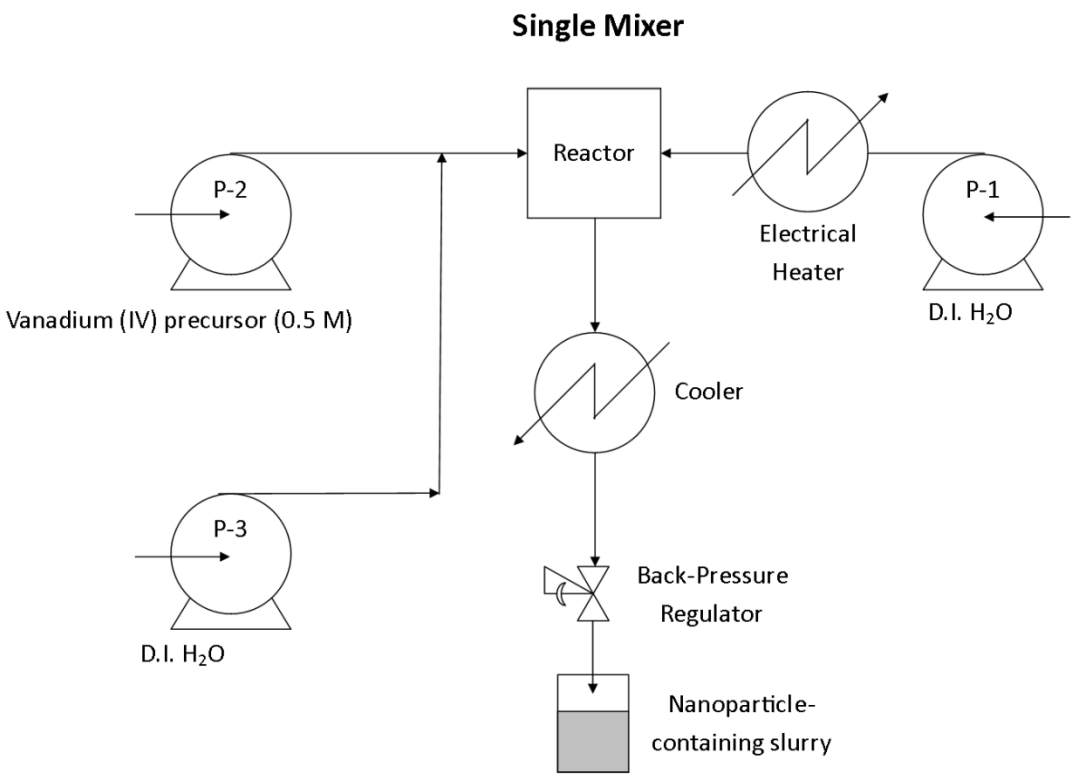

Figure 5.01: Schematic diagram of CHFS process used to produce VO_2 nanoparticles discussed in this chapter. Heater set-point was 450 °C for all samples discussed.

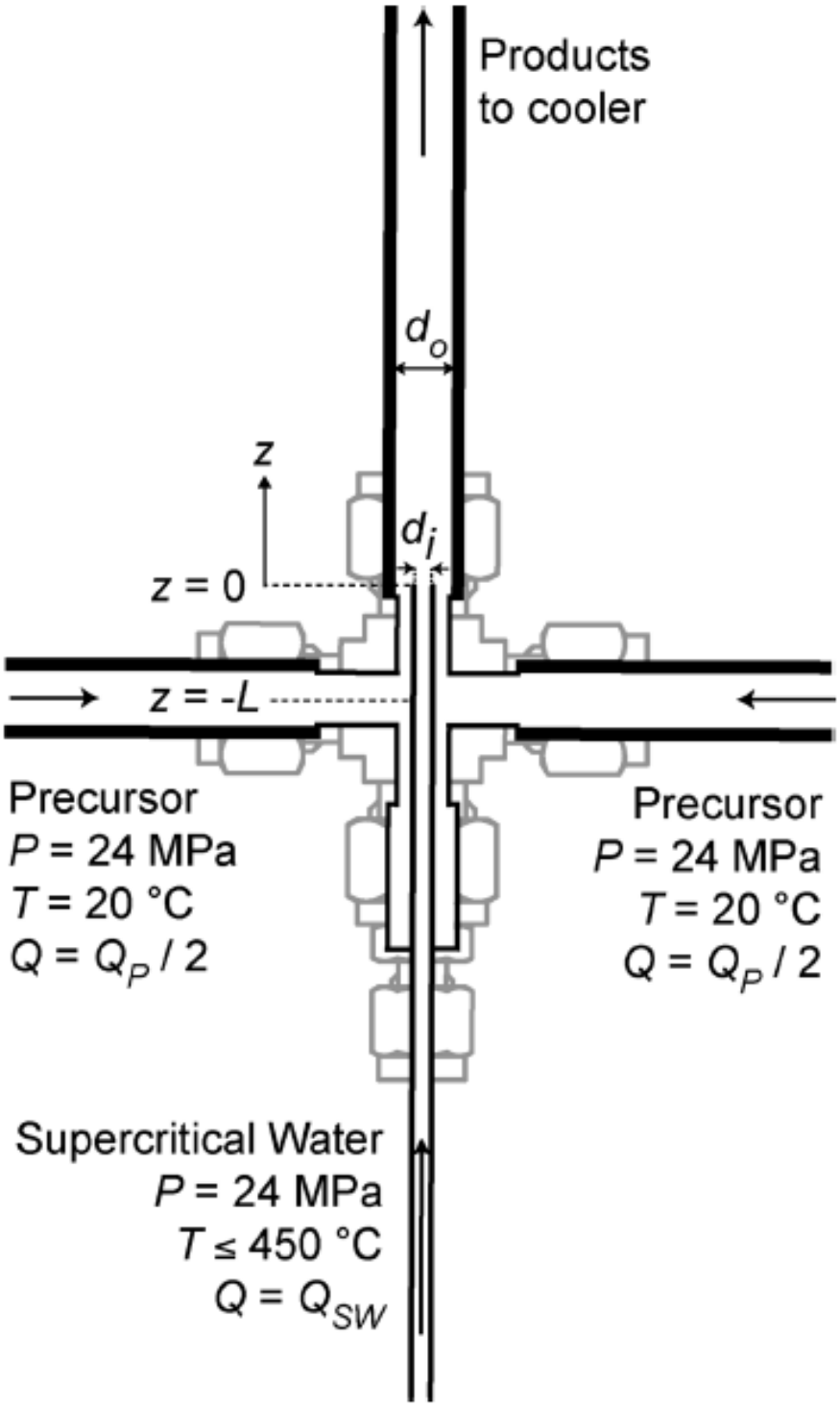

Figure 5.02: Geometry of confined jet mixer.[271] Figure used with permission from journal.

5.2 Synthesis of VO_2 nanoparticles by CHFS

5.2.1 Aim

To determine whether a CHFS process can be used to successfully synthesise VO_2 nanoparticles. To determine the phase/s formed and crystallinity of the nanoparticles produced. To determine the effect of mixing temperature and residence time on the phase/s and morphology of the nanoparticles synthesised.

5.2.2 Experimental

The synthesis of VO_2 nanoparticles was achieved by the reaction of a vanadium (IV) precursor solution. This solution was synthesised by the reduction of ammonium metavanadate (NH_4VO_3, 99.9% purity) by oxalic acid ($H_2C_2O_4 \cdot 2H_2O$, 99% purity) purchased from Sigma Aldrich and used without additional chemical treatment. The precursors were dissolved in DI water (15 MΩcm), from an Elga Purelab Option DV 25.

In a typical reaction, ammonium metavanadate (23.04 g : 0.2 mol) and oxalic acid (50.42 g : 0.4 mol) was dissolved in 2.0 L of DI water. The solution was stirred at room temperature for 4 hours, resulting in the formation of a deep blue solution. This was then left to age overnight. This resulted in a 0.1 M stock solution.

The as synthesised vanadium (IV) precursor solution would be transferred to P-2 for the synthesis of the nanoparticles, in a typical CHFS reaction 400 cm^3 of the stock solution was in the feed for P-2. The reactor set-point would be set to 450 °C and the pressures for P-1, P-2 and P-3 would be set. Once the reactor set-point had been reached, P-2 would be switched from the DI water feed to the precursor feed by a two-way valve. P-1 and P-3 would be left with DI water feeds flowing through them. The feeds generally took ~5 minutes to reach the mixer, with a black nanoparticle-containing slurry seen at the back pressure valve. Typically 900 cm^3 of slurry would be collected. This slurry would then be cleaned by centrifugation and washing, with DI water, followed by dialysis, for 24 hours, before being freeze dried (Virtis Genesis 35XL) by slowly heating from -40 °C to 25 °C over 24 hours under vacuum < 100 mTorr.

5.2.3 Sample descriptions

An initial series of 5 experiments were conducted, where the concentration of the vanadium precursor solution was altered and the addition of a base, to initiate crystallisation of the VO_2, was evaluated. These samples were characterised by powder X-ray diffraction and transmission electron microscopy. Sample descriptions and synthesis conditions for these initial reactions are summarised in Table 5.1.

A further series of 4 experiments were conducted, where the effect of residence time and mixing temperature on the phase and morphology of the VO_2 synthesised was evaluated. These samples were post annealed, ~1 g of material was in a crucible and heated in a tube furnace, fitted with Eurotherm controller, to 600 °C (ramp rate 20 °C min^{-1}) for 2 hours under a nitrogen atmosphere (BOC, 99.9%). The samples are then left to cool under a flow of nitrogen and were only removed when below 80 °C. These samples were characterised powder X-ray diffraction, Raman spectroscopy, UV/Vis spectroscopy, X-ray photoelectron spectroscopy and transmission electron microscopy. Sample descriptions and synthesis conditions for these variable residence times and mixing temperatures are summarised in Table 5.2.

Name	Mixing Temp (°C)	[VO_2] P-2 (mol/L)	[KOH] P-3 (mol/L)
VO_2	335	0.1	0
VO_2-B1	335	0.1	0.1
VO_2-B2	335	0.1	0.2
VO_2-B3	335	0.1	0.4
VO_2-B4	335	0.1	0.6

Table 5.1: Sample descriptions for initial VO_2 nanoparticles synthesised by CHFS, the concentration of the base was varied to determine the effect on the nanoparticles formed. Set-point temperature for all reactions was 450 °C.

Name	Mixing Temp (°C)	Q_{sw} (mL min^{-1})	Q_p (mL min^{-1})	Residence time (s)	$[VO_2]$ (mol/L)	Annealing conditions	
						Time (hrs)	Temp (°C)
VO_2-335	335	80	80	22	0.5	2	600
VO_2-356	356	76	62	22	0.5	2	600
VO_2-375	375	80	50	20	0.5	2	600
VO_2-357	357	64	52	27	0.5	2	600

Table 5.2: Sample descriptions for VO_2 nanoparticles synthesised with varying residence times and mixing temperatures. All samples were post annealed at 600 °C to ensure phase pure monoclinic VO_2. Set-point temperature for all reactions was 450 °C.

5.2.4 Nanoparticle characterisation

X-ray diffraction (XRD) studies were carried out using a Stoe (Mo) StadiP diffractometer. The instrument operates with a Mo X-ray source (Mo tube 50 kV 30 mA), monochromated (Pre-sample Ge (111) monochromator selects Kα1 only) and a Dectris Mython 1k silicon strip detector covering 18° 2θ. Samples were run in transmission mode, with the sample being rotated in the X-ray beam. The diffraction patterns obtained were compared with database standards. Raman spectroscopy was carried out using a Renishaw 1000 spectrometer equipped with a 633 nm laser. The Raman system was calibrated using a silicon reference. UV/vis spectroscopy was performed using a Perkin Elmer Lambda 950 UV/Vis/NIR Spectrophotometer. The absorption spectra were recorded *via* diffuse reflectance, with the samples being deposited onto microscope slides. Heating of samples in the UV/Vis spectrometer was achieved by an aluminium temperature cell controlled by RS cartridge heaters, Eurotherm temperature controllers and k-type thermocouples. A Labsphere reflectance standard was used as reference in the UV/vis measurements. Transmission electron microscopy (TEM) images were obtained using a TEM Jeol 2100 with a LaB6 source operating at an acceleration voltage of 200 kV. Micrographs were recorded on a Gatan Orius Charge-coupled device (CCD). The powders were sonicated and suspended in methanol and drop-casted onto a 400 Cu mesh lacey carbon film grid (Agar Scientific Ltd.) for TEM analysis. X-Ray photoelectron spectroscopy (XPS) was performed using a Thermo Scientific K-alpha spectrometer with monochromated Al Kα radiation, a dual beam charge

compensation system and constant pass energy of 50 eV (spot size 400 μm). Survey scans were collected in the range 0-1200 eV. XPS data was fitted using CasaXPS software, the vanadium $2p_{3/2}$ and O1s peaks were modelled with Gaussian functions. The Gaussian functions had a FWHM value of 1.8 and 1.7 for V^{5+} and V^{4+} respectively (with a tolerance of ±0.2) the oxygen had a FWHM of 1.8 (with a tolerance of ±0.2) these values were obtained from literature measurements.[166, 167]

5.3 Results and discussion

Nanoparticles of VO_2 were synthesised by CHFS. The nanoparticles were formed from a vanadium (IV) precursor solution, which was synthesised by the reduction of ammonium metavanadate by oxalic acid. This solution was used as the vanadium precursor for all reactions. The accepted reaction pathway between the metal carboxylate and oxalic acid is shown in equations 5.01, 5.02 and 5.03.[273, 274]

$$2\ NH_4VO_3 + 4\ H_2C_2O_4 \rightarrow (NH_4)_2[(VO)_2(C_2O_4)_3] + 2\ CO_2 + 4\ H_2O \qquad (5.01)$$

$$(NH_4)_2[(VO)_2(C_2O_4)_3] \rightarrow 2\ VO(C_2O_4) + 2\ NH_3 + CO + CO_2 + H_2O \qquad (5.02)$$

$$VO(C_2O_4) \rightarrow VO_2 + CO + CO_2 \qquad (5.03)$$

5.3.1 Initial VO_2 nanoparticle syntheses

Initial VO_2 nanoparticle syntheses were performed with the addition of a base, KOH, as for many CHFS reactions a base can facilitate nucleation of nanoparticles.[275] A range of base concentrations were studied, as summarised in Table 5.1.

Figure 5.03 shows the XRD patterns for the as formed VO_2 nanoparticles from the CHFS reactor. When compared to the ICSD standard pattern, it is obvious that sample VO_2 is the closest to the standard pattern. With the diffraction peaks at 12.7° (001), 16.9° (200), 19.1° (210), 24.8° (211) and 25.6° (022) (2θ, λ = 0.7093) being present for the XRD pattern for sample VO_2, whereas, these are not all present for the other samples produced. It can be seen from the patterns for samples VO_2-B1 to VO_2-B4 that the higher the concentration of base the fewer peaks that can be matched to the standard. For the highest concentration of base, VO_2-B4, additional peaks can be clearly identified. This suggests that additional phases are being

formed along with the VO_2. This could be caused by high pH levels oxidising or reducing the vanadium ions in solution- due to the amphoteric nature of vanadium.[276]

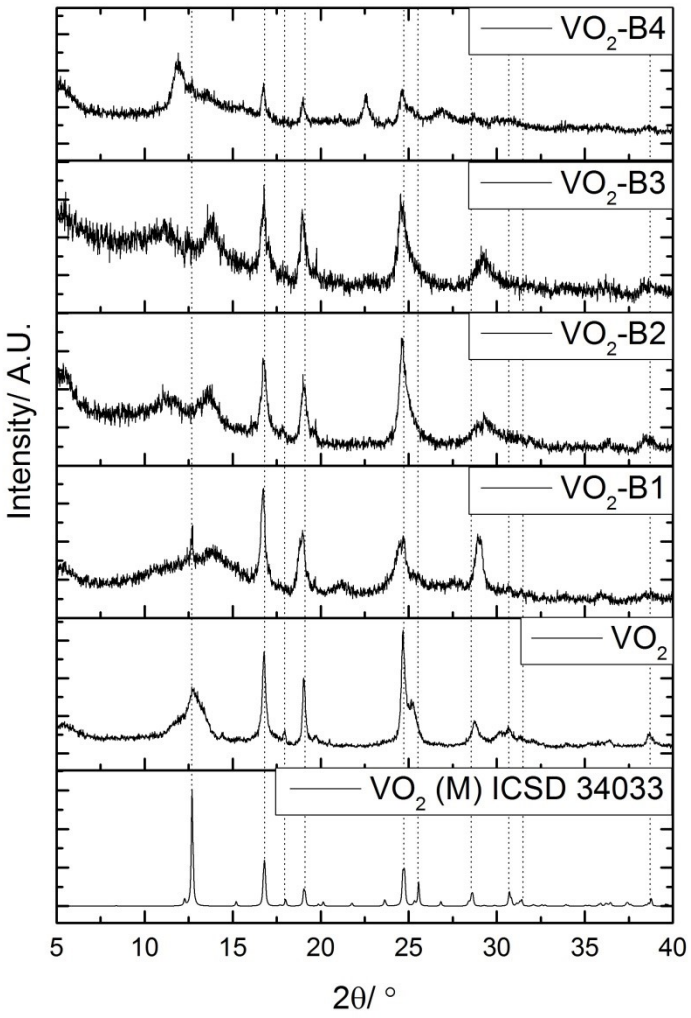

Figure 5.03: XRD patterns for initial reactions to form VO_2 nanoparticles by CHFS reactions. VO_2 is VO_2 formed directly from vanadium precursor without addition of base, VO_2-B1 is 1:1 vanadium precursor to base, VO_2-B2 is 1:2 vanadium precursor to base, VO_2-B3 is 1:4 vanadium precursor to base and VO_2-B4 is 1:6 vanadium precursor to base. λ = 0.7093 Å.

The phase purity of the samples synthesised can be estimated by the relative diffraction peak intensities in the XRD patterns. Even for sample VO_2, it can be seen that the intensities do not match the standard, with the peaks at 12.7° and 16.9° showing the opposite relationship in intensities to the standard pattern- suggesting that the as synthesised VO_2 particles are not phase pure. Interestingly, when

compared with the VO_2 (B) standard, the samples could not be matched to the diffraction peaks for the (B) phase. This suggests that the bulk material is closest to the monoclinic phase of VO_2.

TEM micrographs were obtained for sample VO_2, Figure 5.04. The sample morphology was roughly spherical with a large range in particle diameter from ~30 to ~100 nm in size. A closer inspection of the particle shape, Figure 5.04 (b), shows that the particles are more closely linked to a hexagonal structure than a spherical morphology, which suggests that there is preferential growth as the particles grow in the reaction. Figure 5.04 (c) and (d) show evidence for lattice fringes in the particles. This shows that the particles are highly crystalline, which is a surprising result as the residence time for the formation of these particles is ~10 s and this sample received no additional treatment after formation. The d-spacing gave a value of 0.35 nm, which was matched to the VO_2 (B) phase of VO_2.[6, 277] Interestingly, the TEM d-spacing disagreed with the XRD patterns for sample VO_2.

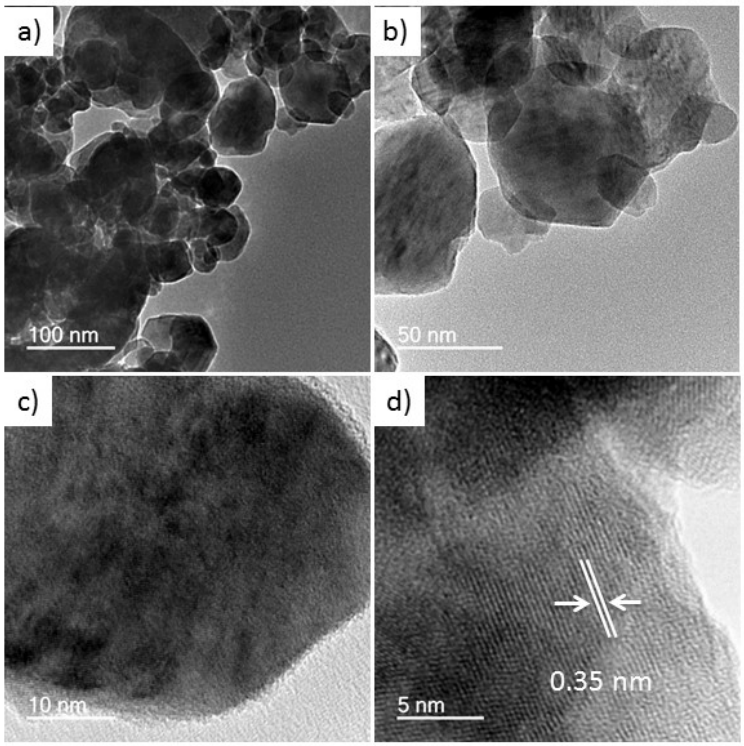

Figure 5.04: TEM micrographs for VO_2 nanoparticles (sample VO_2, no base) as formed from the CHFS process. **a)** Image showing range of spherical particle sizes from 100 to 30 nm diameter, **b)** Magnified image showing morphology of spherical particles showing more hexagonal features, **c)** close up image showing lattice fringes, **d)** lattice fringes from particles giving a d-spacing of 0.35 nm, which was matched to the VO_2 (B) (110) plane.

To ensure phase purity of the samples, a post-annealing treatment was performed on sample VO_2 to determine whether phase pure VO_2 (M) could be produced. Approx. 1 g of VO_2 was placed in a tube furnace and heated to 600 °C (ramp rate 20 °C min^{-1}) for 2 hours under a nitrogen atmosphere (BOC, 99.9%). Figure 5.05 shows the XRD pattern for sample VO_2 after the post annealing step. As shown, the diffraction peaks can now only be attributed to the monoclinic phase of VO_2, there is no evidence for any additional phases in the data. The relative intensities of the diffraction peaks to each other now also closely matches the standard XRD pattern-suggesting phase pure monoclinic VO_2 has been produced. Further evidence for the presence of the monoclinic phase of VO_2 was determined by TEM micrographs, Figure 5.06. The lattice fringes, which are even more pronounced in the post annealed sample of VO_2, gave a d-spacing of 0.32 nm, Figure 5.06 (d), which was matched to the (011) plane of monoclinic VO_2.[278, 279]

The HRTEM also gave information on the effect the post annealing had on the morphology of the nanoparticles. It can be clearly seen in Figure 5.06 (a) and (b) that the average particle size is significantly larger than in the un-annealed sample. The edges of the particles are also less clearly defined, suggesting that there has been sintering of the particles during the post annealing step. Evidence for sintering is further strengthened by the particle morphology in Figure 5.06 (b). Here it can be seen that the particles no longer have a spherical or hexagonal structure, instead a shape that is closer to two particles merging is evident. This suggests that there is Ostwald ripening, where particles aggregate becoming more rectangular, occurring during the post annealing.[92, 280, 281]

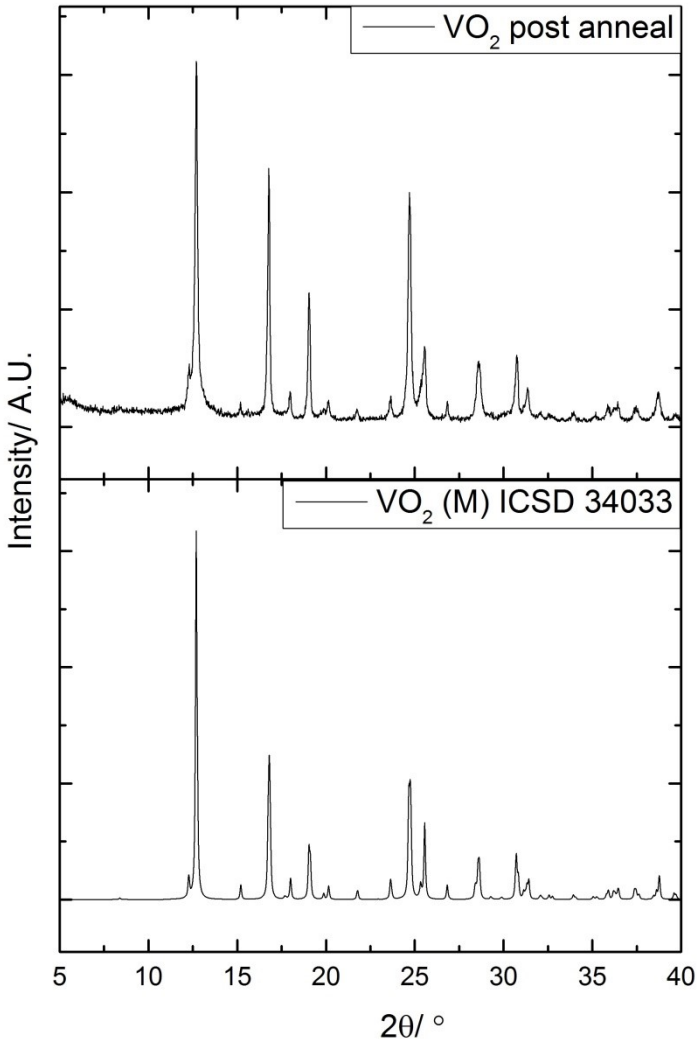

Figure 5.05: XRD pattern for sample VO_2 after post annealing treatment at 600 °C for 2 hours under a nitrogen atmosphere. The diffraction peaks in the data can only be attributed to VO_2 (M) there is no evidence for any additional phases. The relative intensities of the diffraction peaks to each other now also closely match the standard, suggesting phase pure monoclinic VO_2. λ = 0.7093 Å.

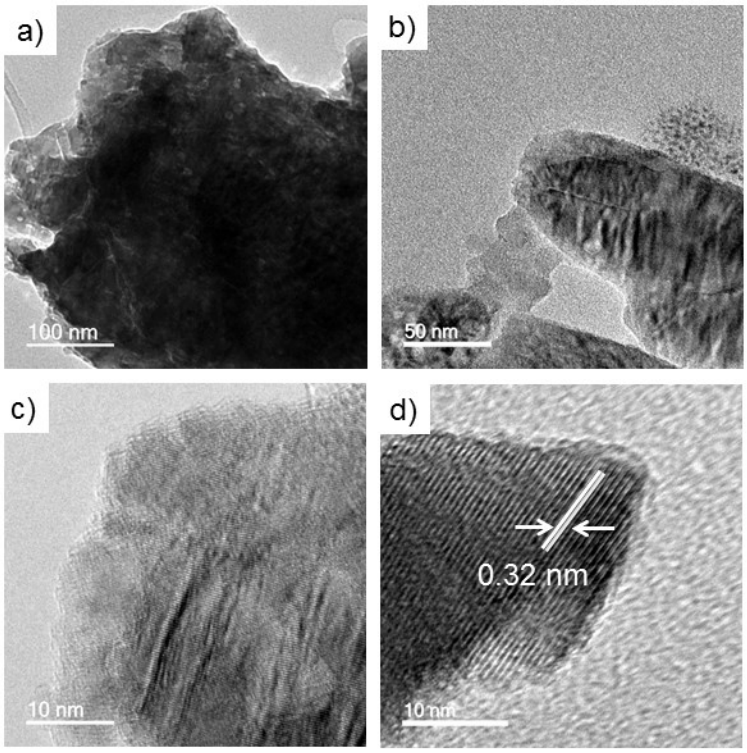

Figure 5.06: HRTEM micrographs for VO_2 post anneal; **a)** Particle morphology showing sintering effects, **b)** Micrograph showing Ostwald ripening effects in the nanoparticles, **c)** Lattice fringes for annealed particles and **d)** lattice fringes from nanoparticles gave a d-spacing of 0.32 nm which was matched to the (011) plane of VO_2 (M).

From these preliminary studies, it was concluded that the best route for producing monoclinic VO_2 nanoparticles was to use the vanadium (IV) precursor solution without the addition of base, as the XRD patterns showed that the VO_2 synthesised using only the vanadium (IV) precursor had the highest number of diffraction peaks that could be matched to monoclinic VO_2. The subsequent reactions in this chapter will look at the effect of mixing temperature and residence time to determine whether the formation of monoclinic VO_2 can be promoted.

5.3.2 The influence of residence time and mixing temperature on the formation of VO_2 nanoparticles synthesised by CHFS

5.3.2.1 Phase identification

A series of VO_2 nanoparticle samples were synthesised with the mixing temperature and residence time altered, as summarised in Table 5.2. The maximum residence time within the CHFS reactor for the nanoparticles was 27 seconds and the maximum mixing temperature was 375 °C.

XRD patterns were obtained for all the VO_2 samples as formed directly from the CHFS process, Figure 5.07. The XRD intensities correlate with the temperature of mixing, with sample VO_2-375 having the highest mixing (reaction) temperature and the closest match to the standard VO_2 (M) XRD pattern. The effect of residence time does not appear to have a large impact on the phase obtained, however, the difference between the residence times is very small only a maximum of 7 seconds. The surprising result was that nanoparticles of VO_2 could be formed in ~20 s that were close to the monoclinic phase, when similar reactions in batch hydrothermal processes require 1-2 days to achieve the same result.[28, 29, 90]

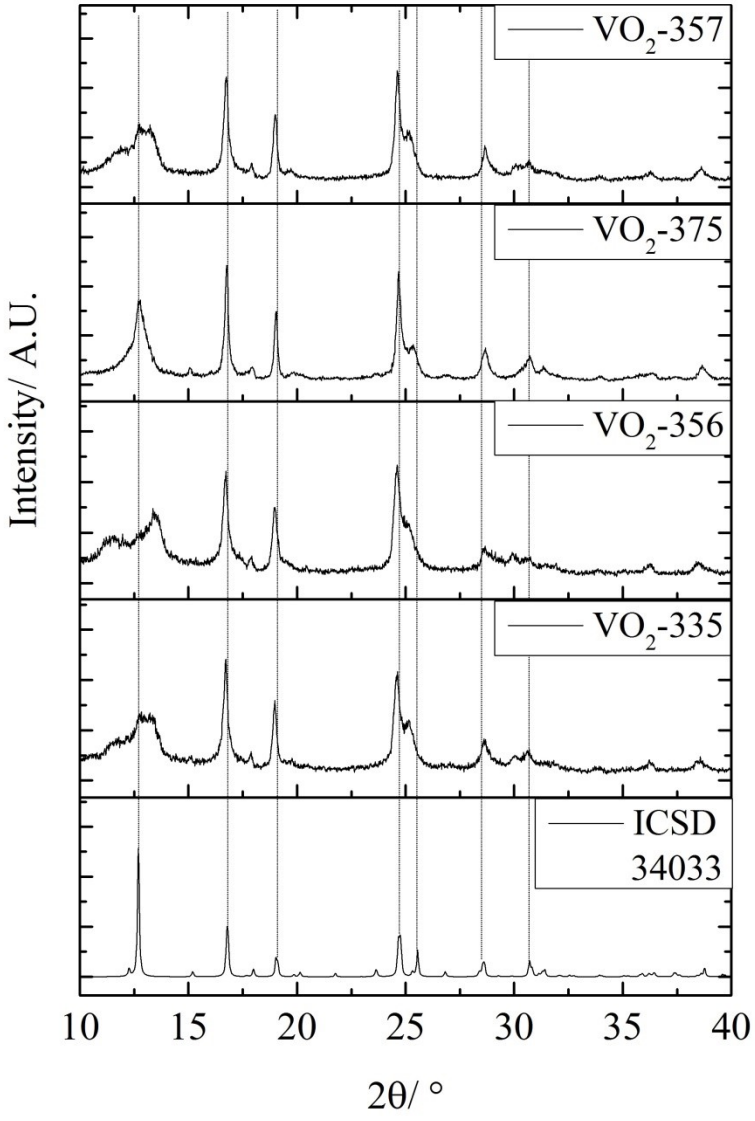

Figure 5.07: XRD patterns for VO_2 nanoparticles formed from CHFS process, VO_2-335 = 335 °C and 22 s, VO_2-356 = 356 °C and 22 s, VO_2-375 = 375 °C and 20 s and VO_2-357 = 357 °C and 27 s. All samples compared against ICSD VO_2 (M) standard (34033). λ = 0.7093 Å.

To ensure phase purity, all samples were post-annealed at 600 °C (ramp rate 20 °C min^{-1}) for 2 hours under a nitrogen atmosphere (BOC, 99.9%). After this post-annealing treatment, a further set of XRD patterns were obtained for the samples, Figure 5.08.

The diffraction peaks for all samples now match the ICSD VO_2 monoclinic, apart from a few additional peaks for sample VO_2-335 (labelled with an *) which was

attributed to an additional impurity phase of vanadium oxide. This was most likely a mixed oxide phase, known as a Magneli phase.[170, 282]

The relative intensities of the diffraction peaks now closely mirror the VO_2 monoclinic standard, suggesting that the nanoparticles are phase pure and crystalline. All of the XRD patterns show narrowing of the diffraction peaks, which suggests that the particles have sintered and become larger as a result. From the preliminary reactions, this is not a surprising result.

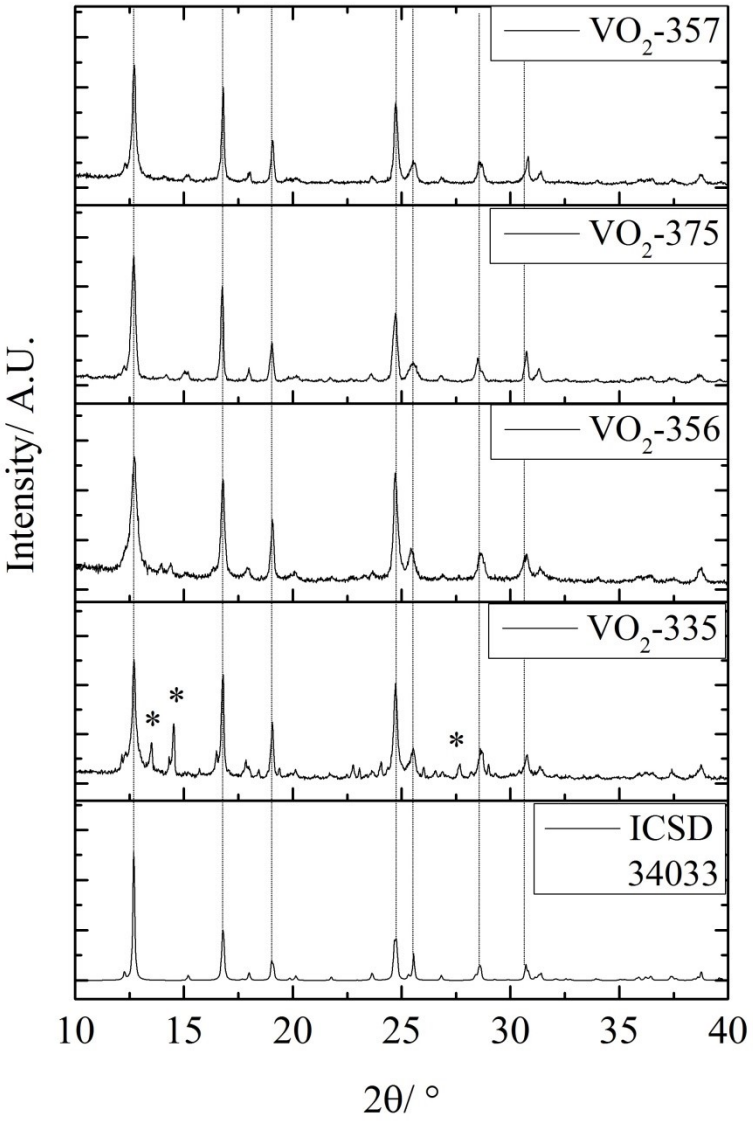

Figure 5.08: XRD patterns for post-annealed VO_2 samples. VO_2-335 = 335 °C and 22 s, VO_2-356 = 356 °C and 22 s, VO_2-375 = 375 °C and 20 s and VO_2-357 = 357 °C and 27 s. All samples are compared against ICSD VO_2 (M) standard (34033). Additional diffraction peaks are labelled with a (*). λ = 0.7093 Å.

To determine the phases present at the surface of the nanoparticles, Raman spectroscopy measurements were taken, Figure 5.09. The bands present in the spectra are attributed to monoclinic VO_2.[58] All the bands present are within ± 2 cm^{-1} of literature values.[174, 175]

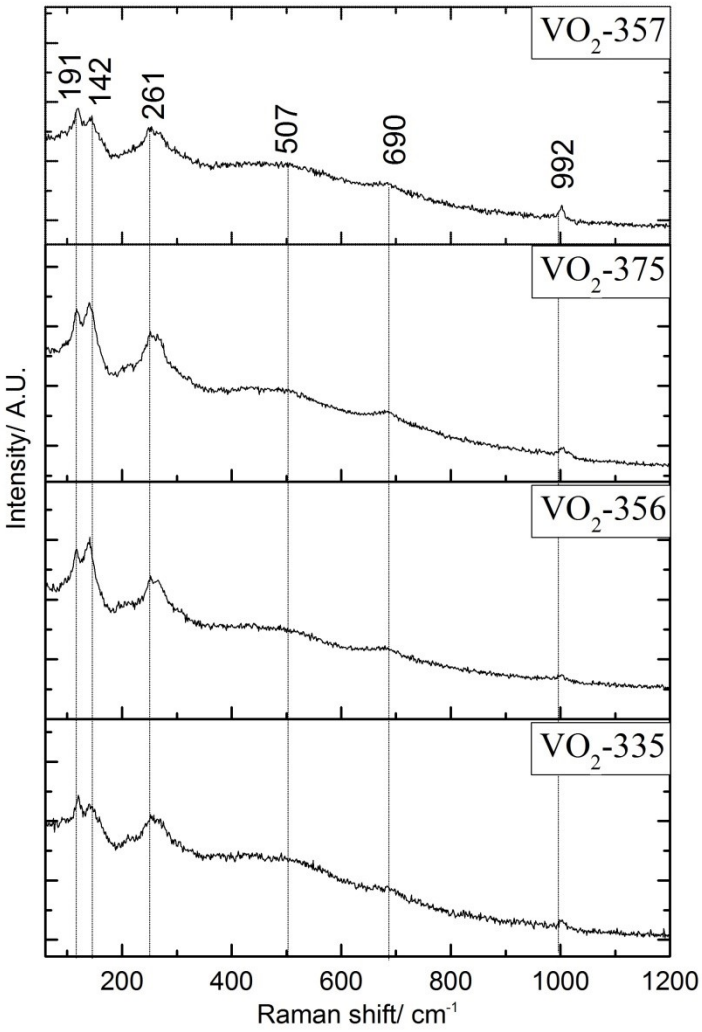

Figure 5.09: Raman spectra for all samples. VO_2-335 = 335 °C and 22 s, VO_2-356 = 356 °C and 22 s, VO_2-375 = 375 °C and 20 s and VO_2-357 = 357 °C and 27 s. All samples have been post-annealed at 600 °C for 2 hours under a nitrogen atmosphere. Band numbers shown are for monoclinic VO_2. Laser wavelength = 633 nm.

5.3.2.2 Morphology of nanoparticles

TEM micrographs were obtained for the post-annealed VO_2 samples, Figure 5.10. The first surprising result was the formation of rod-like geometries which had not been previously observed in the initial CHFS reactions. Samples VO_2-335, VO_2-356 and VO_2-357 displayed a mixture of rod and spherical like structures. Sample VO_2-375 showed only the spherical like structure and in this case the spheres had become more rectangular in nature, suggesting that there had been some sintering of the particles. As sample VO_2 and VO_2-375 show no evidence for rod-like formations after the post annealing process, the rods observed in samples VO_2-335, VO_2-356 and VO_2-357 are attributed to growth within the CHFS reactor and not growth during the post annealing process.

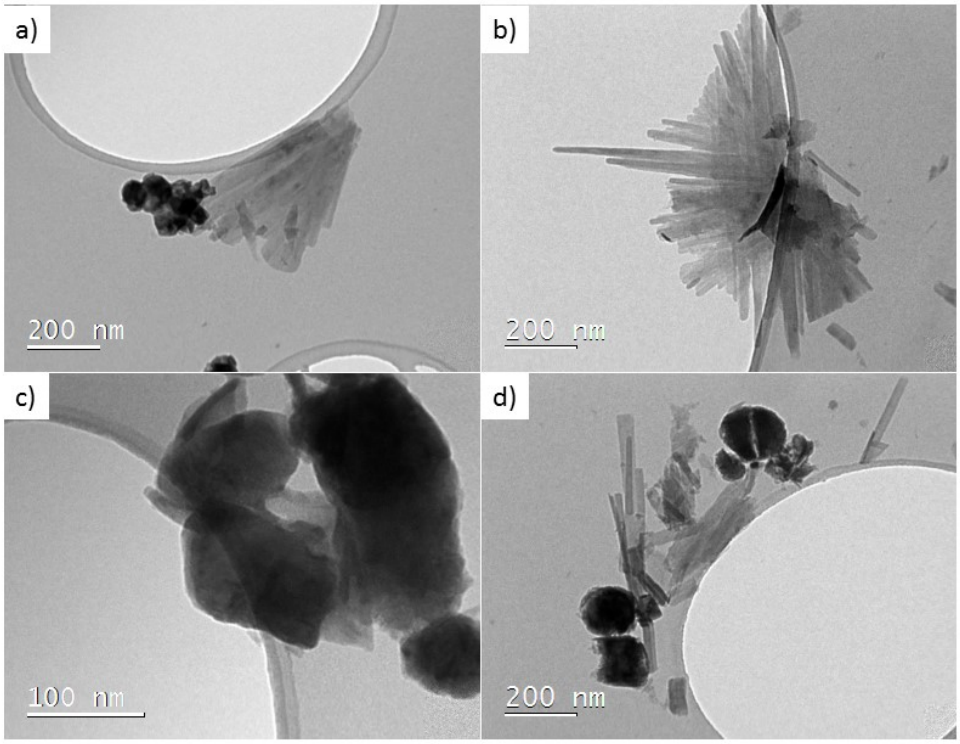

Figure 5.10: TEM micrographs for nanoparticles after post annealing process, **a)** VO_2-335 rod and spherical morphologies, **b)** VO_2-356 close up of rod morphology, **c)** VO_2-375 spherical-like particle showing evidence of more rectangular geometry and **d)** VO_2-357 spherical and rod-like morphologies. The rod-like morphologies are attributed to growth within the CHFS reactor and not the post-annealing processes.

Rod and spherical-like morphologies have both been previously reported for monoclinic VO_2 nanoparticles.[147, 278, 283] It is surprising to have both together in one sample this is attributed to the speed of particle formation, ~20 s, which would mean that the particles have little time to aggregate when forming.

The mean particle sizes were determined from the TEM micrographs, Table 5.3. The spherical mean particle sizes correlate well with the mixing temperature, with the lowest mixing temperature, sample VO_2-335, having the smallest mean particle size and the highest mixing temperature, sample VO_2-375, having the largest mean particle size. The rod-like morphologies also show a relationship with the temperature of mixing, with an increase in mix temperature leading to longer and thinner rod like structures- this again supports the conclusion that these morphologies are formed within the CHFS reactor and not during the post-annealing process.

The other notable features of the TEM micrographs are the nature by which the rod-like particles appear to grow. For sample VO_2-335, Figure 5.10 (a), the rod-like particles are all facing in a similar direction and the lengths and diameters of the rods are all very similar. This suggests that the particles may have had a relatively slow growth rate, allowing the particles to form these structures. This is in comparison to VO_2-356, Figure 5.10 (b), where the higher mixing temperature in VO_2-356 has caused the rod-like structures to grow from a centre point in all directions and although the diameters of the rods are similar to each other, the lengths of the individual rods are now very different. This suggests that the particle growth was much quicker, leading to the formation of these less ordered structures. This is argument is further strengthened by sample VO_2-357, Figure 5.10 (d), which had a similar mixing temperature to VO_2-356 but a longer residence time, 27 s as opposed to 22 s, in the CHFS reactor. The rod and spheres are showing many different particle sizes, with the overall structure being very chaotic. This suggests that the particles have begun to coalesce and aggregate as they are growing.[284]

Comparing sample VO_2 (mixing temp 335 °C, residence time 5 s) against VO_2-335 (mixing temp 335 °C, residence time 22 s) suggests that the initial particle growth in the CHFS process is a spherical particle growth, with rod-like morphologies forming as the residence time increases. The rod-like morphologies, as well as requiring long residence times, are temperature dependent, with higher mixing temperatures favouring spherical morphologies as demonstrated by sample VO_2-375. It has been previously observed that increasing the mixing temperature in CHFS processes

produces faster nucleation,[87] which could inhibit the formation of the rod-like particles.

Sample	Mixing Temp (°C)	Residence Time (s)	Mean particle size		
			Spherical Particles (nm)	Rod Particles (nm)	
				Length	Width
VO_2-335	335	22	46.3 (± 13.1)	239.9 (± 55.2)	68.3 (± 9.7)
VO_2-356	356	22	193.4 (± 38.9)	425.3 (± 49.8)	35.3 (± 5.2)
VO_2-375	375	20	339.2 (± 129.5)	Not Observed	Not observed
VO_2-357	357	27	131.9 (± 49.7)	159.8 (± 32.4)	54.3 (± 11.2)

Table 5.3: Mean particle sizes for spherical and rod-like particles observed post annealed VO_2 samples from the CHFS process.

5.3.2.3 X-ray Photoelectron Spectroscopy

To determine the oxidation state of the vanadium in the post annealed VO_2 powders, X-ray Photoelectron Spectroscopy (XPS) measurements were obtained. The binding energies for all elements were measured against carbon C1s (285.0 eV).

The surface vanadium oxidation state, Figure 5.11, was a mixture of V^{5+} (517.2 eV) and V^{4+} (515.7 eV). These values have been previously quoted for vanadium oxide species in the literature.[166] As with thin films, the surface vanadium species will readily oxidise forming V_2O_5. As the surface areas of the powders are much greater than for thin films, the proportion of V^{5+} to V^{4+} would be expected to be higher.

The O1s binding energy gave a similar result, with the deconvolution giving two oxygen environments, attributed to the binding of oxygen to the V^{5+} and V^{4+} in V_2O_5 and VO_2 respectively.[167]

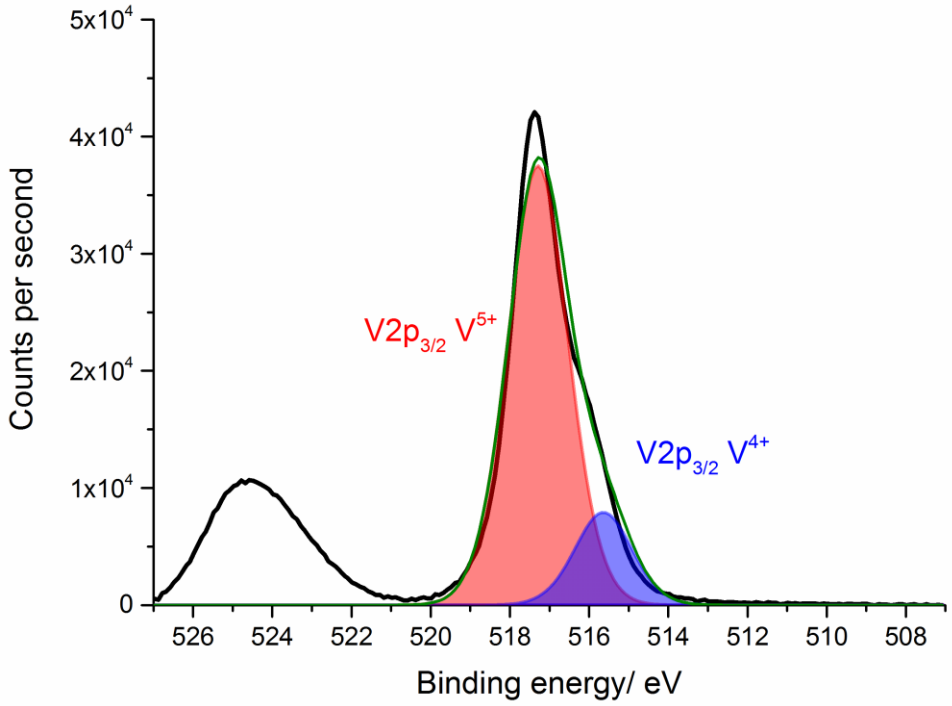

Figure 5.11: Surface XPS spectrum for vanadium binding energy from VO_2 nanoparticles synthesised by CHFS process.

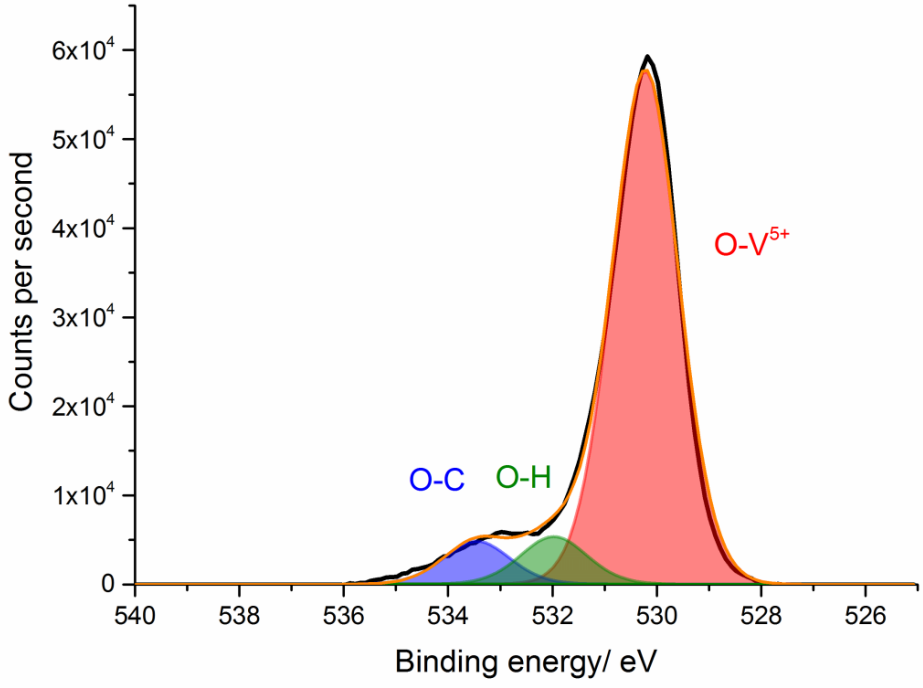

Figure 5.12: Surface XPS spectrum for oxygen binding energy from VO_2 nanoparticles synthesised by CHFS process.

5.3.2.4 Thermochromic properties of VO_2 nanoparticles

Variable temperature UV/Vis/NIR spectroscopy was employed to determine the thermochromic properties of the post-annealed VO_2 samples. For this, the powder was pressed into a pellet and reflectance measurements were obtained. With the tetragonal (rutile) phase being semi-metallic, upon the phase transformation (MST) from the monoclinic (cold) phase to the tetragonal (hot) phase, the expected result is an increase in reflectance in near IR wavelengths by the material when it is heated.[2]

All samples showed a reversible switch between the cold and hot spectra, Figure 5.13. The best performing sample was VO_2-375, which showed the largest switch between the cold and hot spectra (20% difference at 2500 nm). The worst performing sample was VO_2-335, which showed a significantly smaller switch (8% difference at 2500 nm). Interestingly, the switching behaviour displayed correlates with the initial XRD patterns, where VO_2-375 showed the greatest number of VO_2 monoclinic diffractions peaks and sample VO_2-335 the fewest.

The results also correlate with the particle size, with VO_2-375 having the largest particles and VO_2-335 the smallest. Combined with the XPS data, the difference in switching behaviour could be due to the proportion of VO_2:V_2O_5 in the samples- as VO_2-335 has significantly smaller particles that the other samples, it would also have the highest surface area and thus the lowest proportion of VO_2:V_2O_5. As V_2O_5 does not show a phase change at ~68 °C,[2] it will not contribute to the thermochromic response. Sample VO_2-375 has a much larger average particle size and so a higher proportion of VO_2, which would mean a larger thermochromic response. The influence of the ratio of VO_2:V_2O_5 on the thermochromic response has been previously reported for thin film systems.[149, 285]

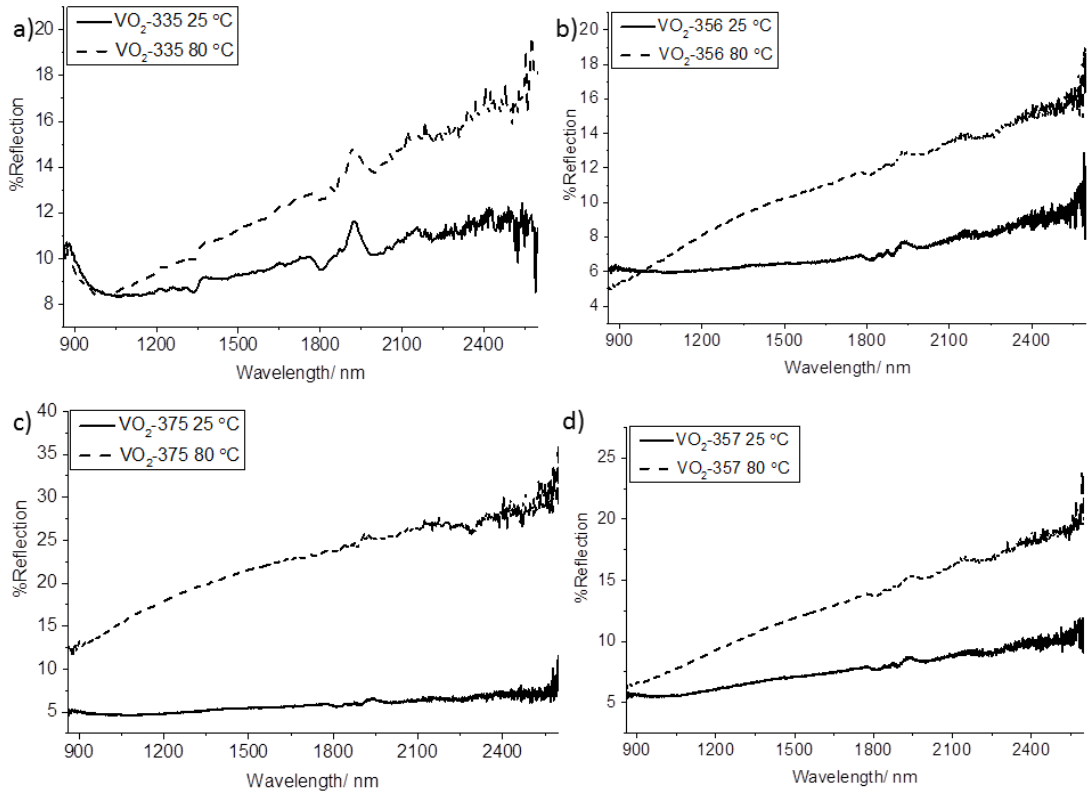

Figure 5.13: Variable temperature reflectance UV/Vis spectra for **a)** VO_2-335 **b)** VO_2-356 **c)** VO_2-375 and **d)** VO_2-357. All samples were measured at 25 °C (solid line) and 85 °C (dashed line). All samples shown have been post annealed at 600 °C for 2 hours under a nitrogen atmosphere.

Previous reports into the production of VO_2 nanoparticles have shown that the ability to tailor the shape can be desirable for a number of different applications. The initial TEM results suggested that as well as forming some VO_2 (M), there is also the formation of the metastable VO_2 (B) phase in the CHFS process. VO_2 (B) has been widely researched for the intercalation of lithium ions for battery technologies.[6, 8] It has been suggested that having a rod-like morphology would be advantageous for such a technology.[286] With longer residence times favouring rod-like formations, and low temperatures favouring the VO_2 (B) phase, the CHFS process could be ideal for the high-throughput production of VO_2 (B) nanoparticles.

It has been previously reported that the phase and morphology of materials produced by continuous hydrothermal methods can be influenced by the nature of the precursor,[287, 288] concentration of the precursor solution,[96] pH of the precursor solution,[96] addition of surfactants[94, 267, 289] and addition of dopants.[290] This means

there is plenty of scope for additional experiments to determine whether the direct synthesis of monoclinic VO_2 nanoparticles can be achieved from CHFS processes.

5.4 Conclusions

This chapter has reported on the synthesis of VO_2 nanoparticles by a continuous hydrothermal method. The addition of a base to the reaction mix was found to have a detrimental effect on the formation of monoclinic VO_2, leading to subsequent reactions being synthesised by the hydrolysis and dehydration of the vanadium (IV) precursor without addition of a base. The CHFS process was shown to produce highly crystalline nanoparticles, as demonstrated by the evidence of lattice fringes in the TEM micrographs of the initial VO_2 nanoparticles formed. The d-spacing from these lattice fringes were matched to the VO_2 (B) phase, combined with the XRD data suggested that the particles as formed were a mixture of (B) and (M) phases. Considering the short residence times in these initial experiments (~5 s), the crystallinity of the product was surprisingly high when compared with traditional batch hydrothermal processes, however, continuous hydrothermal processes have been proven to give highly crystalline products in very short reaction times. The as formed initial VO_2 powders required a post annealing step to ensure phase purity.

A further series of VO_2 nanoparticles were synthesised with the effect of residence time and mixing temperature investigated. The monoclinic diffraction peaks were found to become more intense in samples synthesised at higher mixing temperatures. Residence time did not appear to affect the phase formed, but impacted on the morphology with rod-like structures showing differing growth rates depending on the residence time in the CHFS reactor. Direct synthesis of phase pure monoclinic VO_2 was not observed, with a post annealing step required to obtain thermochromic properties. As with the initial experiments, the residence times were still very short, with a maximum of 27 s. The formation of a product with a high monoclinic VO_2 content, as shown by the XRD patterns, is therefore a very interesting result.

The data from this chapter suggests that the direct formation of VO_2 (M) may be possible, but would require higher reaction temperatures. Longer residence times may affect the phase present, but due to the small difference in residence time in the data presented here, it is unclear whether an increase in residence time would afford monoclinic VO_2 particles.

This is the first time that VO_2 nanoparticle formation has been shown from a CHFS process. In the next chapter, the influence of niobium as a dopant on the formation of VO_2 nanoparticles will be demonstrated.

Chapter 6

Continuous Hydrothermal Flow Synthesis of Nb-VO_2 nanoparticles

Chapter 6: Continuous Hydrothermal Flow Synthesis of Nb-VO_2 nanoparticles

6.1 Introduction

As stated in the previous chapter, the synthesis of VO_2 nanoparticles has been researched due to the aesthetically unpleasing brown/yellow colour of VO_2 thin films.[125, 151] Like undoped thin films and single crystals of VO_2, undoped nanoparticle systems also show a phase transition ~68 °C.[108] For use in fenestration, this phase transition would be required to switch ~25 °C.[18, 133, 158]

There are three potential routes to lower the phase transition temperature; by using a template to induce additional strain into the VO_2 lattice,[137, 291, 292] by reducing the size of nanoparticles synthesised[26, 29] and by the incorporation of dopants into the VO_2 lattice.[30, 31, 114, 132, 183] Of the three methods, doping of VO_2 has been shown to be the most reliable method for reducing the phase transition temperature.[108, 133, 183]

Reduction of the phase transition temperature in VO_2 has been achieved by doping with W,[57, 293, 294] Mo,[31, 119, 264] F[124, 295] and Nb.[9, 43] W, Mo and Nb have all shown a linear relationship with respect to doping levels, with each atom% of dopant incorporated into the lattice a known reduction in the phase transition temperature is observed.[43, 119, 181]

Doped nanoparticles have previously been achieved from batch hydrothermal,[26, 27, 29, 30] sol-gel[146, 189, 296] and sputtering[159, 297, 298] synthetic techniques. These techniques, however, suffer from difficulties in scaling for industrial purposes. This limits the applications of the nanoparticles from these synthetic routes.

As described in the previous chapter, Continuous Hydrothermal Flow Synthesis (CHFS) offers a potential route to the production of nanomaterials in a high-throughput and scalable manner. CHFS has also been proven to allow the incorporation of dopants into materials such as Zn-Ce oxides,[269, 272] nanoceramics,[270, 299] N-doped TiO_2[300] and Eu-doped ZrO_2.[301]

Described within this chapter is a method for synthesising Nb-doped VO_2 nanoparticles from a CHFS process. The concentration of the Nb-dopant was altered to determine the effect on the morphology and phase transition temperature of the particles produced. This is the first demonstration of the doping of VO_2 materials by a CHFS process. The Nb-VO_2 nanoparticles having potential to be used in thermochromic applications.[193]

6.1.1 The Continuous Hydrothermal Flow Synthesis reactor

Figure 6.01 shows a schematic of the reactor set-up used in the synthesis of the samples discussed in this chapter. Three high-pressure pumps P-1 to P-3 (Milton Roy, Primeroyal K) were used to supply reagents and water for the reactions. P-1 was used to supply supercritical water (450 °C) for the process. The flow rate for this pump is defined as Q_{sw}. P-2 and P-3 were used to supply the aqueous vanadium and aqueous niobium precursors respectively to the reactor. As these streams are mixed before entering the reactor, these are defined as Q_p.

Pump P-1 was used to supply a flow of deionised water (15 MΩcm), which was heated to 450 °C at a pressure of 24.1 MPa (as mentioned in the previous chapter, this is above the critical point of water; T_c = 374 °C and P_c = 22.1 MPa) by pumping through a heating unit (7 kW). The combined feeds from pumps P-2 and P-3 were mixed with the supercritical water feed in a combined jet mixer, as shown in the previous chapter (Figure 5.02). In the mixer arrangement, supercritical water was mixed with the precursor streams; this was achieved through a 1/4 " Swagelok pipe fitted to a 3/8 " cross using a 1/4 " to 3/8 " bored through reducer, allowing the tube to extend into a stream of the precursors issuing from P-2 and P-3, which were fed in below the outlet of the supercritical water. The nanoparticles formed remained in the reaction (mixing) temperature for ~5 seconds, this is termed as the 'residence' time. The nanoparticles were then rapidly cooled by passing through a pipe-in-pipe heat-exchanger. The resulting nanoparticle slurry was then collected in an open beaker at ~25 °C after passing through a back pressure regulator (TESCOM model 26-1762-24-194) valve.

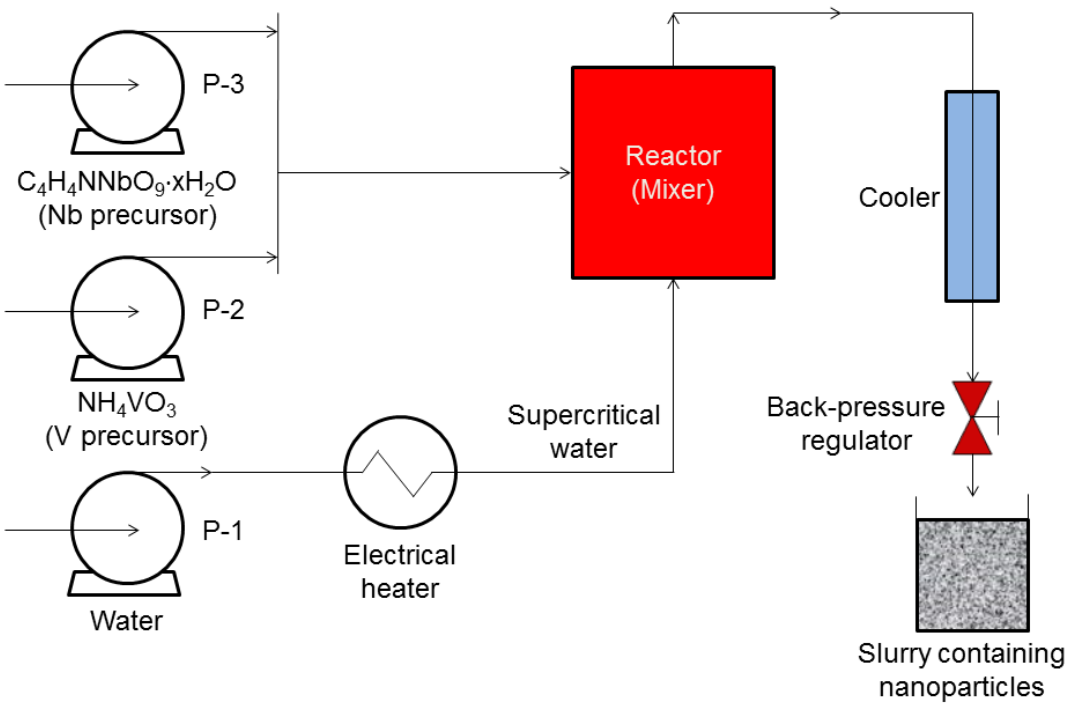

Figure 6.01: Schematic diagram of CHFS process used to produce Nb-doped VO_2 nanoparticles discussed in this chapter. Heater set-point was 450 °C in all cases.

6.2 Synthesis of Nb-VO_2 nanoparticles by CHFS

6.2.1 Aim

To determine whether the incorporation of Nb into VO_2 nanoparticles can be successfully achieved by CHFS. To determine the phase/s formed with increasing Nb concentration. To determine whether the Nb incorporation affects the morphology observed in the nanoparticles formed. To determine the effect on the phase transition temperature of increasing Nb content.

6.2.2 Experimental

The synthesis of the Nb-VO_2 nanoparticles was achieved by the reaction of a vanadium (IV) precursor with a Nb (V) precursor. The vanadium (IV) precursor was synthesised by the reduction of ammonium metavanadate (NH_4VO_3, 99.9% purity) by oxalic acid ($H_2C_2O_4$, 99% purity) in DI water (15 $M\Omega^{-cm}$). The Nb (V) precursor

was produced by dissolving ammonium niobate (V) oxalate hydrate ($C_4H_4NNbO_9.xH_2O$, 99.9 % purity) in DI water (15 MΩcm). All precursors were purchased from Sigma Aldrich and used without additional chemical treatment. The DI water was from an Elga Purelab Option DV 25.

For a typical vanadium (IV) precursor solution, ammonium metavanadate (23.04 g : 0.2 mol) and oxalic acid (50.42 g : 0.4 mol) was dissolved in 2.0 L of DI water. The resulting solution was stirred for 4 hours at room temperature, yielding a deep blue solution. This was then left to age overnight. This was used as a 0.1 M stock solution. For a typical niobium (V) precursor solution, ammonium niobate (V) oxalate hydrate (6.06 g : 0.02 mol) was dissolved in 2.0 L of DI water, this was left to stir until all the niobium precursor had dissolved. This resulted in a 0.01 M stock solution.

The vanadium (IV) precursor solution would be transferred to P-2 and the niobium (V) precursor would be transferred to P-3 for synthesis of Nb-VO_2 particles. In a typical CHFS reaction, 400 cm^3 of the vanadium (IV) precursor would be transferred to the feed for P-2 and 400 cm^3 of the niobium (V) precursor would be transferred to the feed for P-3. The reactor set-point would be set to 450 °C, and the flow rates of pumps P-1, P-2 and P-3 would be set to 80, 40 and 40 mL min^{-1} respectively. Once the set-point had been reached, pumps P-2 and P-3 would be switched from the DI water feed to the precursor feed by a two-way valve. Pump P-1 would be left with a DI water feed flowing through it. The feeds generally took ~5 minutes to reach the mixer, with a black nanoparticle-containing slurry observed at the back pressure valve. Typically 900 cm^3 of slurry would be collected. This slurry would then be cleaned by centrifugation and washing with DI water, followed by dialysis, for 24 hours, before being freeze dried (Virtis Genesis 35XL) by slowly heating from -40 to 25 °C over 24 hours under vacuum < 100 mTorr.

6.2.3 Sample descriptions

A series of 4 samples were produced, with varying concentrations of niobium (V) precursor added to the feed for pump P-3. All samples were post annealed. For a typical post-anneal, ~1 g of material was placed in a crucible and heated in a tube furnace, fitted with Eurotherm controller, to 600 °C (ramp rate 20 °C min^{-1}) for 2 hours under a nitrogen atmosphere (BOC, 99.9%). The samples are then left to cool

under a flow of nitrogen and were only removed from the tube furnace when below 80 °C. Sample descriptions and synthesis conditions are summarised in Table 6.1.

Sample	Conc. Nb precursor ($M \times 10^{-3}$)	Target Nb conc. (at.%)	Actual Nb conc. (at.%)	MST Temp. (°C)
VO_2	(water)	–	–	64.8
Nb(1%)VO_2	0.5	1	0.8	70.5
Nb(5%)VO_2	2.5	5	6.8	46.4
Nb(15%)VO_2	10	15	21.0	52.8

Table 6.1: Sample descriptions for Nb-VO_2 nanoparticles synthesised by CHFS, the concentration of the niobium (V) precursor was varied by diluting the 0.01 M stock solution to achieve 1, 5 and 15% Nb contents with respect to the vanadium. Set-point temperature for all reactions was 450 °C.

6.2.4 Nanoparticle characterisation

X-ray diffraction (XRD) was carried out using a Stoe (Mo) StadiP diffractometer, with a Mo X-ray source (Mo tube 50 kV 30 mA), monochromated (Pre-sample Ge (111) monochromator selects Kα1 only, λ = 0.7093) and a Dectris Mython 1k silicon strip detector covering 18° (2θ). The samples were studied in transmission mode. The diffraction patterns obtained were compared with database standards (ICSD). A Renishaw 1000 spectrometer equipped with a 633 nm laser was used for the Raman spectroscopy studies. The system was calibrated using a silicon reference. UV/vis spectroscopy was carried out using a Perkin Elmer Lambda 950 UV/Vis/NIR Spectrophotometer. The spectra were recorded in transmission mode, with the samples being deposited onto microscope slides. A Labsphere reflectance standard was used as reference in the UV/vis measurements. Transmission electron microscopy (TEM) images were obtained using a TEM Jeol JEM-100CX II with a tungsten source operating at an acceleration voltage of 100 kV. Micrographs were recorded on a Gatan Erlangshen ES500W camera. The powders were sonicated, suspended in methanol and drop-casted onto a 400 Cu mesh lacey carbon film grid (Agar Scientific Ltd.). X-Ray photoelectron spectroscopy (XPS) studies were carried out using a Thermo K alpha spectrometer with monochromated Al K alpha radiation, a dual beam charge compensation system and constant pass energy of 50 eV.

Survey scans were collected in the range of 0 – 1200 eV. XPS data was fitted using CasaXPS software, the vanadium $2p_{3/2}$, O1s and $Nb3d_{5/2}$ peaks were modelled with Gaussian functions. The Gaussian functions had a FWHM value of 1.8 and 1.7 for V^{5+} and V^{4+} respectively (with a tolerance of ±0.2) the oxygen had a FWHM of 1.8 (with a tolerance of ±0.2) and the niobium had a FWHM value of 1.7 (±0.2) these values were obtained from literature measurements.[166, 167, 302]

6.3 Results and discussion

Nb-doped nanoparticles of VO_2 were synthesised by a CHFS process. The nanoparticles were formed from a vanadium (IV) and niobium (V) precursor. The vanadium (IV) precursor was synthesised by the reaction between a metal carboxylate (ammonium metavanadate) and oxalic acid, the reaction pathway for this has been discussed in chapter 5, equations 5.01, 5.02 and 5.03. Structures, such as ammonium niobate (V) oxalate hydrate, are known to undergo thermal decomposition.[303] This is the most likely route for the doping of Nb into structures through a hydrothermal synthetic route.

6.3.1 The effect of Nb dopant concentration on the formation and properties of VO_2 nanoparticles synthesised by CHFS

6.3.1.1 Phase identification

A series of Nb-doped nanoparticles were synthesised with the Nb precursor solution being varied from 0 to 15 atom% with respect to the vanadium. All samples are summarised in Table 6.1.

XRD patterns of the VO_2 nanoparticles, as formed directly from the CHFS process, showed that the samples were not phase pure, as was the case with the undoped VO_2 nanoparticles described in chapter 5. Therefore, all samples were post annealed for 2 hours at 600 °C (ramp rate 20 °C min^{-1}) under a nitrogen atmosphere (BOC, 99.9%). Figure 6.02 shows the XRD patterns for the post annealed samples.

The diffraction peaks for all the samples match the ICSD VO_2 monoclinic, apart from a few additional peaks for samples Nb(5%) VO_2 and Nb(15%) VO_2- these additional peaks could not be matched to either V_2O_3 or V_2O_5, but were close to Nb_2O_5 (±0.2° 2θ) coupled with the slight shift in the diffraction peaks for the doped VO_2 samples

suggest that there is incorporation of Nb into the VO_2 structure with the higher levels causing segregation of the niobium and the formation of a niobate phase.[304]

As with the samples in the previous chapter, the post annealed XRD patterns closely match the relative intensities of the reference pattern- suggesting high phase purity and crystallinity of the product. Finally, it is noted that sample Nb(15%) VO_2 has significantly broader peaks than the other XRD patterns shown, this suggests that the particle size is significantly smaller in this sample than the others synthesised.

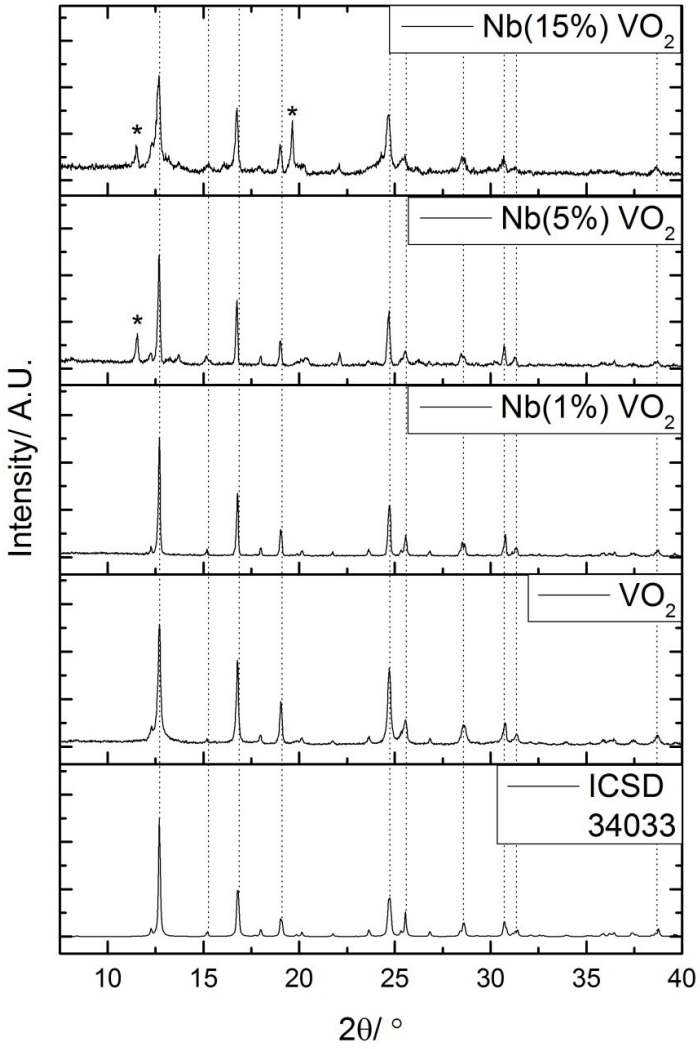

Figure 6.02: XRD patterns for Nb-VO_2 nanoparticles formed from the CHFS process, all samples were post-annealed at 600 °C for 2 hours under a N_2 atmosphere. Samples shown are VO_2 (undoped), Nb(1%) VO_2 (1 at.% Nb to V), Nb(5%) VO_2 (5 at.% Nb to V) and Nb(15%) VO_2 (15 at.% Nb to V). All samples are compared against ICSD VO_2 (M) standard (34033). The additional peaks could not be matched to V_2O_3 or V_2O_5, but were close to Nb_2O_5 (±0.2° 2θ). λ = 0.7093 Å.

To determine the phases present at the surface of the nanoparticles, Raman spectroscopy measurements were taken, Figure 6.03. Although VO_2 (M) bands could be identified for the undoped sample (Figure 5.08 in the previous chapter) the only phase identified for the Nb doped samples was V_2O_5, with characteristic bands at 997 cm^{-1} (V=O stretch); 696 and 524 cm^{-1} (V–O stretch of doubly and triply coordinated oxygen, respectively); 405 and 282 cm^{-1} (V=O bending); and 192, 141 and 94 cm^{-1} (lattice vibrations).[305] This is not completely unexpected, as surface vanadium will be rapidly oxidised to V^{5+}.[306] Combining the XRD and Raman data suggests that the bulk crystalline material is monoclinic VO_2, with the surface phase being V_2O_5.

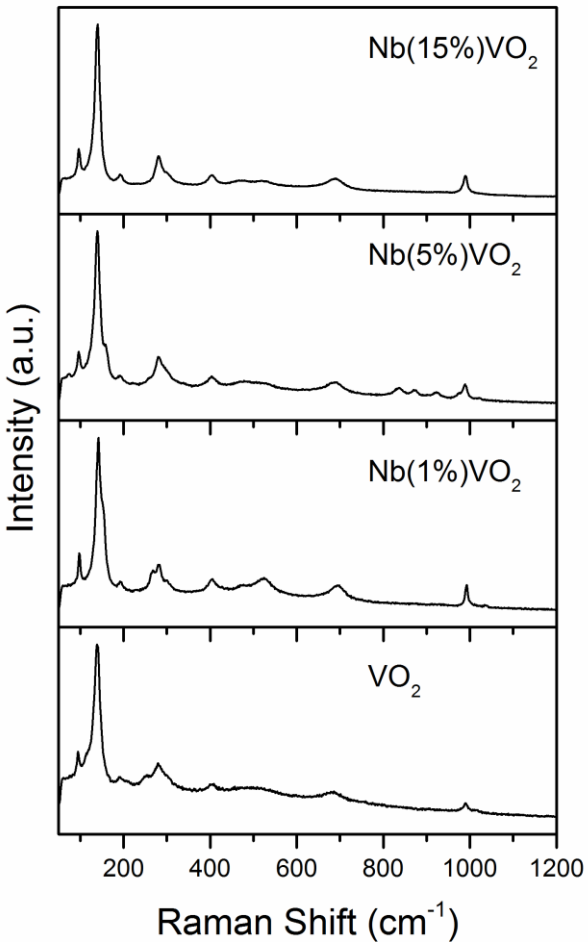

Figure 6.03: Raman spectra for all samples. Samples shown are VO_2 (undoped), Nb(1%) VO_2 (1 at.% Nb to V), Nb(5%) VO_2 (5 at.% Nb to V) and Nb(15%) VO_2 (15 at.% Nb to V). VO_2 All samples have been post annealed at 600 °C for 2 hours under a N_2 atmosphere. Laser wavelength = 633 nm.

6.3.1.2 Morphology of nanoparticles

TEM micrographs were obtained for the post-annealed Nb-VO_2 nanoparticle samples, Figure 6.04. Sample VO_2, Figure 6.04 (a), shows the morphology seen previously for the undoped monoclinic VO_2 synthesised by the CHFS, with a mixture of spherical and rod-like morphologies present in the TEM micrograph.

Sample Nb(1%) VO_2, Figure 6.04 (b), shows spherical and rod-like morphologies too. The rod-like particles now display growth patterns that are indicative of a central seeding point, with the rod-like morphologies growing from this point.

Sample Nb(5%) VO_2, Figure 6.04 (c), shows spherical and blade-like morphologies. The rod-like structures present in Figure 6.04 (a) and (b) are now replaced by these blades, which have greater particle widths but smaller particle lengths.

Sample Nb(15%) VO_2, Figure 6.04 (d), shows only spherical type morphologies. The spherical particles are significantly smaller in size than for the other samples shown. This is supported by the XRD patterns, which showed significant peak broadening for this sample, Figure 6.02. There is no evidence for the presence of either rod or blade-like morphologies. This when coupled with the smaller size of the particles suggests that the increasing niobium is acting as a seed for particle formation. Thus as the concentration of niobium increases smaller particles are formed, due to increased sites for nucleation.[29]

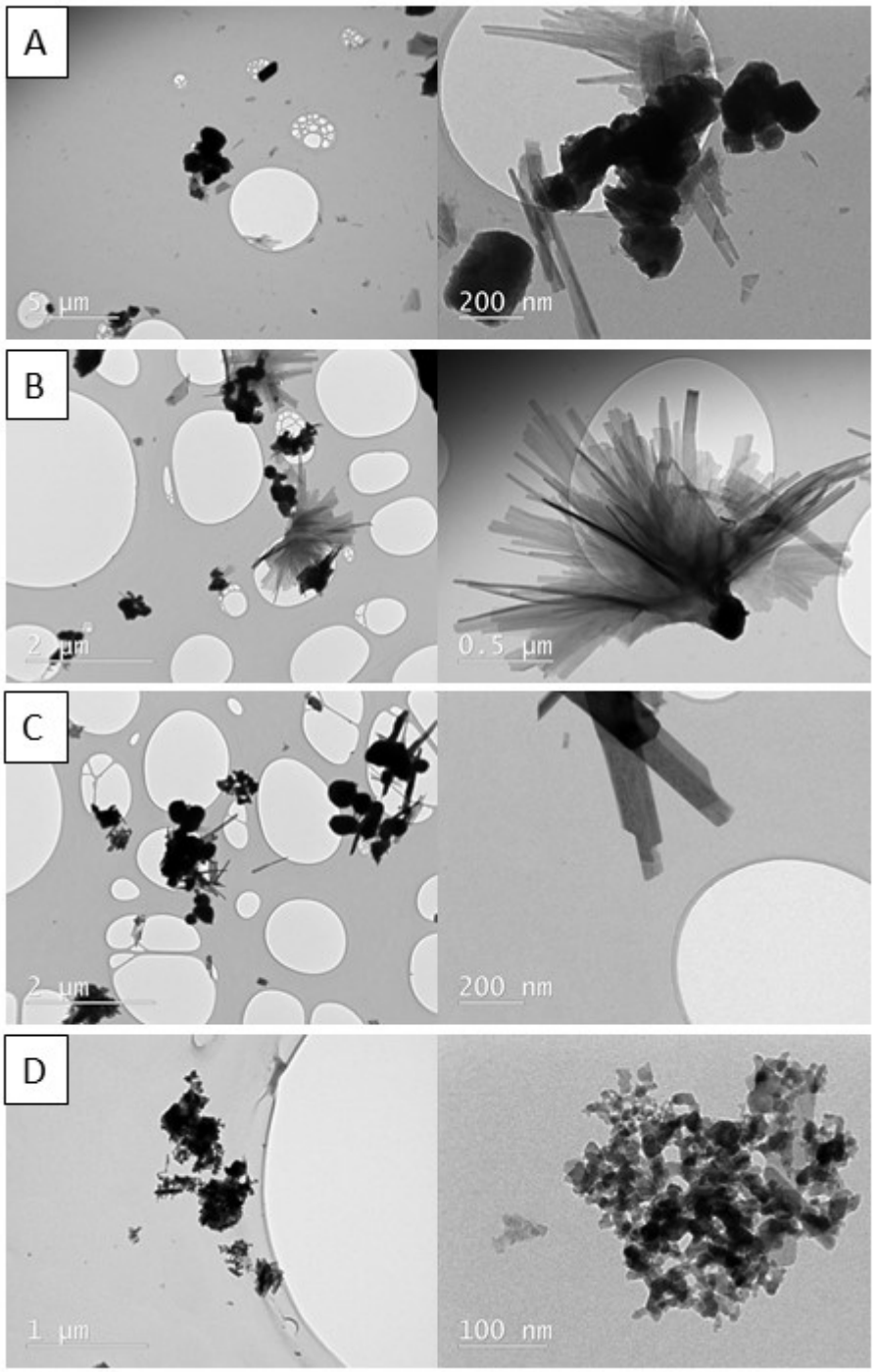

Figure 6.04: TEM micrographs for nanoparticles after post-annealing at 600 °C for 2 hours under a nitrogen atmosphere, **a)** sample VO_2 (undoped), **b)** Nb(1%) VO_2 (1 at.% Nb to V),**c)** Nb(5%) VO_2 (5 at.% Nb to V) and **d)** Nb(15%) VO_2 (15 at.% Nb to V). All TEM micrographs show a low and high magnification image to help elucidate particle morphologies present.

Analysis of the particle shapes and sizes, Table 6.2, shows the effect of increasing the niobium concentration on the particle size and morphology observed. It can be seen that the addition of low concentrations of niobium lead to the formation of both larger spherical and rod-like particles. When the Nb concentration is increased to 5%, this decreases both the spherical and blade-like particles, when compared with the 1% Nb samples. The particle sizes are still larger than those observed in the undoped VO_2 sample. At the highest concentration, 15% Nb, it can be seen that the particle size is significantly reduced. This suggests that there is a critical concentration of niobium above which the nucleation rate is very high, causing the formation of many small particles.

Sample	**%Niobium in precursor solution**	**%Niobium from X-ray Photoelectron spectroscopy**	**Mean Particle Size (nm)**		
			Spherical Particles (nm)	**Rod/blade particles (nm)**	
				Length	**Width**
VO_2	0	0	203.4 (± 47.3)	670.3 (± 143.8)	34.5 (± 7.8)
Nb(1%) VO_2	1	0.8	634.1 (± 211.8)	1507.8 (± 511.0)	140.4 (± 72.3)
Nb(5%) VO_2	5	6.8	252.5 (± 127.9)	962.2 (± 130.7)	152.6 (± 25.3)
Nb(15%) VO_2	15	21.0	26.2 (± 6.0)	Not Observed	Not Observed

Table 6.2: Mean particle sizes for spherical and rod/blade like particles observed in the post annealed samples from the CHFS process.

6.3.1.3 X-ray Photoelectron Spectroscopy

To determine the oxidation states of the vanadium and niobium in the post annealed Nb-VO_2 powders, XPS measurements were obtained. The binding energies for all elements were calibrated to the carbon C1s peak (285.0 eV).

The surface vanadium oxidation state for the undoped VO_2 sample, Figure 6.05, showed a similar mixture of V^{5+} (517.1 eV) and V^{4+} (515.7 eV) as seen in for the undoped samples from the CHFS in the previous chapter. These values are in agreement with the literature.[166] The inclusion of niobium, however, reduced the proportion of V^{5+} in the sample. The areas under the peaks in the XPS spectra were used to determine the proportion of V^{5+} : V^{4+}, Table 6.3. The increase in the niobium content is accompanied by a decrease in the proportion of V^{5+} in the samples.

The oxygen binding energies show a similar trend, with the undoped sample, Figure 6.07, showing only of V^{5+}-O signals, attributed to V_2O_5.[167] When niobium is in high concentrations, Figure 6.08, the O1s shows two V-O environments attributed to V^{4+} and V^{5+}. The other environments present in the O1s XPS spectra are attributed to hydroxyl groups and surface carbon contamination.

Finally, the Nb oxidation environment, Figure 6.09, can only be deconvoluted to give Nb^{5+} in all Nb-doped VO_2 samples, there was no evidence for any other oxidation states of niobium being present in any of the Nb-doped samples. The binding energy for this is 207.4 eV which is in agreement with literature values.[307] The peak areas for the niobium were also used to estimate the % incorporation of Nb into the VO_2 samples, the values calculated roughly match the target values, however, the highest concentrations suggest that niobium uptake is selected for at higher doping concentrations. This could be due to the seeding effect of the niobium as suggested from the TEM micrographs, Figure 6.04 (d).

The XPS spectra suggest that the inclusion of high concentrations of niobium helps to reduce the vanadium from (V) to (IV). This could be due to the effect of the overlap of the Nb d-orbitals with the V d-orbitals, allowing the transfer of electrons from the niobium to the vanadium as has been previously suggested.[32, 308]

Sample	Target Nb%	Nb% from XPS	V^{5+} : V^{4+} (%)
VO_2	-	-	83 : 17
Nb(1%) VO_2	1%	0.8	77 : 23
Nb(5%) VO_2	5%	6.8	75 : 25
Nb(15%) VO_2	15%	21.0	66 : 34

Table 6.3: Niobium content against the relative proportion of V^{5+} : V^{4+} for Nb-VO_2 samples synthesised by CHFS process.

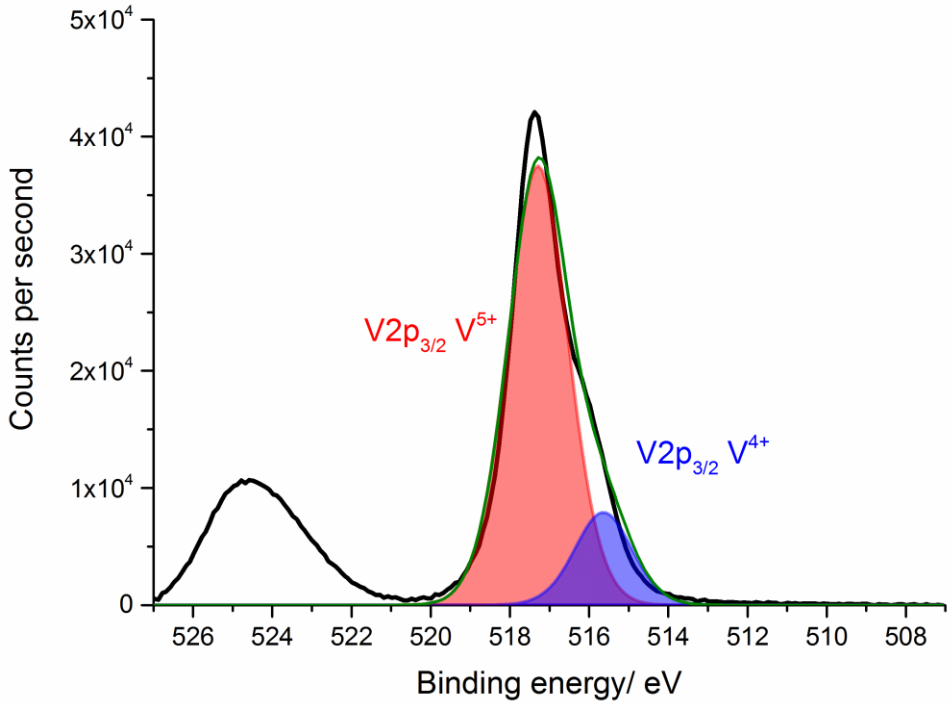

Figure 6.05: Surface XPS spectrum for vanadium binding energy from undoped VO_2 nanoparticles, sample VO_2, synthesised by CHFS process.

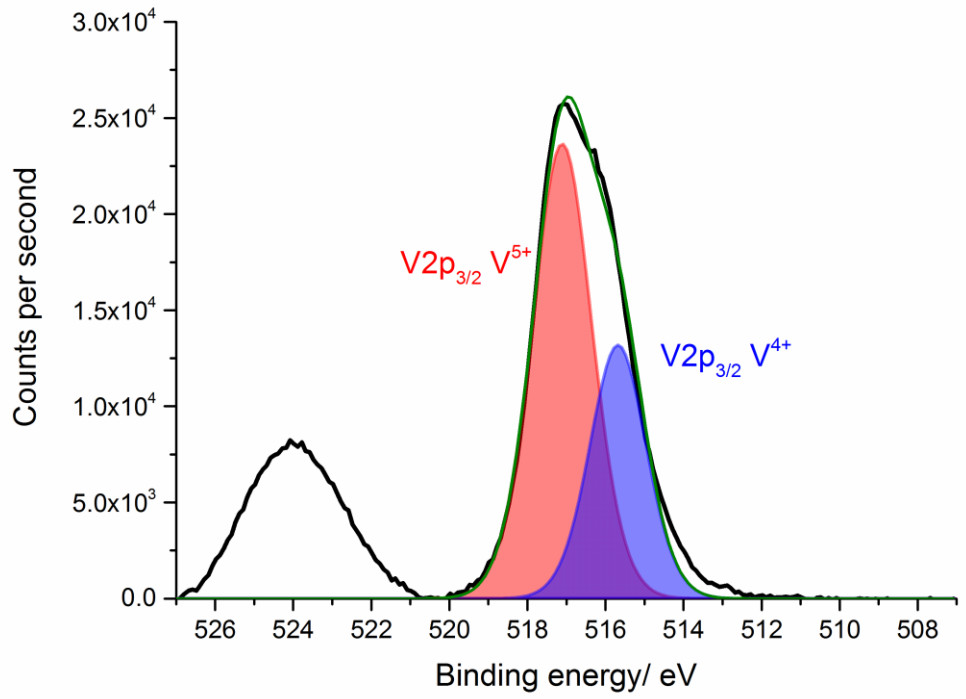

Figure 6.06: Surface XPS spectrum for vanadium binding energy from Nb-VO_2 nanoparticles, sample Nb(15%) VO_2, synthesised by CHFS process.

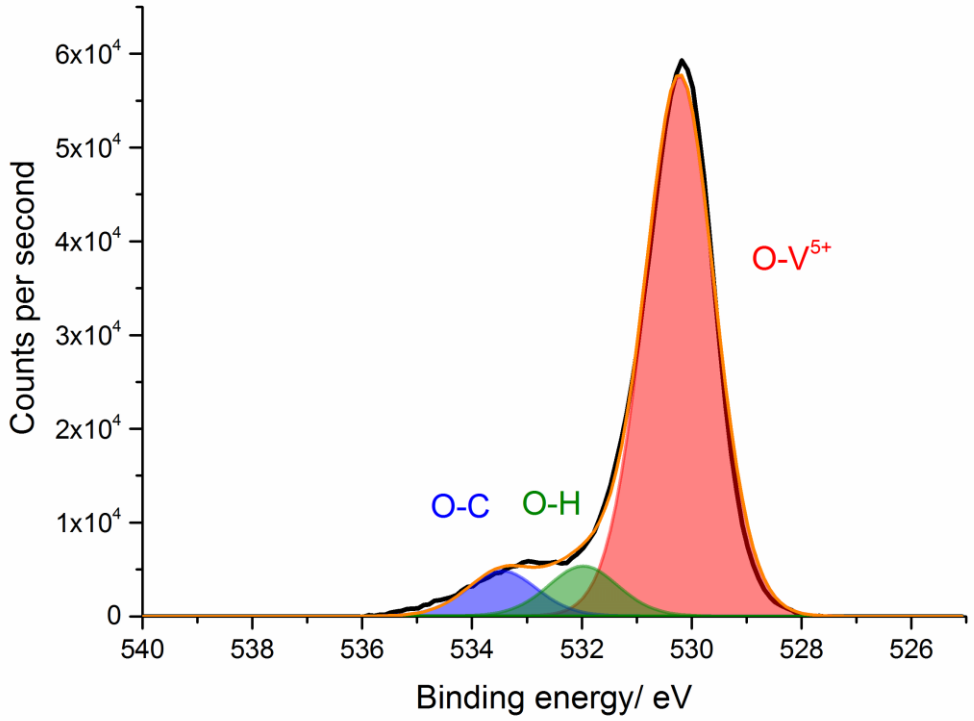

Figure 6.07: Surface XPS spectrum for oxygen binding energy from undoped VO_2 nanoparticles, sample VO_2, synthesised from CHFS process.

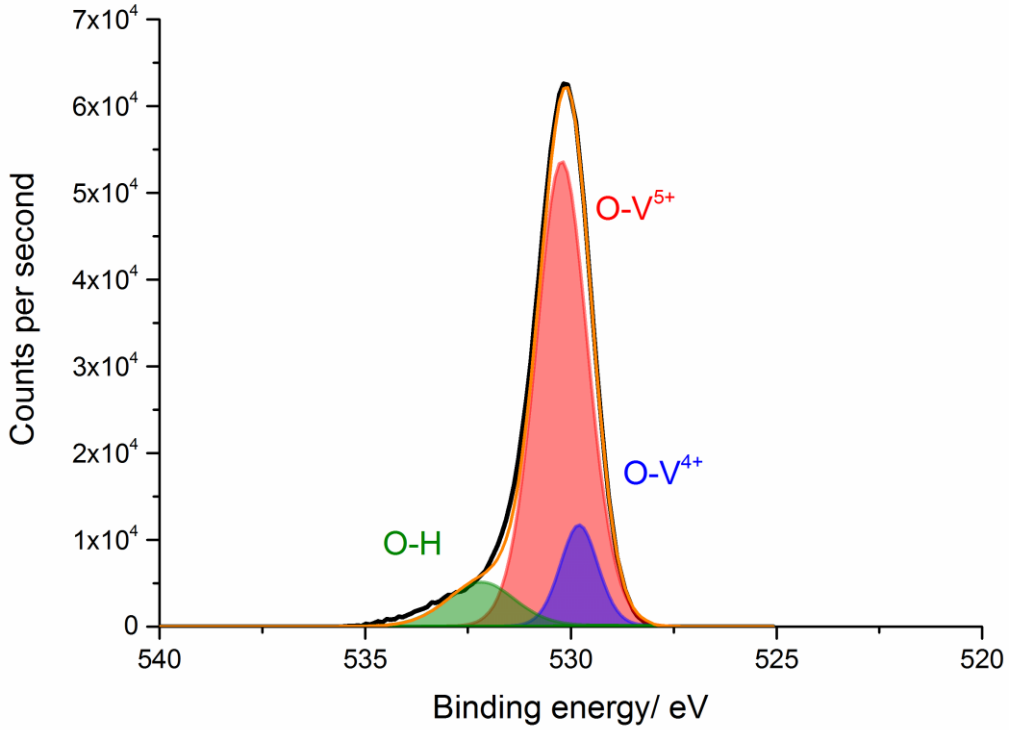

Figure 6.08: Surface XPS spectrum for oxygen binding energy from Nb-VO_2 nanoparticles, sample Nb(15%) VO_2, synthesised by CHFS process.

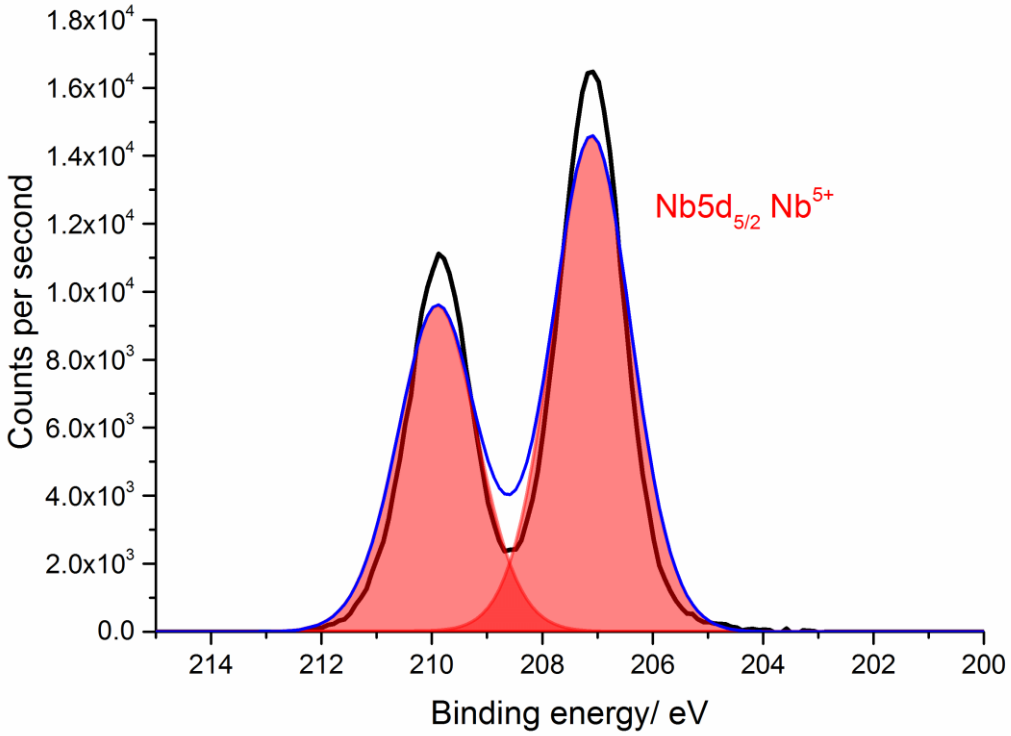

Figure 6.09: Surface XPS spectrum for niobium binding energy from Nb-VO_2 nanoparticles, sample Nb(15%) VO_2, synthesised by CHFS process.

6.3.1.4 Thermochromic properties of Nb-VO_2 nanoparticles

Variable temperature UV/Vis/NIR spectra were obtained to determine the thermochromic properties of the post-annealed Nb-VO_2 samples. Samples were coated onto glass slides. In a typical coating 0.1 g of powder would be mixed with high vacuum grease, the resulting paste would be spread onto a glass slide. This allowed transmission spectra to be obtained, as with the previous transmission spectra, the expected result if the material is thermochromic is a reduction in the transmission, at near IR wavelengths, as the temperature is increased.[7]

All samples showed a reversible switch between the hot and cold spectra, a representative spectrum is given in Figure 6.10 (a). As the inclusion of niobium should reduce the MST phase transition temperature, a series of spectra were recorded at varying temperatures. To determine the MST phase transition temperature, the transmission modulation at 2000 nm was recorded for the samples, Figure 6.10 (b). These plots were fitted using a Boltzmann function equation, 6.01.

$$f(x) = [(A_1-A_2)/(1+e^{(x-x0/dx)})]+A_2 \qquad (6.01)$$

Where A_1 and A_2 are initial and final values (f(x)= A_1 and f(x)= A_2 tangent lines, respectively); in this case, the transmittance modulation corresponds to $(A_1–A_2)\times100$ (%) and x_0 is the abscissa component at the centre of the function, equivalent to the MST temperature.

It can be seen, from Figure 6.10 (b), that samples Nb(5%) VO_2 and Nb(15%) VO_2 both show a reduced phase transition temperature when compared to the undoped VO_2 sample. The phase transitions of all the samples is staggered, except for sample Nb(1%) VO_2, which clearly displays an abrupt change in transmission at ~68 °C. Interestingly, the undoped VO_2 sample shows a wider hysteresis than Nb(1%) VO_2, it has been suggested that nanoparticles can display increased hysteresis in phase transitions due to the presence of defects, such as oxygen vacancies, which allows the relieve of localised stress.[188]

Comparing samples Nb(5%) VO_2 and Nb(15%) VO_2 shows that there is very little difference in the MST phase transition temperature, with both samples switching ~50 °C. This suggests that the niobium is only partially soluble in the VO_2 lattice, with higher concentrations leading to the formation of Nb_2O_5 phases rather than doped VO_2 structures. The reduction in the MST value was also close to what has been observed when Nb has been doped into VO_2 by CVD methods.[31, 43]

It was also reported in studies into Nb-VO_2 thin films that the doping of Nb resulted in the narrowing of the hysteresis loop. To determine whether the Nb-doped VO_2 nanoparticles also displayed this behaviour, hysteresis data were plotted, Figure 6.11. The hysteresis for the undoped sample is ~10 °C, whereas for the 5% Nb sample this narrows to ~5 °C. This supports the conclusion that doping of niobium can both lower the phase transition temperature and reduce the hysteresis between the monoclinic to tetragonal phase transition.[31, 43]

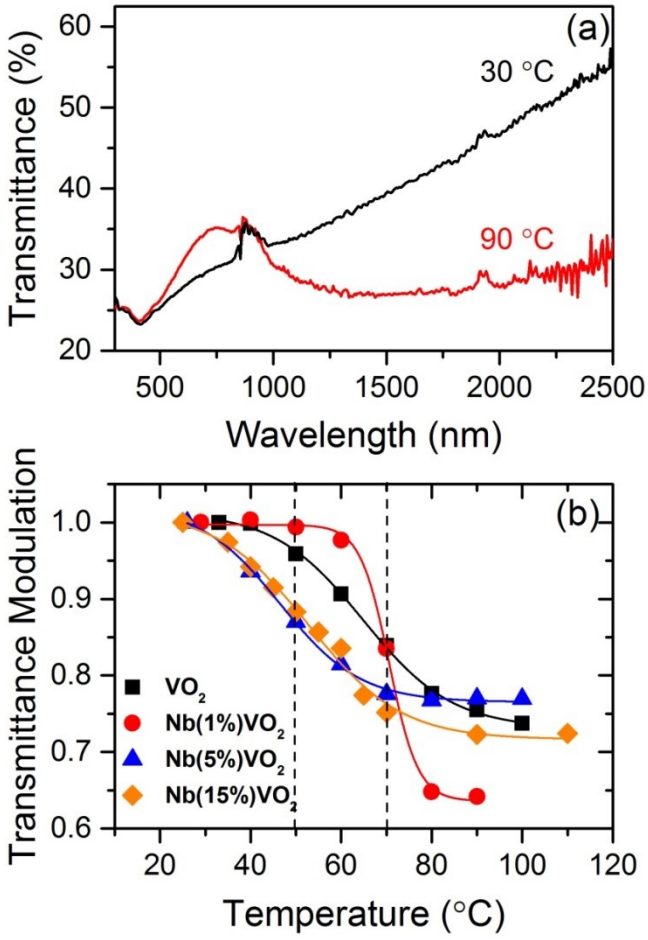

Figure 6.10: The thermochromic properties of the Nb-VO_2 samples were tested by variable temperature UV/Vis spectroscopy, **a)** Representative cold (30 °C, black line) and hot (90°C, red line) UV/Vis spectra (sample Nb(1%) VO_2 shown and **b)** Transmittance modulation (normalised) at 2000 nm for the undoped and Nb-doped VO_2 samples studied in this work, as indicated. The experimental data was fitted using the Boltzmann function. The dashed vertical lines indicate the approximate centre of the corresponding Boltzmann functions.

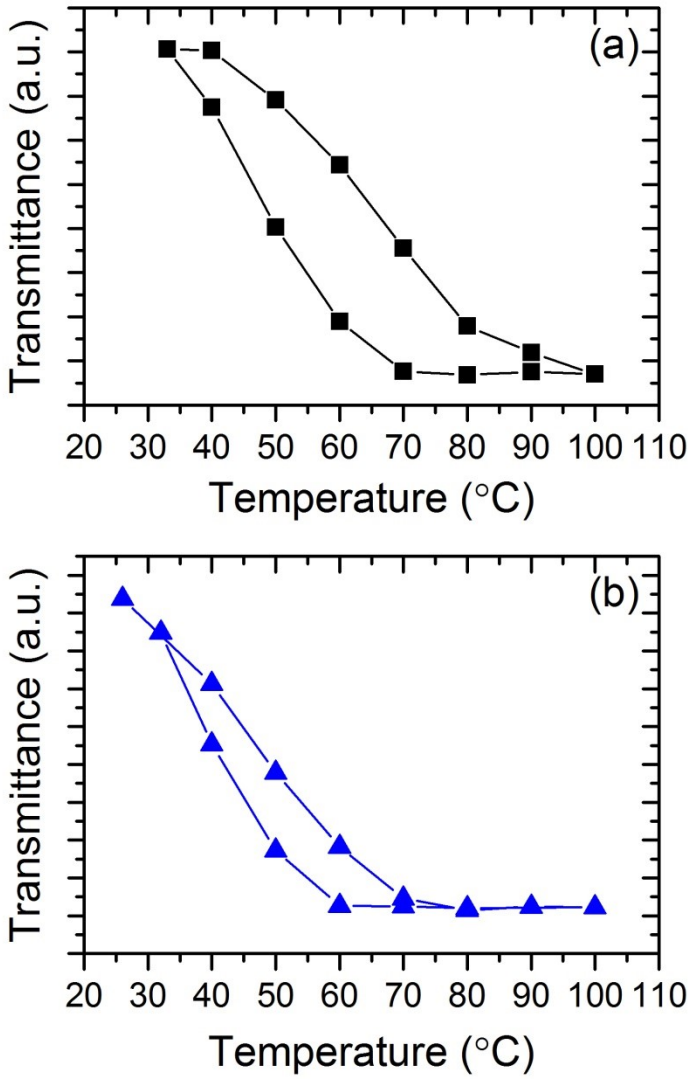

Figure 6.11: Hysteresis for **a)** undoped VO_2 nanoparticles, sample VO_2 and **b)** Nb-doped VO_2 nanoparticles, sample Nb(5%) VO_2.

Previous reports into the production of doped VO_2 nanoparticles have shown that the ability to produce both a decrease in the MST,[147, 192] narrowing of the hysteresis characteristics[121] and reduction in the particle size[26] are all important for thermochromic applications. Although sample Nb(15%) VO_2 did not show any greater reduction in the MST than Nb(5%) VO_2, it did show a significant decrease in the particle size, by a factor of 10 when compared with the undoped VO_2 particles. It could be possible to co-dope niobium with another metal ion, such as tungsten, to both reduce the particle size, MST and hysteresis characteristics of the nanoparticles. The doping of the nanoparticles, described in this chapter, have confirmed previous reports that doping can affect the nature of the nanoparticles formed in continuous hydrothermal processes.[290]

6.4 Conclusions

This chapter has reported on the synthesis of niobium doped VO_2 nanoparticles by a continuous hydrothermal method. A series of Nb-VO_2 particles were synthesised, with the Nb dopant level being varied by changing the concentration of the Nb precursor with respect to the vanadium. The as deposited samples were not phase pure monoclinic VO_2, and a post-annealing step was required to ensure phase pure monoclinic VO_2. The post-annealed samples all showed diffraction peaks consistent with monoclinic VO_2, however the higher concentrations of niobium resulted in additional peaks in the XRD pattern which were attributed to the formation of a niobate phase.

The particle sizes were shown to vary widely depending on the niobium content, with low Nb doping resulting in larger particles and the highest Nb doping resulting in a significant decrease in the particle size. The morphology of the particles were also dependent on the niobium content, with undoped and 1% doped particles showing spherical and rod-like formation, 5% doped particles showing spherical and 'blade' like formations and 15% doped particles displaying only spherical particle shapes. This is attributed to the niobium acting as a 'seed' in the reaction, with greater niobium content resulting in faster nucleation rates and smaller particle sizes.

The niobium was also shown to reduce the MST phase transition, to ~50 °C, but only at higher doping levels. There was no change in the MST between the 5% and 15% Nb doping, which was attributed to the formation of N_2O_5 in the 15% Nb sample.

This is the first time that the doping of VO_2 has been shown by a continuous hydrothermal process. This has shown that the CHFS process is a versatile way of producing thermochromic nanoparticles on a large scale and to control the properties of the nanoparticles by doping. There is still further work required to determine the effect of pH, surfactants, doping and co-doping can have on the VO_2 system. Currently, monoclinic VO_2 cannot be directly synthesised from a continuous hydrothermal process.

Chapter 7

Conclusions and considerations for future work

Chapter 7: Conclusions and considerations for future work

7.1 Overall conclusions

This thesis has examined the use of VO_2 thin films and nanoparticles for solar modulation coatings. Two synthesis techniques, APCVD and CHFS were used to synthesise thin films and nanoparticles of monoclinic VO_2. Monoclinic VO_2 is a material with the potential to allow the control over building heat loads without the need to use air-conditioning, thus helping to reduce emissions and limit anthropogenic induced climate change. Further to this, a new FBCVD reactor was designed and built for the project, this was with the idea of depositing VO_2 onto powder substrates. This was, however, unsuccessful, so a demonstration of the technique shown by the deposition of TiO_2 single and multi-layers onto powder substrates.

For the APCVD reactions, the reaction between vanadium (IV) chloride and ethyl acetate was demonstrated for the first time. Thin films of monoclinic VO_2 were successfully grown from the above reaction at deposition temperatures above 450 °C. The best performing films, in terms of solar modulation, were deposited at 550 °C. The effect of deposition time on the thermochromic response was determined, with thin films between 50-300 nm showing the same solar modulation when evaluated using weighted solar modulation values. Films of 900 nm showed the largest response ~15% solar modulation, but suffered from poor visible light transmission as a result of the dark brown colour of the thicker VO_2 deposition. The growth rate of the films was characteristic of a Stranski-Krastanov mechanism, with thinnest depositions showing a mix of island and layer type formation. Interestingly, the 300 nm film (1 min deposition) showed an extremely rough and disordered surface, whilst the 900 nm (3 min deposition) showed much greater order but were still extremely rough.

The second VO_2 system demonstrated by APCVD was the deposition of multi-layered $VO_2/SiO_2/TiO_2$. This was the first time that such a multi-layered system has been demonstrated by CVD. The multi-layered films showed both improved solar modulation and visible light transmission when compared to single VO_2 film analogues. The improved visible light transmission was attributed to a decrease in the haziness of the films, when assessed by a visual inspection, most likely due to the refractive properties of the SiO_2 ‘sandwich’ layer. The morphology of the SiO_2 layer was shown to be highly porous, with a pillar/column like structure evident

between the pores in the structure. Modelling of this SiO_2 layer suggested that the porous nature of the layer gave the improved visible light scattering when compared to a uniform SiO_2 layer with bulk like optical characteristics. The TiO_2 layer showed rutile TiO_2 in the thinner multi-layer and a mix of anatase/rutile in the thicker multi-layered film. The thicker of the multi-layered systems was shown to have self-cleaning properties by the photocatalytic destruction of a layer of stearic acid. This is a first demonstration of a multi-layered, multi-functional film with improved thermochromic properties and visible light transmission from APCVD- an industrially scalable synthesis technique.

A lab-scale FBCVD reactor was designed and built especially for the project, due to time constraints however, a demonstration of the technique was achieved by a case study of the deposition of single and multi-layered systems onto powder substrates. The material chosen to show this was TiO_2, as it is a material that is easy to characterise and has two primary phases, rutile and anatase, which allowed for the deposition and analysis of these multi-shelled systems. XRD, Raman and UV/Vis spectroscopy confirmed that the two phases could be made independently as well as mixed and finally in a multi-shelled system. TEM images showed that the presence of multi-shelled structures in the anatase@rutile multi-shelled system. The photocatalytic properties of the samples were determined by photocatalytic destruction of stearic acid, under UV (365 nm) irradiation, with the multi-shelled system being poorer than pure anatase, this was attributed to the rutile component being inaccessible and so acting as a charge recombination centre. This evidence was further supported by BET analysis, which showed that the samples had very low surface areas. Combined with the other forms of analysis, this shows that the FBCVD gives excellent surface coverage of materials.

CHFS was used to produce VO_2 nanoparticles for the first time. The effect of residence time in the reactor and reaction (mixing) temperature were measured, with increasing reaction temperature leading to nanoparticles that more closely matched standard XRD patterns. The as formed VO_2 nanoparticles required a post-annealing step to ensure phase pure monoclinic VO_2. Two distinct types of morphology were observed within the VO_2 samples, rods and spheres. It was determined that the rods grew at low temperatures, with spheres being favoured at higher temperatures. The rods also did not appear in the shortest residence times, suggesting that the rod like structures grew from the spheres. The post annealed VO_2 nanoparticles were shown to have a good thermochromic response, with the

sample produced at the highest reaction temperature showing the largest thermochromic switch.

Doping studies were also performed on the CHFS, with the effect of Nb concentration on the phase and morphology of the nanoparticles investigated. At high Nb concentrations, it was found that new phases were present in the XRD patterns- these were attributed to the segregation of the niobium at high concentrations, forming a niobate phase. The niobium also had an effect on the nanoparticle size and morphology, with the highest concentrations of Nb retarding nanoparticle growth resulting in a significant decrease in particle size. XPS analysis showed that the Nb went in as 5+ in all samples. Interestingly, the increase in Nb content was matched by a decrease in the proportion of V^{5+} present in the samples, suggesting that the niobium is reducing the vanadium centres when it is incorporated into the VO_2 nanoparticles. All samples showed a thermochromic switch, with the niobium decreasing the MST phase transition to ~50 °C, however above 5% Nb doping there was no additional decrease. These CHFS reactions were able to show that it is possible to produce undoped and doped VO_2 nanoparticles by a high-throughput industrially scalable synthetic process, however, pure phase monoclinic VO_2 has yet to be synthesised directly.

7.2 Considerations for future work

The multi-layered VO_2 systems discussed in this thesis are only a demonstration of the ability to produce such structures from APCVD conditions; as such there are many potential areas to explore. The first of these would come from attempting to synthesise the ideal film thicknesses suggested by the modelling of the multi-layered systems. This would involve the deposition of a thin (<50 nm) layer of VO_2 followed by SiO_2 and TiO_2 to attempt to improve the visible light transmission to ~70-80% whilst maintaining a solar modulation of ~5%. The next step beyond this would be to produce a stacked system, so 2 or 3 layers of VO_2 would be 'sandwiched' between alternating layers of SiO_2, this would then be analysed to see whether the visible light transmission can be kept at ~70-80% with an improvement on the solar modulation to ~10%. Further studies could be conducted with the use of differing dielectric layers, such as ZrO_2, to determine how the refractive index of the material can be altered- this can either come from modelling the system prior to depositions or as with the work presented in this thesis, depositing a sample structure first and then modelling to determine the ideal thickness of each layer of the structure.

The FBCVD reactor has many potential applications, as this thesis has demonstrated, the FBCVD system is ideal for the deposition of multi-shelled structures. The next set of experiments on this system would be to deposit a series of multi-shelled structures, such as WO_3/TiO_2, CuO/TiO_2 and CdS/TiO_2, to determine the properties of structures deposited onto powder substrates by CVD methods. Beyond this, the use of organic templates that can be calcined to leave a desired material and morphology will be investigated- such as depositing onto carbon substrates with TiO_2, calcining to remove the carbon framework and then analysing the resultant product. If successful, this would allow for the production of materials with novel architectures from an industrially scalable and high-throughput method.

CHFS has many potential applications for VO_2 materials. The first set of experiments would be towards the direct synthesis of monoclinic VO_2 nanoparticles. The CHFS reactor is currently being outfitted with a long residence time pipe that will allow up to 120 s residence time, combined with the highest temperature (375 °C) this may afford monoclinic VO_2. The use of templates, such as TiO_2, will also be employed to determine if a lowering of the barrier to monoclinic VO_2 can be achieved within the CHFS reactor. Finally, core-shell structures could also be produced from the CHFS- this will allow for the altering of the visible light characteristics of the material by using SiO_2, ZrO_2 or TiO_2 as the shell structure to alter the refractive index of the nanoparticles- diminishing the absorption of visible wavelengths by the VO_2 core, whilst maintaining the thermochromic properties.

References

1. S. M. Babulanam, T. S. Eriksson, G. A. Niklasson and C. G. Granqvist, *Sol. Energy Mater.*, 1987, 16, 347-363.
2. J. B. Goodenough, *Annu. Rev. Mater. Sci.*, 1971, 1, 101-138.
3. D. C. Crans and A. S. Tracey, *ChemInform*, 1999, 30.
4. J. M. Reyes, S. L. Segel and M. Sayer, *Can. J. Phys.*, 1976, 54, 1-8.
5. Y. Oka, T. Ohtani, N. Yamamoto and T. Takada, *Nippon seramikkusu kyokai gakujutsu ronbunshi*, 1989, 97, 1134-1137.
6. L. Mai, Q. Wei, Q. An, X. Tian, Y. Zhao, X. Xu, L. Xu, L. Chang and Q. Zhang, *Advanced Materials*, 2013, 25, 2969-2973.
7. J. B. Goodenough, *Journal of Solid State Chemistry*, 1971, 3, 490-500.
8. C. Nethravathi, C. R. Rajamathi, M. Rajamathi, U. K. Gautam, X. Wang, D. Golberg and Y. Bando, *Acs Applied Materials & Interfaces*, 2013, 5, 2708-2714.
9. C. Batista, J. Carneiro, R. M. Ribeiro and V. Teixeira, *J. Nanosci. Nanotechnol.*, 2011, 11, 9042-9045.
10. C. Piccirillo, R. Binions and I. P. Parkin, *Chem. Vap. Deposition*, 2007, 13, 145-151.
11. WO2008009967A1, 2008.
12. D. D. Eden, *Proc. Soc. Photo-Opt. Instrum. Eng.*, 1979, 185, 97-102.
13. Y. Zhou, X. Chen, C. Ko, Z. Yang, C. Mouli and S. Ramanathan, *IEEE Electron Device Lett.*, 2013, 34, 220-222.
14. S. Wall, L. Foglia, D. Wegkamp, K. Appavoo, J. Nag, R. F. Haglund, J. Stähler and M. Wolf, *Physical Review B*, 2013, 87, 115126.
15. W. W. Peng, G. Niu, R. Tetot, B. Vilquin, F. Raimondi, J. B. Brubach, E. Amzallag, T. Yanagida, S. Autier-Laurent, P. Lecoeur and P. Roy, *J. Phys.: Condens. Matter*, 2013, 25, 445402, 445407 pp.
16. T. D. Manning, I. P. Parkin, R. J. H. Clark, D. Sheel, M. E. Pemble and D. Vernadou, *J. Mater. Chem.*, 2002, 12, 2936-2939.
17. R. Binions, 2012.
18. I. P. Parkin, R. Binions, C. Piccirillo, C. S. Blackman and T. D. Manning, *Journal of Nano research*, 2008, 2, 1-20.
19. U.-S. Buildings and C. Initiative, Paris: United Nations Environment Programme, 2007.
20. K. Dovidenko, S. Beasor, A. Topol, H. Efstathiadis, S. Oktyabrsky, S. Shokhor, S. Naar and A. E. Kaloyeros, *Mater. Res. Soc. Symp. Proc.*, 2001, 654, AA3.42/41-AA43.42/46.
21. E. Kusano, J. A. Theil and J. A. Thornton, *J. Vac. Sci. Technol., A*, 1988, 6, 1663-1667.
22. X. Y. Zhang, M. J. Chao, E. J. Liang, F. Hu and B. Yuan, *Journal of Inorganic Materials*, 2009, 24, 34-38.
23. L. Q. Mai, B. Hu, T. Hu, W. Chen and E. D. Gu, *Journal of Physical Chemistry B*, 2006, 110, 19083-19086.
24. E. Cavanna, J. P. Segaud and J. Livage, *Materials Research Bulletin*, 1999, 34, 167-177.
25. M. Pan, H. Zhong, S. Wang, J. Liu, Z. Li, X. Chen and W. Lu, *J. Cryst. Growth*, 2004, 265, 121-126.
26. Y. Gao, C. Cao, L. Dai, H. Luo, M. Kanehira, Y. Ding and Z. L. Wang, *Energy Environ. Sci.*, 2012, 5, 8708-8715.
27. S. Ji, F. Zhang and P. Jin, *Sol. Energy Mater. Sol. Cells*, 2011, 95, 3520-3526.
28. R. Li, S. Ji, Y. Li, Y. Gao, H. Luo and P. Jin, *Mater. Lett.*, 2013, 110, 241-244.

29. J.-H. Son, J. Wei, D. Cobden, G. Cao and Y. Xia, *Chemistry of Materials*, 2010, 22, 3043-3050.
30. J. Zhou, Y. Gao, X. Liu, Z. Chen, L. Dai, C. Cao, H. Luo, M. Kanahira, C. Sun and L. Yan, *Phys. Chem. Chem. Phys.*, 2013, 15, 7505-7511.
31. T. D. Manning, I. P. Parkin, C. Blackman and U. Qureshi, *J. Mater. Chem.*, 2005, 15, 4560-4566.
32. T. D. Manning, I. P. Parkin, M. E. Pemble, D. Sheel and D. Vernardou, *Chem. Mater.*, 2004, 16, 744-749.
33. C. Piccirillo, R. Binions and I. P. Parkin, *Thin Solid Films*, 2008, 516, 1992-1997.
34. K. L. Choy, *Prog. Mater. Sci.*, 2003, 48, 57-170.
35. R. G. Gordon, *MRS bulletin*, 2000, 25, 52-57.
36. G. Ozaydin-Ince, A. M. Coclite and K. K. Gleason, *Reports on Progress in Physics*, 2012, 75, 016501.
37. M. Wang, S. K. Jang, W. J. Jang, M. Kim, S. Y. Park, S. W. Kim, S. J. Kahng, J. Y. Choi, R. S. Ruoff and Y. J. Song, *Advanced Materials*, 2013, 25, 2746-2752.
38. D. J. Larkin, P. G. Neudeck, J. A. Powell and L. G. Matus, *Applied physics letters*, 1994, 65, 1659-1661.
39. I. Kartsonakis, N. Papadopoulos and C. Karayianni, *Key Engineering Materials*, 2012, 495, 138-141.
40. T. S. Sudarshan, 2004.
41. N. Voudouris, C. Christoglou and G. Angelopoulos, *Surface and Coatings Technology*, 2001, 141, 275-282.
42. V. Diesen, C. W. Dunnill, J. C. Bear, S. Firth, M. Jonsson and I. P. Parkin, *Chemical Vapor Deposition*, 2014, 20, 91-97.
43. C. Piccirillo, R. Binions and I. P. Parkin, *Eur. J. Inorg. Chem.*, 2007, 4050-4055.
44. A. A. Tahir, T. Peiris and K. Wijayantha, *Chemical Vapor Deposition*, 2012, 18, 107-111.
45. X. Li, C. W. Magnuson, A. Venugopal, R. M. Tromp, J. B. Hannon, E. M. Vogel, L. Colombo and R. S. Ruoff, *Journal of the American Chemical Society*, 2011, 133, 2816-2819.
46. S. Fay, U. Kroll, C. Bucher, E. Vallat-Sauvain and A. Shah, *Solar Energy Materials and Solar Cells*, 2005, 86, 385-397.
47. K. Haga, T. Suzuki, Y. Kashiwaba, H. Watanabe, B. Zhang and Y. Segawa, *Thin Solid Films*, 2003, 433, 131-134.
48. J. Ayllon, A. Figueras, S. Garelik, L. Spirkova, J. Durand and L. Cot, *Journal of materials science letters*, 1999, 18, 1319-1321.
49. P. Hájková, P. Špatenka, J. Krumeich, P. Exnar, A. Kolouch, J. Matoušek and P. Kočí, *The European Physical Journal D-Atomic, Molecular, Optical and Plasma Physics*, 2009, 54, 189-193.
50. Y. Lin, Y. Yang, B. Zhuang, S. Huang, L. Wu, Z. Huang, F. Zhang and Y. Du, *Journal of Physics D: Applied Physics*, 2008, 41, 195007.
51. A. Kafizas, C. W. Dunnill and I. P. Parkin, *J. Mater. Chem.*, 2010, 20, 8336-8349.
52. D. Vernardou, M. E. Pemble and D. W. Sheel, *Thin Solid Films*, 2007, 515, 8768-8770.
53. P. Evans and D. W. Sheel, *Surf. Coat. Technol.*, 2007, 201, 9319-9324.
54. A. Anastassiou, C. Christoglou and G. Angelopoulos, *Surface and Coatings Technology*, 2010, 204, 2240-2245.
55. J. H. Park, S. Y. Lee, D. H. Bae, N. Y. Lim and J. W. Ha, 2006.
56. C. Vahlas, B. Caussat, P. Serp and G. N. Angelopoulos, *Mater. Sci. Eng., R*, 2006, R53, 1-72.
57. T. D. Manning and I. P. Parkin, *J. Mater. Chem.*, 2004, 14, 2554-2559.

58. T. D. Manning and I. P. Parkin, *Polyhedron*, 2004, 23, 3087-3095.
59. M. E. A. Warwick, I. Ridley and R. Binions, *J. Nanosci. Nanotechnol.*, 2011, 11, 8158-8162.
60. M. E. A. Warwick, C. W. Dunnill and R. Binions, *Chem. Vap. Deposition*, 2010, 16, 220-224.
61. M. E. A. Warwick and R. Binions, *J. Nanosci. Nanotechnol.*, 2011, 11, 8126-8131.
62. M. L. Hitchman and K. F. Jensen, *Chemical vapor deposition: principles and applications*, Academic Press London, 1993.
63. M. Ohring, *Materials science of thin films*, Academic press, 2001.
64. M.-J. Ko, D. Kim, W.-J. Kim, M. S. Cho, S. G. Yoon and J. Y. Park, *Journal of the Korean Ceramic Society*, 2013.
65. S. Kinkel, G. Angelopoulos and W. Dahl, *Surface and Coatings Technology*, 1994, 64, 119-125.
66. R. Moene, L. Kramer, J. Schoonman, M. Makkee and J. Moulijn, *Applied Catalysis A: General*, 1997, 162, 181-191.
67. C. Christoglou, N. Voudouris and G. Angelopoulos, *Surface and Coatings Technology*, 2002, 155, 51-58.
68. C. H. See and A. T. Harris, *Ind. Eng. Chem. Res.*, 2007, 46, 997-1012.
69. D. Venegoni, P. Serp, R. Feurer, Y. Kihn, C. Vahlas and P. Kalck, *Carbon*, 2002, 40, 1799-1807.
70. F. Danafar, A. Fakhru'l-Razi, M. A. M. Salleh and D. R. A. Biak, *Chemical Engineering Journal*, 2009, 155, 37-48.
71. A. Morançais, B. Caussat, Y. Kihn, P. Kalck, D. Plee, P. Gaillard, D. Bernard and P. Serp, *Carbon*, 2007, 45, 624-635.
72. D. Geldart, *Powder technology*, 1973, 7, 285-292.
73. A. H. Ye, W. Q. Fan, Q. H. Zhang, W. P. Deng and Y. Wang, *Catalysis Science & Technology*, 2012, 2, 969-978.
74. Y. J. Zhang, Y. C. Wang, W. Yan, T. Li, S. Li and Y. R. Hu, *Applied Surface Science*, 2009, 255, 9508-9511.
75. H. Diker, C. Varlikli, K. Mizrak and A. Dana, *Energy*, 2011, 36, 1243-1254.
76. C. S. Cundy and P. A. Cox, *Chemical Reviews*, 2003, 103, 663-702.
77. D. E. Akporiaye, I. M. Dahl, A. Karlsson and R. Wendelbo, *Angewandte Chemie International Edition*, 1998, 37, 609-611.
78. N. Murayama, H. Yamamoto and J. Shibata, *International Journal of Mineral Processing*, 2002, 64, 1-17.
79. E. Y. Choi, K. Park, C. M. Yang, H. Kim, J. H. Son, S. W. Lee, Y. H. Lee, D. Min and Y. U. Kwon, *Chemistry-a European Journal*, 2004, 10, 5535-5540.
80. F. A. A. Paz and J. Klinowski, *Chemical Communications*, 2003, 1484-1485.
81. Y. K. Hwang, D. Y. Hong, J. S. Chang, S. H. Jhung, Y. K. Seo, J. Kim, A. Vimont, M. Daturi, C. Serre and G. Férey, *Angewandte Chemie International Edition*, 2008, 47, 4144-4148.
82. F. Tao, Z. Wang, L. Yao, W. Cai and X. Li, *Nanotechnology*, 2006, 17, 1079.
83. J. Wan, X. Chen, Z. Wang, X. Yang and Y. Qian, *Journal of Crystal Growth*, 2005, 276, 571-576.
84. D. Zhao, Q. Huo, J. Feng, B. F. Chmelka and G. D. Stucky, *Journal of the American Chemical Society*, 1998, 120, 6024-6036.
85. D. Kuang, A. Xu, Y. Fang, H. Liu, C. Frommen and D. Fenske, *Advanced Materials*, 2003, 15, 1747-1750.
86. T. Adschiri, K. Kanazawa and K. Arai, *Journal of the American Ceramic Society*, 1992, 75, 1019-1022.
87. A. Cabanas and M. Poliakoff, *Journal of Materials Chemistry*, 2001, 11, 1408-1416.
88. C. J. Tighe, R. I. Gruar, C. Y. Ma, T. Mahmud, X. Z. Wang and J. A. Darr, *The Journal of Supercritical Fluids*, 2012, 62, 165-172.

89. X. Liu, C. Huang, S. Yi, G. Xie, H. Li and Y. Luo, *Solid State Commun.*, 2007, 144, 259-263.
90. D. Munoz-Rojas and E. Baudrin, *Solid State Ionics*, 2007, 178, 1268-1273.
91. V. K. L. Mer, *Industrial & Engineering Chemistry*, 1952, 44, 1270-1277.
92. P. W. Voorhees, *Journal of Statistical Physics*, 1985, 38, 231-252.
93. Y. De Smet, L. Deriemaeker and R. Finsy, *Langmuir*, 1997, 13, 6884-6888.
94. A. Sahraneshin, S. Asahina, T. Togashi, V. Singh, S. Takami, D. Hojo, T. Arita, K. Minami and T. Adschiri, *Crystal Growth & Design*, 2012, 12, 5219-5226.
95. K. Cassiers, T. Linssen, M. Mathieu, M. Benjelloun, K. Schrijnemakers, P. Van Der Voort, P. Cool and E. Vansant, *Chemistry of Materials*, 2002, 14, 2317-2324.
96. G. Amin, M. Asif, A. Zainelabdin, S. Zaman, O. Nur and M. Willander, *Journal of Nanomaterials*, 2011, 2011, 5.
97. Z. Yanqing, S. Erwei, C. Zhizhan, L. Wenjun and H. Xingfang, *J. Mater. Chem.*, 2001, 11, 1547-1551.
98. C.-H. Lu and C.-H. Yeh, *Ceramics International*, 2000, 26, 351-357.
99. J. Yu, G. Wang, B. Cheng and M. Zhou, *Applied Catalysis B: Environmental*, 2007, 69, 171-180.
100. C.-Y. Huang, Y.-C. Hsu, J.-G. Chen, V. Suryanarayanan, K.-M. Lee and K.-C. Ho, *Solar Energy Materials and Solar Cells*, 2006, 90, 2391-2397.
101. C. Pan, D. Zhang and L. Shi, *Journal of Solid State Chemistry*, 2008, 181, 1298-1306.
102. G. Büchel, M. Grün, K. K. Unger, A. Matsumoto and T. Kazuo, *Supramolecular Science*, 1998, 5, 253-259.
103. C.-C. Chang, H.-L. Wu, C.-H. Kuo and M. H. Huang, *Chemistry of Materials*, 2008, 20, 7570-7574.
104. Y. Hakuta, S. Onai, H. Terayama, T. Adschiri and K. Arai, *Journal of materials science letters*, 1998, 17, 1211-1213.
105. C. Kaya, J. He, X. Gu and E. Butler, *Microporous and Mesoporous Materials*, 2002, 54, 37-49.
106. W. K. Ho, J. C. Yu and S. C. Lee, *Journal of Solid State Chemistry*, 2006, 179, 1171-1176.
107. G. S. Wu, J. P. Wang, D. F. Thomas and A. C. Chen, *Langmuir*, 2008, 24, 3503-3509.
108. J. Nag and R. F. Haglund, Jr., *J. Phys.: Condens. Matter*, 2008, 20, 264016/264011-264016/264014.
109. C. B. Greenberg, *Thin Solid Films*, 1983, 110, 73-82.
110. C. D. E. Lakeman and D. A. Payne, *Mater. Chem. Phys.*, 1994, 38, 305-324.
111. K. R. Speck, H. S. W. Hu, M. E. Sherwin and R. S. Potember, *Thin Solid Films*, 1988, 165, 317-322.
112. V. Keppens, D. Mandrus and L. A. Boatner, *Mater. Res. Soc. Symp. Proc.*, 1998, 495, 439-444.
113. D. Yin, N. Xu, J. Zhang and X. Zheng, *Mater. Res. Bull.*, 1996, 31, 335-340.
114. T. J. Hanlon, J. A. Coath and M. A. Richardson, *Thin Solid Films*, 2003, 436, 269-272.
115. D. P. Partlow, S. R. Gurkovich, K. C. Radford and L. J. Denes, *J. Appl. Phys.*, 1991, 70, 443-452.
116. C. Huang, L. Chen, G. Xu and L. Miao, *J. Sol-Gel Sci. Technol.*, 2012, 63, 103-107.
117. Z. Peng, W. Jiang and H. Liu, *Journal of Physical Chemistry C*, 2007, 111, 1119-1122.
118. A. Zylbersztejn and N. F. Mott, *Phys. Rev. B*, 1975, 11, 4383-4395.
119. C. Batista, V. Teixeira and R. M. Ribeiro, *J. Nanosci. Nanotechnol.*, 2010, 10, 1393-1397.

120. E. Wieser, W. Brueckner, B. Thuss and U. Gerlach, *Phys. Status Solidi A*, 1978, 45, 123-131.
121. J. Du, Y. Gao, H. Luo, L. Kang, Z. Zhang, Z. Chen and C. Cao, *Sol. Energy Mater. Sol. Cells*, 2011, 95, 469-475.
122. M. Nishikawa, T. Nakajima, T. Kumagai, T. Okutani and T. Tsuchiya, *Jpn. J. Appl. Phys.*, 2011, 50, 01BE04/01-01BE04/05.
123. K. G. West, J. Lu, L. He, D. Kirkwood, W. Chen, T. P. Adl, M. S. Osofsky, S. B. Qadri, R. Hull and S. A. Wolf, *J. Supercond. Novel Magn.*, 2008, 21, 87-92.
124. P. Kiri, M. E. A. Warwick, I. Ridley and R. Binions, *Thin Solid Films*, 2011, 520, 1363-1366.
125. N. Mlyuka, G. Niklasson and C.-G. Granqvist, *Applied physics letters*, 2009, 95, 171909-171909-171903.
126. C. Tang, P. Georgopoulos, M. E. Fine, J. B. Cohen, M. Nygren, G. S. Knapp and A. Aldred, *Phys. Rev. B: Condens. Matter*, 1985, 31, 1000-1011.
127. A. Gentle and G. B. Smith, *J. Phys. D: Appl. Phys.*, 2008, 41, 015402/015401-015402/015405.
128. W. Burkhardt, T. Christmann, B. K. Meyer, W. Niessner, D. Schalch and A. Scharmann, *Thin Solid Films*, 1999, 345, 229-235.
129. M. Soltani, M. Chaker, E. Haddad, R. Kruzelecky and J. Margot, *Applied physics letters*, 2004, 85, 1958.
130. I. Takahashi, M. Hibino and T. Kudo, *Jpn. J. Appl. Phys., Part 1*, 2001, 40, 1391-1395.
131. A. Rougier, A. Blyr and A. Quede, *J. Electrochem. Soc.*, 2001, 148, H7-H12.
132. W. Burkhardt, T. Christmann, S. Franke, W. Kriegseis, D. Meister, B. K. Meyer, W. Niessner, D. Schalch and A. Scharmann, *Thin Solid Films*, 2002, 402, 226-231.
133. S. Y. Li, G. A. Niklasson and C. G. Granqvist, *Annu. Tech. Conf. Proc. - Soc. Vac. Coaters*, 2011, 54th, 29-34.
134. S. Y. Li, G. A. Niklasson and C. G. Granqvist, *MRS Online Proc. Libr.*, 2011, 1315, No pp. given.
135. K. Nagashima, T. Yanagida, H. Tanaka and T. Kawai, *J. Appl. Phys.*, 2007, 101, 026103/026101-026103/026103.
136. T. Kikuzuki and M. Lippmaa, *Appl. Phys. Lett.*, 2010, 96, 132107/132101-132107/132103.
137. Y. Muraoka, Y. Ueda and Z. Hiroi, *J. Phys. Chem. Solids*, 2002, 63, 965-967.
138. J. Cao, E. Ertekin, V. Srinivasan, W. Fan, S. Huang, H. Zheng, J. W. L. Yim, D. R. Khanal, D. F. Ogletree, J. C. Grossman and J. Wu, *Nat. Nanotechnol.*, 2009, 4, 732-737.
139. J. M. Gregg and R. M. Bowman, *Appl. Phys. Lett.*, 1997, 71, 3649-3651.
140. B. Hu, Y. Ding, W. Chen, D. Kulkarni, Y. Shen, V. V. Tsukruk and Z. L. Wang, *Adv. Mater. (Weinheim, Ger.)*, 2010, 22, 5134-5139.
141. K. Nagashima, T. Yanagida, H. Tanaka and T. Kawai, *Physical Review B*, 2006, 74, 172106.
142. A. Mills, N. Elliott, I. P. Parkin, S. A. O'Neill and R. J. Clark, *J. Photochem. Photobiol., A*, 2002, 151, 171-179.
143. U. Qureshi, T. D. Manning, C. Blackman and I. P. Parkin, *Polyhedron*, 2006, 25, 334-338.
144. M. Wilkinson, A. Kafizas, S. M. Bawaked, A. Y. Obaid, S. A. Al-Thabaiti, S. N. Basahel, C. J. Carmalt and I. P. Parkin, *ACS Comb. Sci.*, 2013, 15, 309-319.
145. Z. Chen, Y. Gao, L. Kang, J. Du, Z. Zhang, H. Luo, H. Miao and G. Tan, *Sol. Energy Mater. Sol. Cells*, 2011, 95, 2677-2684.
146. CN102241482A, 2011.

147. J. Nag and R. Haglund Jr, *Journal of Physics: Condensed Matter*, 2008, 20, 264016.
148. B. L. Cushing, V. L. Kolesnichenko and C. J. O'Connor, *Chemical Reviews*, 2004, 104, 3893-3946.
149. J. Y. Suh, R. Lopez, L. C. Feldman and R. Haglund Jr, *Journal of Applied Physics*, 2004, 96, 1209-1213.
150. R. Lopez, T. Haynes, L. Boatner, L. Feldman and R. Haglund, *PHYSICAL REVIEW-SERIES B-*, 2002, 65, 224113-224113.
151. C. G. Granqvist, P. C. Lansaker, N. R. Mlyuka, G. A. Niklasson and E. Avendano, *Sol. Energy Mater. Sol. Cells*, 2009, 93, 2032-2039.
152. S. Y. Li, G. A. Niklasson and C. G. Granqvist, *J. Appl. Phys.*, 2010, 108, 063525/063521-063525/063528.
153. S. Y. Li, G. A. Niklasson and C. G. Granqvist, *J. Appl. Phys.*, 2011, 109, 113515/113511-113515/113515.
154. K. Appavoo, D. Y. Lei, Y. Sonnefraud, B. Wang, S. T. Pantelides, S. A. Maier and R. F. Haglund, Jr., *Nano Lett.*, 2012, 12, 780-786.
155. Y. Gao, S. Wang, H. Luo, L. Dai, C. Cao, Y. Liu, Z. Chen and M. Kanehira, *Energy Environ. Sci.*, 2012, 5, 6104-6110.
156. I. P. Parkin and R. G. Palgrave, *Journal of Materials Chemistry*, 2005, 15, 1689-1695.
157. S. A. O'Neill, R. J. Clark, I. P. Parkin, N. Elliott and A. Mills, *Chemistry of Materials*, 2003, 15, 46-50.
158. C. Sella, M. Maaza, O. Nemraoui, J. Lafait, N. Renard and Y. Sampeur, *Surf. Coat. Technol.*, 1998, 98, 1477-1482.
159. P. Jin and S. Tanemura, *Japanese Journal of Applied Physics*, 1994, 33, 1478.
160. N. R. Mlyuka, G. A. Niklasson and C. G. Granqvist, *Phys. Status Solidi A*, 2009, 206, 2155-2160.
161. D. Vernardou, M. E. Pemble and D. W. Sheel, *Chemical Vapor Deposition*, 2006, 12, 263-274.
162. T. T. Kodas and M. J. Hampden-Smith, *The chemistry of metal CVD*, John Wiley & Sons, 2008.
163. R. Binions, G. Hyett, C. Piccirillo and I. P. Parkin, *Journal of Materials Chemistry*, 2007, 17, 4652-4660.
164. C. L. Yaws, *Handbook of Vapor Pressure: Volume 4:: Inorganic Compounds and Elements*, Gulf Professional Publishing, 1995.
165. S. A. O'Neill, R. J. H. Clark, I. P. Parkin, N. Elliott and A. Mills, *Chemistry of Materials*, 2003, 15, 46-50.
166. G. Silversmit, D. Depla, H. Poelman, G. B. Marin and R. De Gryse, *Journal of Electron Spectroscopy and Related Phenomena*, 2004, 135, 167-175.
167. E. Hryha, E. Rutqvist and L. Nyborg, *Surface and interface analysis*, 2012, 44, 1022-1025.
168. U. Qureshi, T. D. Manning and I. P. Parkin, *Journal of Materials Chemistry*, 2004, 14, 1190-1194.
169. P. Evans, M. E. Pemble and D. W. Sheel, *Chemistry of Materials*, 2006, 18, 5750-5755.
170. U. Schwingenschlögl and V. Eyert, *Annalen der physik*, 2004, 13, 475-510.
171. C. Griffiths and H. Eastwood, *Journal of Applied Physics*, 1974, 45, 2201-2206.
172. N. Bravaya and A. Pomogailo, *Bulletin of the Russian Academy of Sciences, Division of chemical science*, 1992, 41, 1351-1357.
173. D. Barreca, L. E. Depero, E. Franzato, G. A. Rizzi, L. Sangaletti, E. Tondello and U. Vettori, *Journal of the Electrochemical Society*, 1999, 146, 551-558.
174. P. Schilbe, *Physica B: Condensed Matter*, 2002, 316, 600-602.

175. P. Schilbe and D. Maurer, *Materials Science and Engineering: A*, 2004, 370, 449-452.
176. G. Petrov, V. Yakovlev and J. Squier, *Applied physics letters*, 2002, 81, 1023-1025.
177. J. Parker, *Physical Review B*, 1990, 42, 3164.
178. X. Wang, H. Li, Y. Fei, X. Wang, Y. Xiong, Y. Nie and K. Feng, *Applied Surface Science*, 2001, 177, 8-14.
179. C. Julien, G. Nazri and O. Bergström, *physica status solidi (b)*, 1997, 201, 319-326.
180. S. Lu, L. Hou and F. Gan, *Journal of materials science*, 1993, 28, 2169-2177.
181. C. S. Blackman, C. Piccirillo, R. Binions and I. P. Parkin, *Thin Solid Films*, 2009, 517, 4565-4570.
182. A. Taylor, I. Parkin, N. Noor, C. Tummeltshammer, M. S. Brown and I. Papakonstantinou, *Opt. Express*, 2013, 21, A750-A764.
183. S. Y. Li, G. A. Niklasson and C. G. Granqvist, *Thin Solid Films*, 2012, 520, 3823-3828.
184. T. Smith and J. Guild, *Transactions of the Optical Society*, 1931, 33, 73.
185. D. Le Bellac, G. Niklasson and C. Granqvist, *Journal of Applied Physics*, 1995, 77, 6145-6151.
186. J. F. De Natale, P. Hood and A. B. Harker, *Journal of Applied Physics*, 1989, 66, 5844-5850.
187. M. Sahana, G. Subbanna and S. Shivashankar, *Journal of Applied Physics*, 2002, 92, 6495-6504.
188. K. Appavoo, D. Y. Lei, Y. Sonnefraud, B. Wang, S. T. Pantelides, S. A. Maier and R. F. Haglund Jr, *Nano letters*, 2012, 12, 780-786.
189. A. Bi and J. Zhu, *Adv. Mater. Res. (Zuerich, Switz.)*, 2011, 152-153, 797-800.
190. Y. Li, S. Ji, Y. Gao, H. Luo and M. Kanehira, *Scientific reports*, 2013, 3.
191. M. Takahashi, K. Tsukigi, E. Dorjpalam, Y. Tokuda and T. Yoko, *The Journal of Physical Chemistry B*, 2003, 107, 13455-13458.
192. L. Kang, Y. Gao and H. Luo, *Acs Applied Materials & Interfaces*, 2009, 1, 2211-2218.
193. C. G. Granqvist, *Journal of Vacuum Science & Technology B*, 2014, 32, 060801.
194. Z. Wu, D. Lee, M. F. Rubner and R. E. Cohen, *Small*, 2007, 3, 1445-1451.
195. X. Zhang, A. Fujishima, M. Jin, A. V. Emeline and T. Murakami, *The Journal of Physical Chemistry B*, 2006, 110, 25142-25148.
196. A. Facchetti and T. J. Marks, *From Synthesis to Applications, Wiley, Chichester, UK*, 2010.
197. E. Fortunato, A. Gonçalves, A. Pimentel, P. Barquinha, G. Gonçalves, L. Pereira, I. Ferreira and R. Martins, *Applied Physics A: Materials Science & Processing*, 2009, 96, 197-205.
198. Z. Zhang, Y. Gao, Z. Chen, J. Du, C. Cao, L. Kang and H. Luo, *Langmuir*, 2010, 26, 10738-10744.
199. N. Aas, T. J. Pringle and M. Bowker, *J. Chem. Soc., Faraday Trans.*, 1994, 90, 1015-1022.
200. Y. Tanizawa and T. Suzuki, *J. Chem. Soc., Faraday Trans.*, 1995, 91, 3499-3503.
201. P. Evans, T. English, D. Hammond, M. E. Pemble and D. W. Sheel, *Applied Catalysis a-General*, 2007, 321, 140-146.
202. G. Hyett, M. Green and I. P. Parkin, *Journal of the American Chemical Society*, 2006, 128, 12147-12155.
203. R. N. Wenzel, *Industrial & Engineering Chemistry*, 1936, 28, 988-994.
204. C.-S. Kuo, Y.-H. Tseng and Y.-Y. Li, *Chemistry Letters*, 2006, 35, 356-357.

205. U. Diebold and T. Madey, *Surface Science Spectra*, 1996, 4, 227-231.
206. A. N. Shultz, W. Jang, W. Hetherington, D. R. Baer, L.-Q. Wang and M. H. Engelhard, *Surface science*, 1995, 339, 114-124.
207. H. Shibata, S. Kimura and H. Takatoh, *Japanese Journal of Applied Physics*, 2000, 39, 1327.
208. R. Alfonsetti, L. Lozzi, M. Passacantando, P. Picozzi and S. Santucci, *Applied Surface Science*, 1993, 70, 222-225.
209. M. Sakanoue, Y. Kinoshita, Y. Otsuka and H. Imai, *J. Ceram. Soc. Jpn.*, 2007, 115, 821-825.
210. J. Yu, X. Zhao and Q. Zhao, *Journal of materials science letters*, 2000, 19, 1015-1017.
211. J. R. DeVore, *JOSA*, 1951, 41, 416-417.
212. E. D. Palik, *Handbook of optical constants of solids*, Academic press, 1998.
213. L. Cook, W. Lowdermilk, D. Milam and J. Swain, *Applied optics*, 1982, 21, 1482-1485.
214. A. Vincent, S. Babu, E. Brinley, A. Karakoti, S. Deshpande and S. Seal, *The Journal of Physical Chemistry C*, 2007, 111, 8291-8298.
215. K. Fujita, J. Konishi, K. Nakanishi and K. Hirao, *Applied physics letters*, 2004, 85, 5595-5597.
216. H. Wang, M. Miyauchi, Y. Ishikawa, A. Pyatenko, N. Koshizaki, Y. Li, L. Li, X. Li, Y. Bando and D. Golberg, *Journal of the American Chemical Society*, 2011, 133, 19102-19109.
217. S. Colodrero, A. Mihi, L. Häggman, M. Ocaña, G. Boschloo, A. Hagfeldt and H. Míguez, *Advanced Materials*, 2009, 21, 764-770.
218. E. López-Honorato, P. Meadows, J. Tan and P. Xiao, *Journal of Materials Research*, 2008, 23, 1785-1796.
219. W.-J. Kim, J. N. Park, M. S. Cho and J. Y. Park, *Journal of Nuclear Materials*, 2009, 392, 213-218.
220. A. T. Harris, K. J. MacKenzie, O. M. Dunens and C. H. See, *Recent patents on nanotechnology*, 2008, 2, 25-40.
221. K. Dasgupta, J. B. Joshi and S. Banerjee, *Chemical Engineering Journal*, 2011, 171, 841-869.
222. C. W. Dunnill, Z. A. Aiken, A. Kafizas, J. Pratten, M. Wilson, D. J. Morgan and I. P. Parkin, *J. Mater. Chem.*, 2009, 19, 8747-8754.
223. A. Mills, G. Hill, S. Bhopal, I. P. Parkin and S. A. O'Neill, *J. Photochem. Photobiol., A*, 2003, 160, 185-194.
224. J. P. Waters, D. Smyth-Boyle, K. Govender, A. Green, J. Durrant and P. O'Brien, *Chemical Vapor Deposition*, 2005, 11, 254-260.
225. M. J. Powell, R. G. Palgrave, C. W. Dunnill and I. P. Parkin, *Thin Solid Films*, 2014, 562, 223-228.
226. J. Ananpattarachai, P. Kajitvichyanukul and S. Seraphin, *J. Hazard. Mater.*, 2009, 168, 253-261.
227. A. Mills, N. Elliott, G. Hill, D. Fallis, J. R. Durrant and R. L. Willis, *Photochemical & Photobiological Sciences*, 2003, 2, 591-596.
228. J. K. Zhou, L. Lv, J. Q. Yu, H. L. Li, P. Z. Guo, H. Sun and X. S. Zhao, *Journal of Physical Chemistry C*, 2008, 112, 5316-5321.
229. T. Kasuga, M. Hiramatsu, A. Hoson, T. Sekino and K. Niihara, *Langmuir*, 1998, 14, 3160-3163.
230. L. Ma, A.-P. Chen, J.-D. Lu, H.-B. He and C.-Z. Li, *Wuji Cailiao Xuebao(Journal of Inorganic Materials)*, 2012, 27, 33-37.
231. U. Diebold, *Applied Physics A*, 2003, 76, 681-687.
232. B. Dabbousi, J. Rodriguez-Viejo, F. V. Mikulec, J. Heine, H. Mattoussi, R. Ober, K. Jensen and M. Bawendi, *The Journal of Physical Chemistry B*, 1997, 101, 9463-9475.

233. S. Kim, B. Fisher, H.-J. Eisler and M. Bawendi, *Journal of the American Chemical Society*, 2003, 125, 11466-11467.
234. Y. Lu, Y. Yin, Z.-Y. Li and Y. Xia, *Nano letters*, 2002, 2, 785-788.
235. P. Scherrer, *Nachrichten von der Gesellschaft der Wissenschaften zu Göttingen, mathematisch-physikalische Klasse*, 1918, 1918, 98-100.
236. J. I. Langford and A. Wilson, *Journal of Applied Crystallography*, 1978, 11, 102-113.
237. B. Ohtani, O. Prieto-Mahaney, D. Li and R. Abe, *Journal of Photochemistry and Photobiology A: Chemistry*, 2010, 216, 179-182.
238. J. Tauc, *Materials Research Bulletin*, 1968, 3, 37-&.
239. A. Kafizas, C. Crick and I. P. Parkin, *Journal of Photochemistry and Photobiology a-Chemistry*, 2010, 216, 156-166.
240. H. Tang, K. Prasad, R. Sanjines, P. Schmid and F. Levy, *Journal of Applied Physics*, 1994, 75, 2042-2047.
241. M. Batzill, E. H. Morales and U. Diebold, *Physical Review Letters*, 2006, 96, 026103.
242. S. Porto, P. Fleury and T. Damen, *Physical Review*, 1967, 154, 522.
243. M. Ocana, J. V. Garcia-Ramos and C. J. Serna, *Journal of the American Ceramic Society*, 1992, 75, 2010-2012.
244. R. Quesada-Cabrera, C. Sotelo-Vazquez, J. C. Bear, J. A. Darr and I. P. Parkin, *Advanced Materials Interfaces*, 2014, 1.
245. A. Kafizas, C. J. Carmalt and I. P. Parkin, *Chemistry-a European Journal*, 2012, 18, 13048-13058.
246. M. Anpo, T. Shima, S. Kodama and Y. Kubokawa, *Journal of Physical Chemistry*, 1987, 91, 4305-4310.
247. K. J. A. Raj and B. Viswanathan, *Indian J. Chem. A*, 2009, 48, 1378.
248. A. L. Linsebigler, G. Lu and J. T. Yates Jr, *Chemical Reviews*, 1995, 95, 735-758.
249. J. Augustynski, *Electrochimica Acta*, 1993, 38, 43-46.
250. T. Luttrell, S. Halpegamage, J. Tao, A. Kramer, E. Sutter and M. Batzill, *Scientific reports*, 2014, 4.
251. A. Mills, A. Lepre, N. Elliott, S. Bhopal, I. P. Parkin and S. O'neill, *Journal of Photochemistry and Photobiology A: Chemistry*, 2003, 160, 213-224.
252. T. A. Kandiel, R. Dillert, A. Feldhoff and D. W. Bahnemann, *The Journal of Physical Chemistry C*, 2010, 114, 4909-4915.
253. T. Ohno, K. Tokieda, S. Higashida and M. Matsumura, *Applied Catalysis A: General*, 2003, 244, 383-391.
254. D. C. Hurum, A. G. Agrios, K. A. Gray, T. Rajh and M. C. Thurnauer, *The Journal of Physical Chemistry B*, 2003, 107, 4545-4549.
255. D. O. Scanlon, C. W. Dunnill, J. Buckeridge, S. A. Shevlin, A. J. Logsdail, S. M. Woodley, C. R. A. Catlow, M. J. Powell, R. G. Palgrave and I. P. Parkin, *Nature Materials*, 2013, 12, 798-801.
256. M. R. Hoffmann, S. T. Martin, W. Choi and D. W. Bahnemann, *Chemical Reviews*, 1995, 95, 69-96.
257. J. Zhang, Q. Xu, Z. Feng, M. Li and C. Li, *Angewandte Chemie International Edition*, 2008, 47, 1766-1769.
258. JP2013184091A, 2013.
259. R. Lopez, L. Boatner, T. Haynes, L. Feldman and R. Haglund, *Journal of Applied Physics*, 2002, 92, 4031-4036.
260. V. Ramaswamy, T. E. Haynes, C. W. White, W. J. MoberlyChan, S. Roorda and M. J. Aziz, *Nano letters*, 2005, 5, 373-377.
261. A. Sidorov, O. Vinogradova, I. Obyknovennaya and T. Khrushchova, *Technical Physics Letters*, 2007, 33, 581-582.
262. Y. Zhou, A. Huang, Y. Li, S. Ji, Y. Gao and P. Jin, *Nanoscale*, 2013, 5, 9208-9213.

263. Y. Xu, W. Huang, Q. Shi, Y. Zhang, L. Song and Y. Zhang, *Journal of Sol-Gel Science and Technology*, 2012, 64, 493-499.
264. L. Mai, B. Hu, T. Hu, W. Chen and E. Gu, *The Journal of Physical Chemistry B*, 2006, 110, 19083-19086.
265. J. M. Booth and P. S. Casey, *Acs Applied Materials & Interfaces*, 2009, 1, 1899-1905.
266. Z. Zhang, S. Brown, J. B. Goodall, X. Weng, K. Thompson, K. Gong, S. Kellici, R. J. Clark, J. R. Evans and J. A. Darr, *Journal of Alloys and Compounds*, 2009, 476, 451-456.
267. P. Boldrin, A. K. Hebb, A. A. Chaudhry, L. Otley, B. Thiebaut, P. Bishop and J. A. Darr, *Ind. Eng. Chem. Res.*, 2007, 46, 4830-4838.
268. S. Elouali, L. G. Bloor, R. Binions, I. P. Parkin, C. J. Carmalt and J. A. Darr, *Langmuir*, 2012, 28, 1879-1885.
269. S. Kellici, K. Gong, T. Lin, S. Brown, R. J. Clark, M. Vickers, J. K. Cockcroft, V. Middelkoop, P. Barnes and J. M. Perkins, *Philosophical Transactions of the Royal Society of London A: Mathematical, Physical and Engineering Sciences*, 2010, 368, 4331-4349.
270. X. Weng, J. K. Cockcroft, G. Hyett, M. Vickers, P. Boldrin, C. C. Tang, S. P. Thompson, J. E. Parker, J. C. Knowles and I. Rehman, *Journal of combinatorial chemistry*, 2009, 11, 829-834.
271. R. I. Gruar, C. J. Tighe and J. A. Darr, *Ind. Eng. Chem. Res.*, 2013, 52, 5270-5281.
272. C. J. Tighe, R. Q. Cabrera, R. I. Gruar and J. A. Darr, *Ind. Eng. Chem. Res.*, 2013, 52, 5522-5528.
273. D. Sathyanarayana and C. Patel, *Bulletin of the Chemical Society of Japan*, 1964, 37, 1736-1740.
274. D. Sathyanarayana and C. Patel, *Bulletin of the Chemical Society of Japan*, 1967, 40, 794-797.
275. C. Aymonier, A. Loppinet-Serani, H. Reverón, Y. Garrabos and F. Cansell, *The Journal of Supercritical Fluids*, 2006, 38, 242-251.
276. N. N. Greenwood and A. Earnshaw, *Chemistry of the Elements*, Elsevier, 2012.
277. W. Chen, J. Peng, L. Mai, H. Yu and Y. Qi, *Chemistry Letters*, 2004, 33, 1366-1367.
278. Z. Gui, R. Fan, W. Mo, X. Chen, L. Yang, S. Zhang, Y. Hu, Z. Wang and W. Fan, *Chemistry of Materials*, 2002, 14, 5053-5056.
279. T. Yao, L. Liu, C. Xiao, X. Zhang, Q. Liu, S. Wei and Y. Xie, *Angewandte Chemie*, 2013, 125, 7702-7706.
280. M. Gondal, Q. Drmosh, Z. Yamani and T. Saleh, *Applied Surface Science*, 2009, 256, 298-304.
281. M. A. Hines and G. D. Scholes, *Advanced Materials*, 2003, 15, 1844-1849.
282. A. Magneli and G. Andersson, *Acta Chemica Scandinavica*, 1955, 9, 1378-1381.
283. K. C. Kam and A. K. Cheetham, *Materials Research Bulletin*, 2006, 41, 1015-1021.
284. R. L. Penn and J. F. Banfield, *Geochimica et cosmochimica acta*, 1999, 63, 1549-1557.
285. F. C. Case, *Journal of Vacuum Science & Technology A*, 1989, 7, 1194-1198.
286. S. A. Corr, M. Grossman, Y. Shi, K. R. Heier, G. D. Stucky and R. Seshadri, *Journal of Materials Chemistry*, 2009, 19, 4362-4367.
287. Y. Hakuta, T. Ohashi, H. Hayashi and K. Arai, *Journal of Materials Research*, 2004, 19, 2230-2234.
288. Y. Ding, G. Zhang, H. Wu, B. Hai, L. Wang and Y. Qian, *Chemistry of Materials*, 2001, 13, 435-440.

289. X. Sun, X. Chen, Z. Deng and Y. Li, *Materials Chemistry and Physics*, 2003, 78, 99-104.
290. J. B. Goodall, S. Kellici, D. Illsley, R. Lines, J. C. Knowles and J. A. Darr, *Rsc Advances*, 2014, 4, 31799-31809.
291. L. A. Gea and L. Boatner, *Applied physics letters*, 1996, 68, 3081-3083.
292. I. Yamaguchi, T. Manabe, T. Tsuchiya, T. Nakajima, M. Sohma and T. Kumagai, *Jpn. J. Appl. Phys.*, 2008, 47, 1022-1027.
293. M. Soltani, M. Chaker, E. Haddad, R. Kruzelecky and J. Margot, *Journal of Vacuum Science & Technology A: Vacuum, Surfaces, and Films*, 2007, 25, 971-975.
294. J. Ye, L. Zhou, F. Liu, J. Qi, W. Gong, Y. Lin and G. Ning, *Journal of Alloys and Compounds*, 2010, 504, 503-507.
295. L. Dai, S. Chen, J. Liu, Y. Gao, J. Zhou, Z. Chen, C. Cao, H. Luo and M. Kanehira, *Physical Chemistry Chemical Physics*, 2013, 15, 11723-11729.
296. F. Beteille and J. Livage, *Journal of Sol-Gel Science and Technology*, 1998, 13, 915-921.
297. C. Batista, J. Carneiro, R. Ribeiro and V. Teixeira, *Journal of nanoscience and nanotechnology*, 2011, 11, 9042-9045.
298. Y. Cui, X. Wang, Y. Zhou, R. Gordon and S. Ramanathan, *J. Cryst. Growth*, 2012, 338, 96-102.
299. X. Weng, B. Perston, X. Z. Wang, I. Abrahams, T. Lin, S. Yang, J. R. Evans, D. J. Morgan, A. F. Carley and M. Bowker, *Applied Catalysis B: Environmental*, 2009, 90, 405-415.
300. Z. Zhang, J. B. Goodall, D. J. Morgan, S. Brown, R. J. Clark, J. C. Knowles, N. J. Mordan, J. R. Evans, A. F. Carley and M. Bowker, *Journal of the European Ceramic Society*, 2009, 29, 2343-2353.
301. H. Hobbs, S. Briddon and E. Lester, *Green Chemistry*, 2009, 11, 484-491.
302. A. Darlinski and J. Halbritter, *Surface and interface analysis*, 1987, 10, 223-237.
303. A. Coats and J. Redfern, *Analyst*, 1963, 88, 906-924.
304. F. Holtzberg, A. Reisman, M. Berry and M. Berkenblit, *Journal of the American Chemical Society*, 1957, 79, 2039-2043.
305. G. T. Went, S. T. Oyama and A. T. Bell, *Journal of Physical Chemistry*, 1990, 94, 4240-4246.
306. I. E. Wachs and B. M. Weckhuysen, *Applied Catalysis A: General*, 1997, 157, 67-90.
307. B. King, H. Patel, D. Gulino and B. Tatarchuk, *Thin Solid Films*, 1990, 192, 351-369.
308. G. Jorgenson and J. Lee, *Solar Energy Materials*, 1986, 14, 205-214.

Appendix

Appendix 1:

Calculations of the transmittance spectra through the multilayer structures were performed using a transfer matrix method. The refractive index of TiO_2, SiO_2 and VO_2 were taken from Devore,[211] Palik[212] and Mlyuka,[160] respectively. The model assumed the multilayer film stack was deposited upon a glass (SiO_2) substrate and irradiated from a broadband light source in air. The reported transmittance values were taken between the region of air directly in contact with the TiO_2 layer and the region of glass in direct contact with the bottom VO_2 layer. The SiO_2 layer in the system reported is optically thicker than the coherence length of broadband sunlight. Therefore, it was expected to have a broad phase distribution at the SiO_2-VO_2 interface for light that had passed fully through the SiO_2 layer. This effectively inhibited the formation of a resonant cavity within the SiO_2 layer, decoupling resonance between the TiO_2 and VO_2 layers. In order to model incoherence in the SiO_2 layer, the model was adapted for the transfer matrix calculation method. Both electric field and phase information were maintained within the TiO_2 and VO_2 layers (and at their respective boundaries). However, within the SiO_2 layer only electric field information was preserved.

Publications

[1] D. O. Scanlon, C. W. Dunnill, J. Buckeridge, S. A. Shevlin, A. J. Logsdail, S. M. Woodley, C. R. A. Catlow, **M. J. Powell**, R. G. Palgrave, I. P. Parkin, G. W. Watson, T. W. Keal, P. Sherwood, A. Walsh, A. A. Sokol, *Nature Materials*, 2013, 12, 798-801.

[2] **M. J. Powell**, R. G. Palgrave, C. W. Dunnill, I. P. Parkin, *Thin Solid Films*, 2014, 562, 223-228.

[3] **M. J. Powell**, C. W. Dunnill, I. P. Parkin, *Journal of Photochemistry and Photobiology A: Chemistry*, 2014, 281, 27-34.

[4] **M. J. Powell**, R. Quesada-Cabrera, W. L. Travis, I. P. Parkin, *Journal of Materials Chemistry A*, 2015. *In press.*

[5] R. Quesada-Cabrera, **M. J. Powell**, P. Marchand, C. J. Denis, J. A. Darr, I. P. Parkin, *Journal of Nanoscience and Nanotechnology*, 2015. *In press.*

[6] **M. J. Powell**, P. Marchand, C. J. Denis, J. C. Bear, J. A. Darr, I. P. Parkin, *Nanoscale*, 2015. Submitted.

[7] **M. J. Powell**, R. Quesada-Cabrera, A. Taylor, D. Teixeira, I. Papakonstantinou, R. G. Palgrave, G. Sankar, I. P. Parkin, *Journal of Energy and Environmental Science*, 2015. Submitted.